POLITECNICO DI TORINO

Dottorato di Ricerca in
Metrologia: Scienza e Tecnica delle Misure

HIGH INTENSITY FOCUSED ULTRASOUND AND OXYGEN LOAD NANOBUBBLES: TWO DIFFERENT APPROCHES FOR CANCER TREATMENT

Ph.D Thesis

Chiara Magnetto

POLITECNICO DI TORINO

Dottorato di Ricerca in
Metrologia: Scienza e Tecnica delle Misure
Ciclo XXVI

HIGH INTENSITY FOCUSED ULTRASOUND AND OXYGEN LOAD NANOBUBBLES: TWO DIFFERENT APPROCHES FOR CANCER TREATMENT

Ph.D Thesis

Examinee:
Chiara Magnetto
Student N: 178852

Supervisors:
Dott. Giovanni Durando
Dott. Adriano Troia
Prof.ssa Maria P. Bussa

Academic Year: 2013/2014

HIGH INTENSITY FOCUSED ULTRASOUND AND OXYGEN LOAD NANOBUBBLES: TWO DIFFERENT APPROCHES FOR CANCER TREATMENT

ABSTRACT

The study of applications based on the use of ultrasound in medicine and biology for therapeutic purposes is under strong development at international level and joins the notoriously well-established and widespread use of diagnostic applications [1]. In the past few years, High Intensity Focused Ultrasound (HIFU) has developed from a scientific curiosity to an accepted therapeutic modality. HIFU is a non invasive technique for the treatment of various types of cancer, as well as non-malignant pathologies, by inducing localized hyperthermia that causes necrosis of the tissue. Beside HIFU technology, other innovative therapeutic modalities to treat cancer are emerging. Among them, an extremely innovative technique is represented by oxygen loaded nanobubbles (OLNs): gas cavities confined by an appropriately functionalized coating. This is an oxygenating drugs aimed at re-oxygenation of cancerous tissue. Oxygen deficiency, in fact, is the main hallmark of cancerous solid tumors and a major factor limiting the effectiveness of radiotherapy. In this work, these two approaches to treat tumours are under study from a metrological point of view. In particular, a complete characterization of an HIFU fields regarding power, pressure and temperature is provided while oxygen load nanobubbles are synthesized, characterized and applied in *in vitro* and *in vivo* experiments.

KEYWORDS: HIFU, temperature, nanobubbles oxygen, sonophoresis

CONTENTS

LIST OF FIGURES

CHAPTER 1

INTRODUCTION AND BACKGROUND

Cancer is the general name for a group of more than 100 diseases where cells in a part of the body begin to grow abnormally and uncontrollably. In 2007, cancer surpassed cardiovascular and cerebrovascular diseases as the leading cause of death. Human efforts have made great strides in the treatment of cancer. A century ago the chances of someone surviving cancer was negligible. Today two out of every three people diagnosed will still be alive at the end of five years. It is evident by the ever-increasing number of survivors that cancer diagnosis and treatment continues to improve, although the 'cure' for cancer has been far more elusive than once hoped [2]. Cancer treatments have improved in part due to the increase in understanding of cellular, genetic and molecular mechanisms, which provide targets for interventions to prevent, detect, eliminate and control the disease [3]. When the disease is local, surgery and radiation therapy are commonly used to treat cancer with a radical intent. Technological advancements in imaging and non-invasive treatments bring new therapeutic possibilities to the field [4]. Among the minimally invasive treatment methods that have been developed, High Intensity Focused Ultrasound (HIFU) appears the most investigated technology in the new panorama of solid tumor treatment based on ultrasound [5-6]. In HIFU medical treatments, ultrasound (US) energy emitted by transducer is focused into a small volume to heat and destroy the targeted tissue while ideally not damaging tissue outside the focal region. In spite of the multitude of medical applications, the effects of ultrasonic waves interactions on living tissues are not completely described and the definition of the "acoustic dose" is still dividing the scientific community. For this reason, the transducer's characterization in terms of

acoustic pressure, ultrasound power measurement and monitoring of the temperature rise induced by ultrasound beam in tissues is essential. The characterization of the ultrasonic field is carried out through the use of hydrophones able to evaluate the spatial distribution of the acoustic pressure; however, high intensity and possible cavitation phenomena generated by the focused transducers restrict the use of conventional sensors (piezoelectric) for the characterization of these sources. Recently, new measurement techniques based on optical methods are emerged. One of the most promising measurement methods is the fiber optic hydrophone, a tool that allows obtaining an accurate measurement of pressure and temperature with a high spatial and temporal resolution; moreover, it can be exposed to high intensity and acoustic cavitation. My thesis work has been conducted with the aim of characterizing the HIFU sources and to measure the main parameters of the acoustic field (power and pressure). After that, a fiber optic hydrophone was used to perform measurements of pressure emitted by a transducer and for the determination of the temperature increase induced by ultrasound field. Heating effects induced by HIFU transducers were observed not only in water, but also in different tissue mimicking material (TMM) realized at INRiM: an agar based gel, a polyacrilamide gel and for the first time a reversible thermochromic silica gel. Subsequently to the measurements carried out in laboratory, temperature rise in the focus of an HIFU transducer was evaluated in situ, at Istituto Oncologico Europeo (IEO) of Milan.

Among high intensity focused ultrasound, other innovative applications that use ultrasound to treat cancer are under development. In this regard, nanobubbles represent a new class of agents with both diagnostic and therapeutic applications. Indeed, encapsulated gas nanobubbles are well known as ultrasound contrast agents for medical ultrasound imaging [7]. Nonetheless, they not only help to image, but they can also be used as drug/gene carriers [8]. The nanobubbles as drug/gene carriers have an average size less than that of red blood cells, i.e. they are capable of penetrating even into the small blood capillaries and releasing drug and genes under the action of ultrasound field. The application of ultrasound and nanobubbles to targeted drug and gene delivery has been the subject of intense experimental research [9]. Under exposure of sufficiently high-amplitude ultrasound, these targeted nanobubbles would rupture, spewing drugs or genes, which are contained in its encapsulating layer, to targeted cells (sonoporation) or tissues (sonophoresis). At INRIM, we developed a particular type of nanobubbles: oxygen-filled nanobubbles (OLNs), which are gaseous cavity confined by a coating

suitably functionalized. OLNs are an innovative oxygenating drugs aimed at treating hypoxia-associated pathologies, in particular for re-oxygenation of cancerous tissue. It has been known for nearly a century that hypoxic cells are more resistant to radiotherapy than aerobic cells, and tumor hypoxia is a major factor leading to the resistance of tumors to radiation treatment as well as several cytotoxic agents [9]. In my thesis, various formulations of OLNs has been synthesized and characterized. OLNs can be prepared in liquid or gel formulations, shelled with chitosan or dextran and cored with perfluoropentane (PFP) or decafluoropentane (DFP). In vitro, nanobubbles are effective to release oxygen in absence and presence of ultrasound (sonophoresis induced by ultrasonic transducers through a membrane of pig skin epidermis). The application of ultrasound combined with oxygen-carrier nanobubbles is demonstrated as a method to locally increase dissolved oxygen. Moreover, they were not cytotoxic after internalization by human keratinocytes. In vivo, nanobubbles increased levels of oxygenated hemoglobin (photoacoustic studies) and transcutaneous oxygen pressure ($TcPO_2$) after topical treatment of hypoxic mice both in the absence and in the presence of ultrasound.

In this chapter, a brief introduction to the main applications of ultrasound in medicine, both regarding diagnostic and therapeutic applications is provided. This introduction is followed by a description of the physical effects caused by the interaction of ultrasound with the propagation medium. Finally, a complete description of the therapeutic applications of ultrasound is given with particular interests for high intensity focused ultrasound and for therapeutic applications which use micro and nanobubbles.

1.1 ULTRASOUND IN MEDICINE

Ultrasound, a form of mechanical energy that is transmitted through and into biological tissues as an acoustic pressure wave at frequencies above the limit of human hearing, is used widely in medicine as a therapeutic, operative, and diagnostic tool [10,11]. Therapeutic ultrasound use intensities as 1 to 3 W/cm^2 and can cause considerable heating in living tissues. To take full advantage of this energy absorption, physical therapists often use such levels of ultrasound acutely to decrease joint stiffness, to

reduce pain and muscle spasms, and to improve muscle mobility [12]. The use of ultrasound as a surgical instrument involves even higher levels of intensity (up to 300 W/cm^2), and sharp bursts of energy are used to fragment calculi, to ablate tissues such as cancer tissue, cataracts, and even to remove methylmethacrylate cement during revision of prosthetic joints [13]. At the opposite end of the ultrasound-intensity spectrum, much lower magnitudes of 1 to 50 mW/cm^2 are used to drive diagnostic devices that noninvasively image vital organs, fetal development, peripheral blood flow, and metabolic bone diseases such as osteoporosis and, coincidentally, to evaluate fracture callus during healing [14,15]. The intensity level used for imaging, which is five orders of magnitude below that used for surgery, is regarded as non-thermal and non-destructive [16]. Nevertheless, low-intensity ultrasound is still a mechanical force, and it therefore holds the potential to influence bone mass and morphology through bone tissue's strong sensitivity to physical stimuli.

1.2 INTERACTION OF ULTRASOUND WITH TISSUE

An ultrasound wave emitted by transducer outside the body must travel through multiple tissue layers, (including skin, subcutaneous fat, muscle), prior to reaching the desired treatment site within the target organ. At each tissue interface, part of the energy carried by the sound wave will be reflected, whilst the remaining energy is transmitted. The transmission coefficient depends primarily on the difference in acoustic impedance, *Z*, defined as the product of density and speed of sound, between the two tissue layers, as well as on the thickness of each layer [17]. At interfaces where there is little difference in acoustic properties, the transmission coefficient is close to unity. With the exception of fat, air and bone, most tissues in the human body have acoustic properties similar to those of water. Aqueous media are therefore optimal for transmitting ultrasound energy from the transducer into the body, and reflections at tissue interfaces are generally weak.

Furthermore, when ultrasound propagates through a particular tissue layer, the pressure fluctuations induced lead to shearing motion of tissue at a microscopic level, which results in frictional heating. Part of the mechanical energy carried (in/out) by the

incident wave is thus converted into heat by this viscous absorption, which constitutes the primary mechanism for ultrasound-induced hyperthermia. In an in homogenous medium, small regions with different acoustic properties from their surroundings will scatter the incident wave in all directions, causing a loss of acoustic intensity in the direction of sound propagation. The loss in incident acoustic energy in a medium is characterised by its attenuation coefficient, μ, given by the sum of the absorption coefficient μ_a and the scattering coefficient μ_s.

The ultrasound intensity, *I*, following propagation through a distance *x* in a medium of attenuation coefficient μ is given by:

$$I = I_o e^{-\alpha x} \tag{1}$$

where I_0 is the incident ultrasound intensity at the origin (x=0).

For most tissues, the attenuation coefficient is related to the ultrasound frequency via a power law of the form

$$\alpha = af^b \tag{2}$$

where *a* and *b* are tissue-specific constants [17]. It is precisely this dependency of attenuation on frequency that renders ultrasound particularly well suited to non-invasive therapy, but which causes some significant challenges in optimizing HIFU induced hyperthermia. Unlike other hyperthermia modalities, such as radiofrequency RF or microwaves, the attenuation ultrasound field through water-like media at ultrasound frequencies is sufficiently low that adequate amounts of energy can be delivered to the depths through tissue required during clinical treatments. Increasing the ultrasound excitation, frequency results in a power-law increase of both the absorption and attenuation coefficient. The former implies that higher heat deposition is achieved, while both result in a decreased penetration depth. Therefore, the optimal choice of therapeutic ultrasound frequency is application-specific, and represents a compromise between treatment depth and the desired rate of heating.

1.5.3 MECHANISM OF EFFECTS ON TISSUE

Ultrasound is a pressure wave meaning that it has regions of high pressure (compression) and low pressure (rarefaction) (Figure 1.1). As acoustic waves propagate through a medium the particles in the medium are subjected to the compression and rarefaction regions of the wave which result in changes to the particle displacement, velocity, density, pressure and temperature. The interactions of ultrasound for which bioeffects are produced can be grouped into two categories: thermal and mechanical effects. Broadly, mechanical effects can best be predicted from knowledge of individual pulses, whilst thermal effects can best be predicted from knowledge of energy flow over an extended time period.

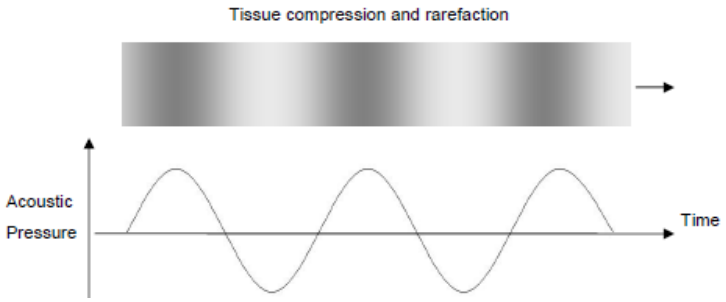

Figure 1.1: ultrasound, propagating through tissue,causes alternating regions of increased and reduced pressure related to compression and rarefaction.

1.5.4 THERMAL EFFECTS

Therapeutic applications of ultrasound depend on the direct interaction of the ultrasound field with the tissue Thermal mechanism can be used to create either a low level thermal rise, in general up to around 45 ° C (local hyperthermia) or, a short, highly localized high temperature rise that cooks the tissue up to 60-65 °C (thermal ablation). Ultrasound-induced temperature rise is dependent on several factors, including tissue properties (e.g., absorption coefficient, density, perfusion rate, etc.), ultrasound exposure parameters (e.g., frequency, pressure amplitude, pulse duration, pulse repetition frequency (PRF), etc.). The generation of heat in tissues can typically be controlled through proper exposure planning [18], the acoustic energy removed from

the wave by absorption is deposited in the medium as heat at a rate q_v per unit of volume

$$q_v = 2\alpha_a I \tag{3}$$

where *I,* is the intensity of the wave at the focus in W/cm^2, and α is amplitude absorption coefficient in dB cm^{-1}MHz^{-1}. Due to this heat deposition the temperature *T* at a point in the field will rise at a rate given by

$$\frac{dT}{dt} = \frac{2\alpha_a I}{\rho C_p} \tag{4}$$

Where C_p is specific heat capacity in J/Kg °K of the medium at a constant pressure in Pa.

Once the temperature of the medium rises above the ambient value, convection, conduction and radiation will result in heat being transferred from warmer to cooler regions [18]. In addition, an extra process of perfusion occurs in tissue. Perfusion is described as the process by which heat is removed from warmer regions by blood flowing through capillaries and blood vessels and redistributed to cooler regions. The temperature elevation in a region subjected to an acoustic disturbance is a direct result of acoustic power absorption in the region of interest. For soft tissues these processes can be described by using the Pennes bio-heat transfer equation:

$$\rho_t C_t \frac{\partial T}{\partial t} = K_t \Delta^2 T - w_b C_b (T - T_\infty) + q_v \tag{5}$$

where ρ, is the density, K_t is the specific heat, and C_t, C_b are the thermal conductivity with the subscripts *t* and *b* referring to tissue and blood, respectively, *T* is the temperature of the tissue,t_∞ is the arterial blood temperature, and *t* is the time. Here the first term on the right-hand side accounts for heat diffusion while the second term accounts for blood perfusion losses with w_b being the perfusion rate. The term q_v is the rate of acoustic power deposition per unit volume given by Equation. (1).

Another important parameter related to thermal effects is thermal lesion. The concept of thermal lesion is usually used to determine the extent of the lesioned tissue [19]. The thermal dose can be defined as the time (*t*) required to produce an iso-effect at

temperature *T* to the time (*t 43*) which would be required to produce the same effect at 43 °C. Tissue exposed for more than the equivalent of one hour at 43 °C is considered "lesioned" (Figure 1.2). Depending on the cell type, this is roughly equivalent to 3 logs of cell kill in a typical cell survival experiment and has been shown to induce tissue necrosis in-vivo. The boundaries of the thermal isodose curves delineate the lesion shape and size. A threshold for the denaturing of tissue protein (thermal coagulation necrosis), is calculated according to the thermal dose (*TD*) formulation.

$$TD43(t) = \int_{U}^{t} R^{43-t(t)} dt' \qquad (6)$$

where the empirical constant $R = 0.5$ $t \geq 43$ °C and $R = 0.25$ t < 43°C. The thermal dose required to create a thermal lesion is equivalent to the thermal dose of a 240- min exposure at 43°C [20].

The thermal dose concept has been proposed to quantify the relationship between treatment efficacy and the temperature of the target as a function of time. Sapareto and Dewey (1984) [19] proposed the following relationship between the tissue thermal dose *TD43(t)* (also known as cumulative equivalent minutes (CEM) at 43 °C) as a function of treatment temperatures, *T*(*t*), and time *t*.

This definition originated from the hyperthermia protocol, when the tissue was heated to a temperature of 43–45°C during a long exposure of several hours [20] or the temperature rise is above a threshold of 56°C and the exposure time is at least 1s. In these cases, irreversible cell death will be induced through coagulation necrosis [21]. The coagulation necrosis is characterized by cell death mainly due to protein denaturation, which is caused by an infarct such as excessive heat [22].

However, it has been shown that this model gives good estimations of the thermal lesion for the higher temperatures caused by HIFU, which include 10 s at 53 °C, 1 s at 57 °C, and 0.1 s at 60 °C. In HIFU treatments, the temperature commonly exceeds 70 °C in about 1–4 s. Thus, tissue necrosis occurs almost immediately [20].

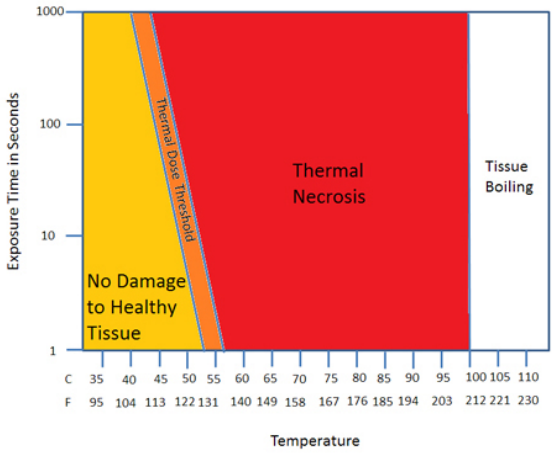

Figure 1.2: Relation between exposure time and temperature on tissues

1.2.3 MECHANICAL EFFECTS

Non-thermal effects encompass a range of processes such as radiation force and acoustic streaming. Most relevant to this thesis and to mechanical bioeffects of ultrasound in general, is cavitation which is described below.

Acoustic Cavitation: Acoustic cavitation term is used to refer to a range of complex phenomena that involve the creation, oscillation, growth and collapse of bubbles within a medium [18]. The cavitation behavior can be broadly classified into one of two categories: stable cavitation and inertial cavitation (Figure 1.3). The behavior of the bubble will depend on the frequency, pressure amplitude, bubble radius and environment surrounding the bubble. When an existing bubble is exposed to an ultrasonic field the acoustic pressure acts as a driving force that drives the bubble and results in the bubble radius varying. The bubble behaves as an oscillator with stiffness and inertia. The gas within the bubble provides the stiffness. As the gas is compressed it provides a force that resists the compression. The liquid surround the bubble provides the inertia and moves with the bubble wall. As a result the bubble has a natural resonant frequency f_r. For the case of a spherical air bubble of radius R_0 in water (assumed to be incompressible and inviscid) a simple calculation based on linear oscillations gives:

$$frR_0 \approx 3Hz \cdot m \qquad (7)$$

$$(R_0 \geq 10\mu)$$

When the bubble is exposed to an ultrasound field at its resonance frequency, it exhibits its maximum response. The resonance frequency is dependent on the initial size of the bubble. The maximum expansion of a non-inertial cavity typically does not exceed twice the equilibrium radius. The response of the bubble can be nonlinear and is dependent on variables including the acoustic pressure amplitude, exposure frequency, and size of the bubble. The damping of the bubble oscillations occurs through viscous dissipation, sound radiation, and thermal conduction mechanisms [23-25].

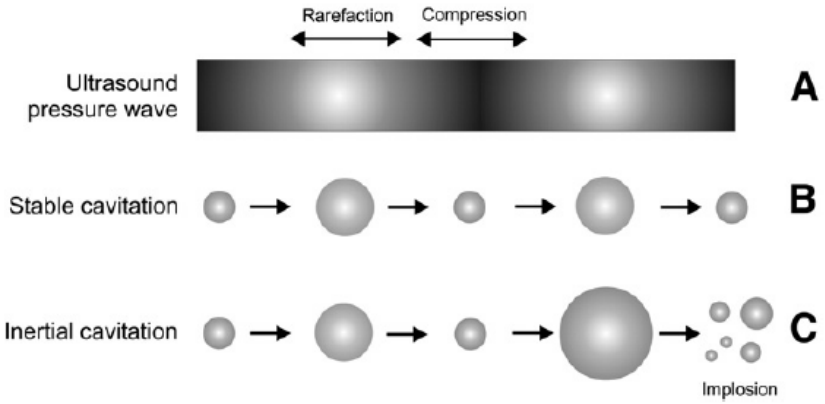

Fig. 1.3. Stable and inertial cavitation. (A) Schematic representation of an acoustic pressure wave. (B) and (C) show, respectively, stable and inertial cavitation of microbubbles.

Stable cavitation: At very low acoustic pressures, microbubbles oscillate in a symmetrical, linear way. This means that their expansion and compression is inversely proportional to the local ultrasound pressure [26]. At higher ultrasound intensities, microbubbles behave non-linearly with a lengthening of the expansion phase of the microbubbles, as the microbubbles are more resistant to compression than to expansion [27-28]. This phenomenon is also known as stable cavitation or non-inertial cavitation. During stable cavitation of the microbubble (Figure 1.4 A,B), there is gas influx (during expansion) and gas efflux (during compression). In the case of symmetrical oscillations, the netto gas influx over one expansion/compression cycle is zero. However, when the expansion phase extends, there is a net gas influx into the microbubble. For this reason, the microbubble grows until it reaches its resonant size, whereupon it demonstrates stable, low amplitude oscillation (Figure 1.3). Such stable oscillations create a liquid flow around the microbubbles, the so-called microstreams [29] (Figure 1.4C). When

these oscillating microbubbles are in close vicinity of cells, these cells will experience shear stress. The shear stress related to micro streaming is relatively high compared to the shear stress associated with blood flow (0.1–4 Pa) [30]. US induced elevated shear stress levels that may induce a large spectrum of biological effects which are explained in figure 1.4. Figure 1.4 (A), (B) and (C) refer to biophysical effects caused by stable cavitation, while (D) and (E) depict effects of inertial cavitation. Figure 1.4A: Pushing (left) and pulling (right) effects during the expansion and compression phase, respectively, of a stably oscillating microbubble, thereby disturbing the membrane integrity. Figure 1.4B: Acoustic radiation force causes microbubble displacement and compresses the microbubble against the cell membrane resulting in membrane disruption. The microbubble may even be pushed through the lipid bilayer to enter the cell. Figure 1.4C: stable oscillation of a microbubble creates microstreamings in the surrounding fluid, which exert mechanical stress on the cell membrane, causing pore formation.

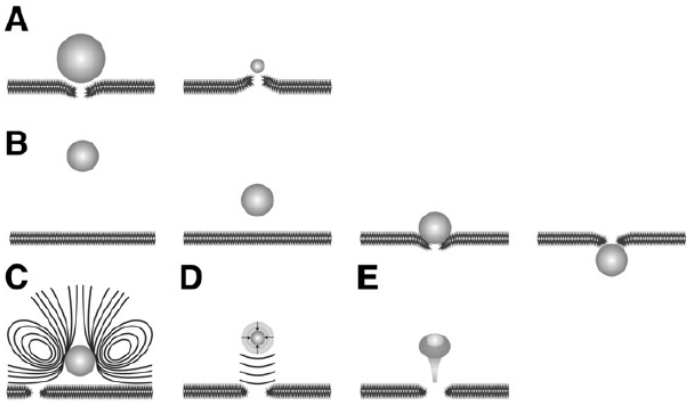

Figure 1.4. Biophysical effects of stably and inertial cavitating microbubbles. (A), (B) and (C) refer to biophysical effects caused by stable cavitation, while (D) and (E) depict effects of inertial cavitation.

Inertial cavitation: At sufficiently high exposure amplitudes, a bubble may expand to a maximum radius greater than twice its initial radius and then collapse rapidly to a small fraction of its initial radius [18] (Figure 1.3). This type of cavitation is called inertial cavitation. The relatively slow expansion is followed by a rapid collapse phase driven by the inertia of the spherically converging liquid. Various parameters determine the violence of the collapse of the inertial cavity.

In a given liquid, for a particular spherical bubble nucleus, the occurrence of inertial cavitation depends on the acoustic pressure amplitude, the acoustic frequency and

bubble radius. The surface tension forces in smaller bubbles prevent the initial growth so the bubbles do not grow enough. On the other hand, large nuclei can grow initially, however they do not collapse sufficiently to generate high temperatures. For a given bubble radius and frequency, there is a threshold pressure required for inertial cavitation. The response of an inertial cavitation to an acoustic field is highly nonlinear, such that a small increase in acoustic pressure amplitude can change the bubble response from a non-inertial cavitation to an inertial cavitation.

Figure 1.5 illustrates the transition threshold between inertial and non-inertial cavitation, based on the calculations of Apfel and Holland (1991) [31]. If within one period of the applied waveform, the bubble collapsed and generated a temperature in the gas in excess of 5000 K, they assumed inertial cavitation. The calculations show that for any frequency there is a minimum peak rarefactional pressure p_{opt} that is required to generate inertial cavitation. This will only occur for bubbles with an initial radius R_{opt}. For example from figure 1.4, for a 10MHz wave the minimum rarefactional pressure to induce inertial cavitation is about 0.84 MPa.

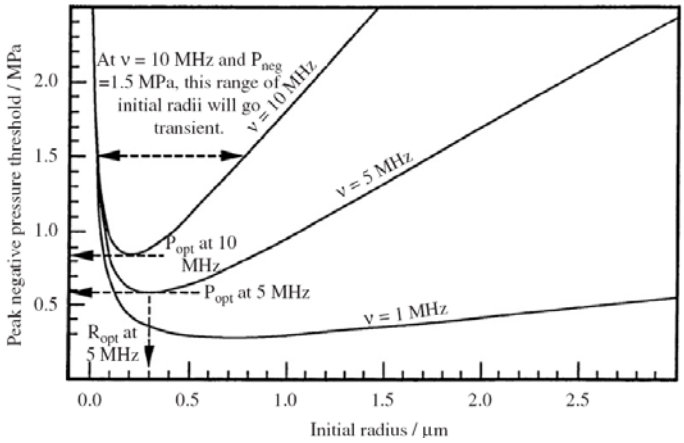

Figure. 1.5. Plot of the cavitation threshold in water as a function of initial nucleus radius for three frequencies of insonication: 1, 5, and 10 MHz. Nuclei consist of air bubbles initially at 300 K that undergo growth in a single cycle of ultrasound and collapse adiabatically to a temperature of 5000 K. Surface tension, viscosity, and inertia of the host fluid are included in this analytical model by Holland and Apfel [37-31]. For 5 MHz, the optimal nucleus radius is 0.3 Am with a corresponding cavitation threshold, Popt, of 0.58-MPa peak negative pressure. Note that at a pressure PV greater than Popt, a broader size range of nuclei cavitate.

The acoustic pressure at which the transition occurs is often called the threshold for inertial cavitation. Extremely high temperatures and pressures can be achieved at the minimum radius of the inertial bubble collapse [32]. Some models predict maximum collapse temperatures exceeding thousands of degrees Kelvin [25, 32]. These high temperatures and pressures are localized near the collapsing bubble. They are temporally limited to the duration of the collapse. Generally for a given pressure amplitude and bubble radius, the maximum collapse pressure in the bubble decreases as the frequency of exposure increases [25]. The motion of the bubble wall may become supersonic during inertial collapse. During the collapse of the microbubbles, shock waves (Figure 1.4D) can be generated in the fluid and jet formation (Figure 1.4E) can occur [33]. When a collapsing microbubble is located close to a surface, like a cell membrane, an asymmetrical collapse takes place, and results in the formation of a liquid jet towards the nearby surface. This microjet punctures the cell membrane, thereby creating a pore. Micro jets play a role in the fragmentation of kidney stones with lithotripter shock waves [34]. It has been shown that shock waves and microjets create very high forces that can generate high stresses on cell membranes, perforate cell membranes and even permeabilize blood vessels (Figure 1.4D) [35-37]. It has been suggested that liquid microjets might act as micro syringes, delivering drugs to cells [31,32].

1.3. THERAPEUTIC ULTRASOUND

Therapeutic ultrasound is generally described as the use of ultrasound for applications other than imaging or diagnostics [38]. For diagnostic applications of ultrasound, exposures are chosen primarily for their ability to give images with good spatial and temporal resolution, using sufficient pressure amplitude to give an acceptable signal to noise ratio. The aim is to obtain the required diagnostic information without causing biologically significant cellular effects, the energy deposition in tissues is meant to be minimal. In contrast, therapeutic applications require that the exposed target tissue undergoes reversible or irreversible change, depending on the goal of the treatment. Therapeutic ultrasound energy is usually delivered as continuous wave or tone burst (long pulse) exposures. Depending on the application, single element and phased array

sources may be used. Frequencies range from 0.8 MHz to 20MHz, with the choice of frequency being a compromise between the depth of the tissue to be treated, and the requirement for ultrasound absorption within the target to provide heating. For therapeutic applications, a number of methods are used to couple the sound into the tissue. Where the acoustic window is relatively flat, and the transducer's emitting surface is plane, aqueous gel may be used between the source's front face and the skin. However, for awkward tissue geometries and when, for example concave spherical bowl transducers are used, water may provide a better coupling medium. For the high power applications, it is important that the couplant is degassed to prevent the occurrence of cavitation. In diagnostic ultrasound, biological effects are undesirable and hence whereas application of therapeutic ultrasound is based on depositing ultrasound energy to specifically create beneficial effects. These effects can be mild and non-destructive, like those generated for physiotherapy healing [39], or more extreme and destructive, such as thermal ablation of tumors [6]. The mechanisms of interaction between ultrasound field with cells and tissues for producing therapeutic effects are typically divided into thermal and non-thermal mechanisms [40]. The three most important ultrasound mechanisms (heat generation, acoustic cavitation, and acoustic radiation forces) for creating bioeffects have been briefly covered in previous sections.

1.3.1. APPLICATIONS OF THERAPEUTIC ULTRASOUND

In 1927 it was recognized that ultrasound could produce lasting change in biological systems. This was the start of both ultrasound therapy and safety studies [41]. Tissue heating due to ultrasonic energy absorption has been used with therapeutic intent in many conditions. Recently it has been realized that good results, in terms of hypertermia and ablation, may also be obtained from the non-thermal effects that occur as ultrasound travels through tissue. Ultrasound therapies can broadly be divided into low power and high power therapies where low power applications include sonophoresis, sonoporation, gene therapy, sonothrombolysis, bone healing and wound healing. High power therapies encompasses physiotherapy, histotripsy, high intensity focused ultrasound (HIFU) and lithotripsy. Apart from physiotherapy uses, ultrasound therapies are currently not widespread. The following sections will describe the most frequently applications of

ultrasound for therapy with a particular interests for HIFU and for therapeutic applications which use micro and nanobubbles.

1.4 THERAPEUTIC ULTRASOUND: HIFU

High intensity focused ultrasound (HIFU) is gaining rapid clinical acceptance as a treatment modality enabling non-invasive tissue heating and ablation for numerous applications. HIFU treatments are usually carried out in a single session, often as a day case procedure, with the patient either fully conscious, lightly sedated or under light general anaesthesia. A major advantage of HIFU over other thermal ablation techniques is that there is no necessity for the transcutaneous insertion of probes into the target tissue. The high powered focused beams employed are generated from sources placed outside the body (for treatment of tumours of the liver, kidney, breast, uterus, pancreas) or in the rectum (for treatment of the prostate), and are designed to enable rapid heating of a target tissue volume, while leaving tissue in the ultrasound propagation path relatively unaffected. Given the wide-ranging applicability of HIFU, numerous extra-corporeal, transrectal and interstitial devices have been designed to optimise application-specific treatment delivery. Compared to diagnostic ultrasound, HIFU has significantly higher time-averaged intensities in the focal region of the ultrasound transducer [42]. Typical diagnostic ultrasound transducers deliver ultrasound with time-averaged intensities of approximately 0.1–100 mW/cm^2 and compression and rarefaction pressures of 0.001–0.003 MPa. HIFU transducers deliver ultrasound with intensities in the range of 100–10,000 W/cm^2 to the focal region, with peak compression pressures of up to 30 MPa and peak rarefaction pressures up to 10 MPa [42].

1.4.1 HISTORY OF HIFU

The first suggestion that high intensity ultrasound beams might be used for therapeutic purposes came in 1942 [43], but the first report of application of HIFU to humans was not until 1960 [44, 45]. This technique did not gain significant clinical acceptance until the 1990s, despite successful ophthalmological treatments before this date. Early equipment was heavy and unwieldy, and the original applications proposed were in the

brain, which involved surgical intervention to remove bone. The development of HIFU coincided with the introduction of the drug L-dopa. From a patient's perspective, L-dopa proved to be a more acceptable treatment for Parkinson's disease. The lack of imaging sophistication also restricted the growth of HIFU applications at that time. In order to capitalise on the precision of the cell killing proffered by HIFU, it is necessary to be able to achieve accurate placement of ''lesions'' within the target volume. Precise targeting and good treatment follow-up techniques (with anatomical and functional imaging), are only now available with ultrasound or magnetic resonance imaging (MRI) techniques, thus paving the way to realizing the full potential of HIFU treatments. Early attempts to place ultrasound lesions in the brain through the intact skull bone were unsuccessful [43, 46]. Small lesions were found in the brain, but there was profound damage to the scalp. Mode conversion and the high acoustic absorption of bone lead to a high degree of attenuation in the skull bone. Only once a window had been made in the skull, could discrete lesions be placed deep within the brain [47-48]. White matter appears to be more susceptible to damage than grey matter [49,50]. Fifty patients with Parkinson's disease were amongst the first people to be treated with HIFU [45]. Although it was claimed that the symptoms of Parkinsonism were eliminated, this treatment does not appear to have been taken further, probably because of the concurrent development of the drug L-dopa mentioned above. The requirement to remove a section of skull bone, combined with targeting complexity limited the progress of this neurosurgical research. However, phase correction (time reversal) techniques may allow the focus to be reconstructed following transmission through bone [51, 52]. The feasibility of this has been demonstrated using large area hemispherical phased array transducers, which allows reduction of the energy density at the skull surface. The first proposal to use focused ultrasound in ophthalmology came from Lavine et al. [53] who demonstrated cataract formation when the lens of the eye was targeted. Further experimental studies demonstrated that HIFU technique was able to decrease intra-ocular pressure [54], and produce lesions in the vitreous, lens, retina and choroid [55–56]. High intensity focused ultrasound has been used successfully in the treatment of glaucoma. This was first established in experimental models using intensities up to 2000Wcm^2 at 4.6 MHz. Histology showed focal thinning of the sclera, and focal disruption of the ciliary body with the conjunctiva remaining intact. The first human treatments, undertaken in 1982, gave encouraging results. Of the 880 patients treated, 79.3% had a sustained lowered intra-ocular pressure after 1 year [57]. High

intensity focused ultrasound has also been used with success in experiments to seal traumatic capsular tears [56], and in laboratory treatment of intra-ocular tumours [58, 59], retinal detachment and vitreous haemorrhage [55]. Although HIFU has shown considerable promise in these ophthalmological applications, laser surgery has enjoyed wider success and application, presumably because of its apparently simpler technology and application.

1.4.2 PHYSICS OF HIFU

The aim of most ablative therapies, whether for the treatment of cancer or of benign conditions, is the selective destruction of a targeted tissue volume, leaving surrounding tissues intact [60-61] (Figure 1.6). The aim of a high intensity focused ultrasound (HIFU) treatment is to raise the temperature of a selected, isolated tissue volume above 55°C. It is known that 55°C held for this time will lead to coagulative necrosis and immediate cell death [19, 62]. Instantaneous coagulative necrosis occurs and hence cell death with a margin of 6–10 cells between live and dead cells at the edge of the focal zone [60-63]. In theory, this is possible with a focused ultrasound beam, since the short wavelengths of ultrasound at MHz frequencies in soft tissue allows it to be focused into small, clinically relevant, volumes. Ultrasonic energy absorption within the focal volume induces high temperatures locally at the focus, with temperatures outside this region being kept at levels that are not cytotoxic.

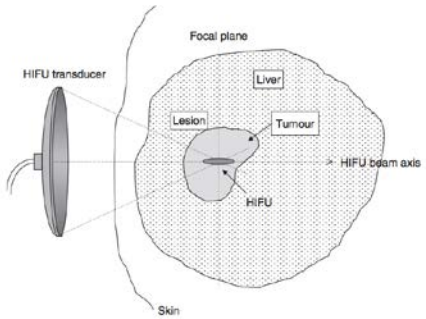

Figure 1.6: Diagrammatic illustration of the principle of HIFU. High-intensity ultrasound waves are generated by a transducer outside the body and focused onto a small region deep within tissue. HIFU-induced heating causes cell death by thermal necrosis within the focal volume, but leaves tissue elsewhere in the propagation path unaffected.

The volume of destroyed cells is call ‘‘lesion’’. An important feature of HIFU lesions is that the damage is spatially confined with no surrounding cellular damage. They are often referred to as ‘‘trackless’’. In this sense they are different from those produced by other ablative therapies which necessitate the introduction of an applicator into the volume [64-65]. A key objective of a HIFU treatment is to delivery the energy required to raise the tissue temperature to a cytotoxic level sufficiently fast that the tissue vasculature does not have a significant effect on the extent of cell killing, that is, that cooling due to blood perfusion or heat diffusion is not important. It has been shown that HIFU can lead to vessel wall disruption and also to vascular occlusion [66–67].

A transducer with a piezoelectric crystal can be used as a source of ultrasound that vibrates at a fixed frequency when electrical energy is applied. To provide a focus with a given depth and shape, single element transducers are designed using a flat piezoelectric element with a lens, a spherically curved element with concavity in the propagation direction, or a combination of transducer curvature and a lens. Such applicators may provide a fixed focus; however, they are limited in high- power applications because of mechanical self-heating of the element.

In Figure 1.7 is shown simple focusing achieved by a spherical-shaped concave radiator. This type of focusing transducer is usually a piezoelectric whose front surface is of spherical shape of a given radius of curvature (ROC), r_c. The aperture diameter of the transducer is *D*. The geometrical center of the sphere is at *C*. The dimensions of the curved front surface have the following relationship;

$D/2 = (\mathrm{ROC}) \sin \alpha$

$h = \mathrm{ROC}\,(1 - \cos \alpha)$,

Where h is the depth of the concave surface

f number = ROC / D

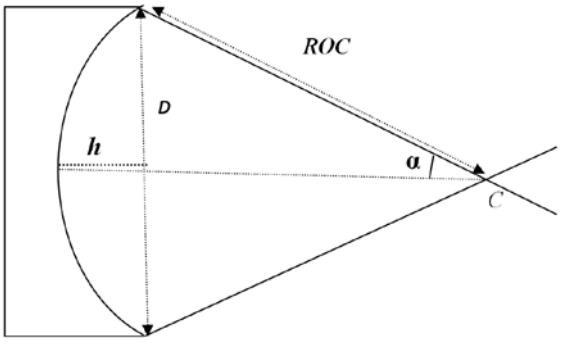

Figure 1.7: Illustration of a focusing acoustic radiator.

The focus of a single element transducer lies on its central axis near its center of curvature. It has been demonstrated by O'Neil (1949) [68] that the greatest intensity takes place near but not exactly at *C* (geometrical focus). The magnitude of focusing,

expressed by the ratio of the intensity at *C* to the average intensity at the radiating surface, is equal to ($2\pi h / \lambda$). In other words, decreasing f number increases the sharpness of the focusing [69]. Furthermore, it also decreases the distance between the physical focus and the geometrical focus *C*. The plane that contains *C* and is normal to the axis of the sound field is called the focal plane. The focal length is defined as distance *F* [69]. A cigar-shaped focal volume (an ellipsoid of revolution around the central axis) is formed with HIFU. The size depends on the frequency used, with its width decreasing with increasing frequency for a given absorbed energy [70]. At 1.7 MHz, using a 10 cm diameter transducer with a focal length of 14 cm produces focal lesion approximately 1.5 mm in diameter and 15 mm long. The precise shape of the lesion depends on the tissue acoustic properties, ultrasound intensity and exposure time, and the transducer geometry. The most useful frequencies for HIFU treatments in human diseases are from 0.8 MHz to 10 MHz, the ultrasound waves have wavelengths from 0.1 to 3 mm, which are much shorter than the dimensions of both tumors and applicators. Thus, dispersion of the beam is minimal and well-collimated beams are directed into tumor size volumes. The optimum frequency for a treatment at any depth is a compromise between the need to keep the attenuation in the tissue path overlying the target low in order that sufficient energy reaches this volume, and the necessity of having adequate absorption at the focus to ensure the required temperature rise [70]. Several factors determine whether an effective lesion will be formed. These include the thermal properties of the targeted tissue, the acoustic properties of the tissue that the beam will pass through, and the presence of blood vessels that, if close to the focus, can act as heat sinks reducing the rate of temperature rise.

Technological changes are under way to make the HIFU devices more users friendly and effective. Nowadays there are two methods for the application of ultrasound energy, namely, transrectal and extracorporeal devices.

1.4.3 HIFU DAMAGE ON TISSUES

Ultrasound beam propagating through tissue loses energy due to ultrasonic attenuation caused by both scattering and absorption of the tissue [22]. The absorption of ultrasonic energy causes a local temperature rise in tissue if the rate of heating exceeds the rate of cooling. The energy levels carried in the HIFU beam are several orders of magnitude greater than those of a clinical diagnostic ultrasound beam, within a wide range of frequencies from a few hundred kHz to a few tens of MHz [71]. When the intensity of the ultrasound beam is increased and focused onto a tight spot the temperature at the focus rises rapidly above a certain limit, it leads to effective cell killing even for very short exposures [72-21]. Very little damage to overlying or surrounding tissue occurs during HIFU lesioning. There are two main mechanisms that are directly involved in the tissue damage induced by HIFU exposure. The first is a thermal effect from the conversion of mechanical energy into heat in the tissue, and the second is acoustic cavitation.

The predominant mode of ablation with HIFU is heating. Absorption of ultrasound results in the conversion of ultrasonic energy to heat. Acoustic cavitation is the second mechanism of HIFU induced tissue damage. Cavitation is relatively unpredictable. It depends on many independent variables such as frequency, intensity pulse shape and length and the degree of presence of particles of gases in the medium [73]. During HIFU exposure, it would be difficult to identify distinctly thermal effect from mechanical effect. In practice, the two effects occur simultaneously within tissue. Hence, the coagulation necrosis induced by HIFU can be considered as the result of biological effects from a combination of mechanical stresses and thermal damage on the tissue [74]. However there is increasing interest in using cavitation to optimize HIFU treatments and this is currently under extensive investigation. Specifically, inducing cavitation during exposures can improve the rate of heating through enhanced absorption [74-77].

1.4.4 THE TREATMENT PROCESS

Effective HIFU treatments depend on the successful conduct of a number of different stages of the procedure. For cancer, the initial diagnosis is usually made from CT or MR

scans. An assessment of the tumour's visibility to diagnostic ultrasound is then required. This involves ascertaining that there is a suitable acoustic window through which the treatment can be delivered, that the target boundaries can be clearly identified, and that no sensitive normal tissue structures lie in the beam path. The target volume must be accurately identified and spatially localised. The second stage in the treatment is to determine the correct ultrasound exposure to achieve ablation. This is done in a number of ways. Where ultrasound imaging is used for guidance, the most common method is to use a combination of focal peak intensity and exposure time that results in a hyperechoic region at the target, whereas when MR is the guidance method, this combination is varied until the required temperature (and hence thermal dose), as seen using MR thermometry, is reached. During the treatment delivery phase, some indicator of tissue change is desirable. This enables assessment of treatment progress, and may also provide feedback to allow adjustment of exposure parameters in real time. For MR guided HIFU, the temperature rise could be determined using spinlattice relaxation time (T_1), proton resonance frequency (PRF) or proton diffusion (D) related sequences [78]. For US guided treatments, the most commonly used indicator of tissue ablation is the appearance of a hyperechoic region on the image, but other techniques such as elastography and ultrasound thermometry are under investigation [78]. The final component of the HIFU procedure is post-treatment assessment of the extent of tissue ablation. Contrast enhanced MR and ultrasound imaging allow visualisation of vasculature. Successful HIFU ablation leads to occlusion of blood vessels in the target volume, and thus reduced contrast uptake following treatment [79]. More details about HIFU's guidance methods are given in 1.4.6 paragraph.

1.4.5 THE TREATMENT DELIVERY

The guiding principle of HIFU is that an ultrasonic beam should be able to destroy a sharply defined region of tissue rapidly. Focusing of the ultrasound beam may be achieved in a number of ways. The simplest method is to use a single element spherical shell of piezo-electric material capable of delivering high power. Whereas quartz was the transducer material of choice in the early days of HIFU, recent developments have seen the use of piezo-ceramics such as PZT (lead zirconate titanate) and piezocomposite materials. The single element focused bowl transducer gives no flexibility in order to

define the focal length. Different focal lengths may be achieved by combining a plane single element transducer with lenses of different specifications. Lenses are usually made from materials having a speed of sound greater than that of water, and thus are of concave shape when a convergent beam is sought. Good impedance matching is required in order to minimise energy loss at the transducer–lens interface. Maximum transmission is obtained when the transducer and lens are separated by a quarter wavelength of impedance matching material. Fry [80] achieved energy localization by using four plane transducers each fronted by a plano-concave lens. The beams were arranged in such a way that their foci overlapped, and the intensity was maximised by optimal phasing of the individual beams. This method requires the availability of four separate acoustic windows. Emerging phased array technology for high power ultrasound applications has led to the design of transducers that allow electronic beam steering to facilitate more rapid treatment of clinically relevant volumes [81–82]. The acoustic energy may be delivered in a number of ways. A single exposure (typically 2–10 s of duration) may be made with the transducer held stationary. This results in a well-demarcated ‘‘lesion’’ of dimensions determined by the focal region of the transducer. Where larger volumes are to be targeted, the transducer could be moved in discrete steps, and fired at each position, where the distance between ‘‘shots’’ will determine whether lesions are overlapping or separate, depending on the necessity to achieve confluent regions of cell killing (Figure 1.8). An alternative exposure strategy is to move the active therapy transducer in pre-determined trajectories (e.g. linear tracks or spirals) to conform with the required treatment volume. If the correct combination of transducer velocity and ultrasound energy is used, these result in confluent volumes of cell damage.

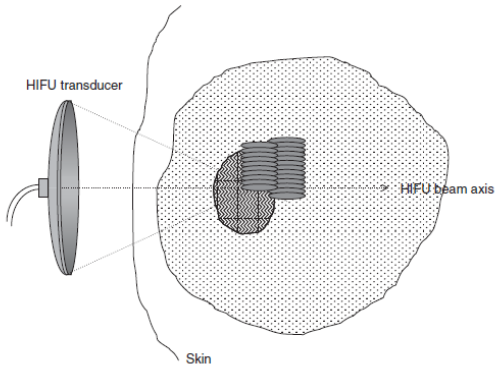

Figure 1.8 Diagrammatic illustration of HIFU treatment delivery for the ablation of large tissue volumes. Multiple lesions are created side-by-side to span the required treatment volume, starting on the side distal to the transducer. The lesions can be overlapping or separate, depending on the necessity to achieve confluent regions of cell killing.

1.4.6 EXTRACORPOREAL DEVICES

Tissue targets lying within the breast, abdomen, brain or limbs are usually treated using an extracorporeal HIFU source. Trans-cutaneous treatments of this nature require that there is a suitable acoustic window on the skin that provides a propagation path for the focused beam that is uninterrupted by intervening gas. In addition, it must be possible to couple the ultrasound energy to the skin surface using coupling gel, a water balloon or other suitable liquid path. During last 20 years, many prototype extracorporeal devices have been used in feasibility studies [83-84]. Extra-corporeal devices fall into two types—those for which the treatment is guided by magnetic resonance (MRgFUS) and those for which ultrasound imaging is used (USgFUS). There are advantages and disadvantages to each imaging modality for use with HIFU that are described below. MRgFUS can provide information on functional and physiological parameters of tissue, including diffusion, perfusion, flow, and temperature. This latter capability is particular useful in HIFU therapy because it can be used to detect tissue damage induced by thermal ablation. MRgFUS is the only currently available technique with proven capabilities to create quantitative temperature maps during the treatment. Tissue temperatures in the therapeutic ultrasound field are available within approximately 5s after treatment completion, with a resolution of approximately 1°C [85]. Follow-up evaluation of HIFU induced lesions can also be done by MRI. The high correlation of lesion formation with temperature provides a means to measure the treatment volume

and quantify tissue damage. At present, there are 3 temperature-sensitive parameters for MRgFUS. The first one is related to the molecular diffusion coefficient (diffusion coefficient) is used for thermometry, it often takes 2 to 3 min to obtain an image, which is too slow for real-time monitoring. Two other parameters are commonly used, including proton resonance frequency shift (PRFS) and longitudinal relaxation time (T1). However, it will be very difficult to monitor the temperature changes of the tissue when the patient movement occurs during HIFU, this may limit application of HIFU technology. The temporal resolution is limited in MRgFUS due to the slow image acquisition frame rate [86]. Hence, MRgFUS is inherently not real time, resulting in temporal misinterpretation of temperature profiles and lengthened treatment times. The use of MRgFUS provides high spatial resolution in an arbitrary plane. MRgFUS enables an accurate assessment of the extent of tumor infiltration and stage as well as the critical surrounding structures. As a result, MRgFUS is an invaluable tool for planning the most precise ablation trajectory for a focused US beam. Both MRgFUS and USgFUS-guided techniques can be used to measure the distance between the skin and the superficial or deep surface of the tumor, regardless of whether the involved skin and chest wall areas can be directly imaged. However, MRgFUS has been shown to be more precise and reproducible than US in determining the exact location and extent of breast cancer in a given patient, as well as the amount of intraductal spread. The improvement of 3T MRgFUS from the previous 1.5T MRgFUS further increases the ability of MRgFUS to define tumor borders [87]. High costs are associated to MRgFUS; it also requires a special environment that can hinder patient accessibility; a minimal use of metal parts in the HIFU assembly is necessary to prevent distorsion of the MRgFUS images and in addiction the MRgFUS is not appropriate for patients with magnetic metal implants. The resulting artifacts influence the quality of imaging, and more importantly, implants may endanger patients during HIFU therapy.

Ultrasound guided system (USgFUS) has not the possibility to create quantitative temperature maps during the treatment but many studies have demonstrated that US grey-scale change is reliable for monitoring the temperature response to HIFU treatment in real-time. While the temporal resolution is limited in MRgFUS, USgFUS guidance provides real-time imaging at a relatively low cost, although with a limited field of view, spatial resolution, and contrast resolution. Using real-time USgFUS monitoring, treatment effects can be assessed by immediate gray-scale changes. By examining this feedback, operators can control the thermal dose delivered. Increasing the ultrasonic

greyscale level in the target volume is generally considered a signal of effective treatment and is caused by coagulative necrosis of the target lesions, cavitation bubbles, and other unidentified factors. By examining the appearance of the hyper-echoic area, complete necrosis can be assessed and breast skin burn can also be identified. After ablation, it is not easy to observe remaining active lesions or the focal point [87]. Ultrasound provides a more rapid imaging technique, but as yet real time imaging of the ablated volume has proved difficult in the absence of bubbles, although rapid elastography methods are being investigated [88]. When gas bubbles are produced by acoustic cavitation or boiling, hyperechoic regions appear on the ultrasound image and these have been shown to be a good indicator of tissue damage [89]. Low costs are associated to USgFUS; moreover, US-guided HIFU does not have contraindications such as the artefacts influence on the quality of imaging, and, more importantly a special environment is not required, even ferromagnetic devices are allowed during HIFU therapy.

Clinical results have been reported from prototype extracorporeal devices [83, 90] but results from two commercially devices are available [91-92]—these are the Exablate (from Insightec) (figure 1.9A) and the JC Tumour therapy device (JC-Haifu) (figure 1.9B). Early reports from these studies have been encouraging [93-94]. Visioli et al. (1999) [83] published their preliminary phase I clinical trial results for the treatment of soft tissue tumours, including those of liver, using their own clinical prototype (1.7 MHz, focal peak intensity in situ 1500 Wcm^2). Both system have demonstrated that HIFU could be used as an outpatient procedure without anaesthetic or other sedation, with liver motion being reduced by patient breath holding. There are a large number of reports of the results from clinical trials of the treatment of liver cancer, all using the Chongqing HAIFU device [91, 95]. Experimental studies of kidney ablation have been reasonably successful [96-98]. Marberger et al. (2005) [99] reviewed the use of HIFU for the treatment of renal tumours. They concluded that the kidney provides a more challenging target than other organs, but that the results from China [100] give cause for optimism that the problems of rib shielding and respiratory motion can be overcome. Illing et al. (2005) [101] have also reported encouraging results in renal tumour treatment. The breast is in many ways an obvious target for HIFU as access is relatively simple, tissue movement is not a problem, and ultrasonic and MR imaging of the breast is well established. Using MR guidance, fibroadenomas and malignant breast tumours have been treated [92]. Cancers of the bladder, pancreas and bone have also been

targeted by ultrasound guided HIFU [90,96, 102]. The potential for HIFU treatment of uterine fibroids has been explored both experimentally [103] and clinically [104-105]. It's clear advantages are its non-invasive nature, the ability to achieve high spatial specificity, the potential for retreatment or use of other therapeutic modalities after its use, and its low side effect profile. Ultrasound will not penetrate air filled viscera, and so cannot be used in, for example, the lung or bowel, although it may be effective on their surfaces. The current restrictions to treatments in the brain due to the presence of the skull may be overcome using time reversal techniques [106-107]. HIFU treatments are lengthy at present, but methods of speeding up treatments are actively being sought, using sophisticated ultrasound delivery modes and for example, contrast agent microbubbles, to increase the rate of tissue destruction [108]. Early fears that HIFU might stimulate metastatic spread of cancer have not proved founded [109-110].

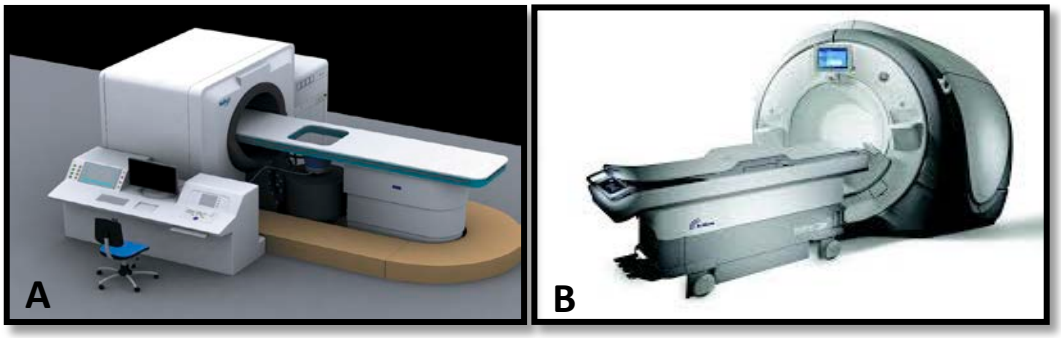

Figure 1.9 Two commercially available extracorporeal devices: Exablate (from Insightec) (figure 1.9A) and JC Tumour therapy device (Chongqing HAIFU company) (figure 1.9B).

1.4.7 TRANSRECTAL DEVICES

The transrectal devices that have been developed for the treatment of benign and malignant prostate disease have probes that can be inserted in the rectum and which incorporate both imaging and therapy transducers in one unit [111-112]. Based on this technique there are 2 commercially available transrectal devices. They are undergoing multicenter evaluation to assess their role in the management of prostate cancer [113]. The Sonablate 500 transrectal device (Focus Surgery; Milpitas, California) uses a 4-MHz curved lead-zirconate-titanate transducer with a dimension of 3.0 x 2.2 cm for treatment. The central, circular, 12-mm-diameter portion is used for imaging. The focal

length can be 3.0, 3.5, 4.0, or 4.5 cm. The intensity at the focus is 1680 to 2000 W/cm^2, depending on the focal length [114]. The second device is the Ablatherm® (Technomed International, Lyon, France) system. This device includes a motorized probe-positioning system, ultrasound power generator, a cooling system for preservation of the rectal wall, and the ultrasound scanner [115]. Treatment (or thermal ablation) treats prostate cancer by focusing high-intensity ultrasound waves on the affected area, causing localized heating that destroys the cells in the gland without damaging the surrounding tissue. Focused ultrasound works in the same way as rays of sunlight that pass through a magnifying glass and are concentrated at a single point, causing a significant temperature rise around the focal point. Both systems incorporate therapy and imaging transducers into a treatment head mounted at the end of a trans-rectal probe. The therapy transducer takes the form of a truncated spherical bowl. The clinical aim of both devices is usually to ablate the entire prostate, although nerve sparing treatments are sometimes required. Prostate ablation is achieved by placing touching lesions side by side. In the Ablatherm® device, lesion length is varied by adjustment of the ultrasound power to pre-set levels, whereas for the Sonablate™ the thicker prostates are ablated using two layers of lesions, the deeper layer being created using a longer focal length than the more superficial layer. The different focal lengths are achieved by rotating the transducer, the two sides having different geometries. Sonablate™ users are able to vary the acoustic output power of the probe.

1.4.8 INTERSTITIAL DEVICES

There has been some interest in the development of high intensity ultrasound probes for interstitial use. In the main, these use plane transducers rather than focusing elements, and volume destruction is obtained by rotation of the probe. Prat et al. [116, 117] have described a probe designed for the intra-ductal treatment of biliary tumours. A 3mm x 10mm 10MHz plane transducer is mounted on a stainless steel shaft that is passed through a jumbo fiberduodenoscope. The probe can be positioned under fluoroscopic guidance. Ultrasound intensity at the transducer face of 14Wcm^{-2} is used for 10–20 s bursts. Circumferential ablation is achieved by rotation of the flexible probe. The transducer is rotated by 18° after each ‘‘shot’’. Once 360° of damage has been achieved the probe is repositioned under fluoroscopic guidance to create adjacent rings, each

8mm in height. This has been used clinically with some encouraging results [118, 119]. A similar device has been created for the treatment of esophageal tumors [120]. A 15mm x 8mm 10MHz piezoceramic plane transducer is mounted on an 80cm long, 10mm outside diameter flexible shaft. Intensities of 12-16Wcm^{-2} for exposure times of 5–20 s gave ablation to a maximum depth of 13mm in ex vivo liver. In the oesophagus ex vivo a 10 s exposure at 12Wcm^{-2} resulted in damage to a depth of 4–5mm. A similar MR compatible device has been developed. Makin et al. [121] have also developed a probe for percutaneous and laparoscopic treatment of the liver. The probe consists of a (32 3.1MHz) element imaging and therapy array with 2.3 mm elevation, 1.53 mm pitch and 49 mm aperture. Rotational treatments can be undertaken. The ability of high intensity ultrasound beams to occlude the blood supply and coagulate tissue has been exploited in the design of a device to allow bloodless partial nephrectomy [122]. A 3.8MHz, 1.2 cm^2 plane transducer mounted on a handheld applicator is used at intensity at the transducer face of 26Wcm^{-2}.

1.4.9 CLINICAL APPLICATIONS

While focused ultrasound is in the early stages of development and adoption, it has the potential to transform the treatment of a variety of serious medical conditions. Some applications of the technology are approved for commercial use and are available in medical treatment centers around the world. Other uses are still undergoing research, with opportunities for patients to participate in clinical trials at leading medical research institutions [123]. Even more potential uses of the technology are in the early stages of technical research. Today, focused ultrasound can be used in the treatment of various conditions in the human body, these conditions include the following:

Prostate Cancer -This is treated via the insertion of a rectal ultrasound probe into the rectum. This insertion allows better access to the prostate [125].

Kidney Cancer - HIFU is a non invasive method of treating kidney cancer which leaves the patient with no need for dialysis as compared with the other methods like surgery or radiotherapy[126].

Liver Cancer - Cancer that was normally managed by surgery can now be treated with focused ultrasound. Other cancers that can be treated with this ultrasound are bone cancer, pancreatic cancer [126].

Atrial Fibrillation - Abnormal rhythms of the heart can be treated by ablating the heart tissue that is responsible for causing the arrhythmias [127].

In total there are more than 82,000 patients treated with focused ultrasound. A majority of patients treated have had prostate cancer, followed by uterine fibroids and liver cancer.

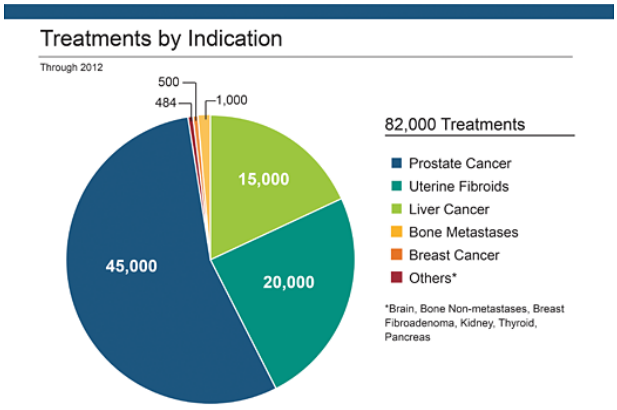

Figure 1.10. Patients Treated

The future of focused ultrasound

There are many clinical studies in the field of focused ultrasound with the aim of replacing the standard invasive surgical procedures with this non invasive technology. Research is being conducted to advance the accurate administration of focused ultrasound waves to internal organs using MRI technology.

1.4.10 HIFU LIMITATIONS

Safety is paramount in developing any new technology. It is important to consider the safety, side effects, and limitations of the treatment. A clear knowledge of expected and hazardous side effects is critical in order to achieve regulatory approval and for a patient to give fully informed consent for a procedure. It has been shown to be successful for

the treatment of liver tumors in the former [129] and in the selective destruction of normal liver, bladder, muscle, and kidney in the latter [130]. Small-animal studies have also shown that HIFU does not increase the risk of tumor metastasis [109]. Studies involving transrectal HIFU for the treatment of prostate cancer have recorded side effect profiles [113]. The most serious complication described is rectal wall injury. Although, after improvements in device-design and safety features such as rectal wall cooling, this particular complication occurs very rarely at less than 1%. The other side effects are disease specific, with urinary incontinence (<5%) and impotence (≈50%) being the most common. The general consensus from all studies to date has been that extracorporeal and transrectal HIFU are both safe and acceptable to patients. The adverse effects of the HIFU process have been reported in previous studies. First, on the basis of clinical experiences in China [102] it can be seen that the duration of HIFU treatment is long. The procedure takes several hours and the patients must lie on the therapy platform, making them uncomfortable and causing unnecessary deposition of energy in the surrounding tissues. This procedure may cause adverse events such as skin burns, transient pain, and nerve injury. Kennedy et al. (2004) [131] reported that the most severe treatment-related adverse events were transient pain and superficial skin burns in their study for the HIFU treatment of 11 patients with liver tumors. Second, a few live cells may be left in the targeted area after HIFU ablation. Spaces between extremely small focal regions of HIFU may result in the survival of a few cells in the focal area [132].Third, ablation and blocking of micro vessels smaller than 0.2 mm in diameter is achievable with HIFU, but it is less effective with vessels 0.2 mm in diameter and larger because rapid blood flow may reduce HIFU energy absorption, preventing it from depositing sufficient energy in the target zone within a short time [102]. These adverse effects may be due to small throughput and long treatment time. Therefore, HIFU energy deposition should be enhanced in a much shorter time. Factors related to HIFU energy deposition in HIFU therapy consist of the acoustic intensity of transducers, energy absorption characteristics of tissues and the exposure duration. Theoretically, high acoustic intensity or prolonging duration of sonication can change small throughput. However, there is always a risk of depositing more energy to the overlying tissue. The resulting effect is a longer ablation time for patients with an increase in the incidence of adverse effects and the technical difficulty of providing treatment. Many studies have focused on how the tissue characteristics of acoustic absorption can be changed to make energy deposition more efficient [133-134]. In order to enhance the

HIFU ablation efficiency, heating, cavitation, and mechanical events in the target tissues should be enhanced [135-136]. Several types of materials such as iodized oil, porphyrin, and ultrasound contrast agents have been investigated for enhancing energy deposition in tissue in the past [137]. In particular, ultrasound contrast agents have been intensively studied to enhance the effect of HIFU therapy.

1.5 THERAPEUTIC ULTRASOUND: DRUG ENHANCEMENT USING MICRO-NANOBUBBLES

Although therapeutic ultrasound was considered a tool for hyperthermia or thermal ablation of tumors for over 40 years, more recently new mechanisms for ultrasound-based or ultrasound-enhanced therapies have been described, and there is now great momentum and enthusiasm for the clinical translation of these techniques [138]. Ultrasound has been proposed as an innovative method for noninvasive delivering of drugs and genes to different tissues. To target and deliver drug and gene, microbubbles has been the subject of intense experimental research [139]. Encapsulated gas microbubbles are well known as ultrasound contrast agents for medical ultrasound imaging. While the use of microbubbles as contrast agents has been around for perhaps a couple of decades, the use of microbubbles for therapy is in its infancy [140].

In diagnostic ultrasound, microbubbles create an acoustic impedance mismatch between fluids and tissues to increase reflection of sound. Accordingly, these new contrast agents increase the signal from flowing blood and vascularized tissues containing blood. Ultrasound contrast agents should have extensive ultrasound applications in radiology and cardiology for the detection of perfusion and characterization of tissues [140]. It is only recently, however, that the new generation of blood pool agents has become available for routine diagnostic applications, and subsequent clinical experience will produce guidelines for the use of these agents [140]. The application of microbubbles (MBs) in diagnostic as contrast-enhanced ultrasound has become an indispensable part of clinical ultrasonography [141], and molecular imaging via ultrasound has recently attracted significant attention [142]. MBs help to enhance the specificity and sensitivity

of imaging for various types of diseases, especially with tumors [143]. Other advantages of using MBs include a lower cost of contrast agents, an opportunity for real-time observation and the elimination of the exposure to radiation. However, compared with contrast agents for computed tomography (CT) and magnetic resonance imaging (MRI), MBs are much larger. Microbubbles used for clinical imaging are typically between about 1 and 10 μ in diameter (the upper limit for passage through the lung capillaries); Usually, the diameter of a microbubble is approximately equal to the size of a red blood cell, resulting in similar rheology in the microvessels and capillaries throughout the body following intravenous administration [144]. Recently developed nanoscale bubbles (nanobubbles [NBs]) are promising contrast agents for extravascular ultrasonic imaging. Nanoscale ultrasound contrast agents with various shells (polymers or phospholipids) and cores (gas, liquid, or solid) have been fabricated and exhibit good contrast enhancement. Over recent years, the potential use of nanobubble systems combined with US has gained growing amounts of attention not only for diagnostic applications as contrast agents, but are currently the subject of much research in relation to their potential use as therapeutic tools: they can also be used as drug and gene carriers. The nanobubbles as drug/gene carriers have an average size less than that of red blood cells, i.e. they are capable of penetrating even into the small blood capillaries and releasing drug and genes under the action of ultrasound field. The application of ultrasound and nanobubbles to targeted drug and gene delivery has been the subject of intense experimental research. Under exposure of sufficiently high-amplitude ultrasound, these targeted nanobubbles would rupture, spewing drugs or genes, which are contained in its encapsulating layer, to targeted cells or tissues. Recently, targeting ligands are attached to the surface of the nanobubbles (i.e. targeted-nanobubbles), which have been widely used in cardiovascular system and tumor diagnosis and therapy. This technique presents a variety of advantages, including: non-invasiveness, local applicability and proven safety [145-146]. Nanobubbles with various shells (polymers or phospholipids) and cores (gas, liquid, or solid) have been fabricated and exhibit good contrast enhancement. However, research on NBs is still in the initial stages.

In the following paragraphs I will describe the main proprierties of nanobubbles with a particular attention to their interactions with ultrasound and their applications in therapeutic ultrasound.

1.5.1 GENERAL PROPRIETIES OF NANOBUBBLES

Nanobubbles (NBs) are comprised of spherical voids or cavities filled by a gas. Generally, for medical applications, nanobubbles are stabilized by a coating material such as phospholipids, surfactant, denatured human serum albumin or synthetic polymer.

Since gas is less dense than liquids or solids, nanobubbles comprise a pocket region or structure of low density. This property of low density of NBs has a number of potentially important medical applications. These include site-specific delivery and treatment of thrombosis and pulmonary delivery [147]. One way of exploiting the diagnostic and therapeutic applications of nanobubbles is with ultrasound. Ultrasound is one of the most common medical imaging methods and is also used therapeutically. Sound travels more slowly in gas than it does in liquid. The difference in speed of sound in nanobubbles creates an acoustic impedance mismatch between tissue and blood surrounding a nanobubble. Nanobubbles are efficient reflectors of ultrasound energy, hence their use as contrast agents for medical ultrasound imaging. Nanobubbles also lower the threshold for cavitation with ultrasound. Ultrasound energy can be reflected, transmitted or absorbed as it passes through a biological medium. In cavitation, ultrasound energy is concentrated within a domain around a nanobubble. Nanobubbles can be used as therapeutic cavitation nuclei with ultrasound (see next paragraph). The frequency of ultrasound is also important. Cavitation is generally more efficient (i.e., easier to produce) at lower frequencies of ultrasound. Cavitation can be used therapeutically at clinically useful ultrasound frequencies such as 1 MHz.

The nanobubbles must be sufficiently stable, that after injection into the blood, they will circulate for a long enough period of time to reach the target site. The stability of nanobubbles in liquid (e.g., a biological fluid such as the blood) depends upon the surrounding medium-temperature, pressure, concentration of dissolved gases, the composition of the gas in the bubble and the coating material surrounding the nanobubble. Elevations in pressure, such as occur in the heart and arteries during systole pose a stress on bubbles. An important parameter to consider in the development of stable bubble systems is the Laplace pressure, which governs the in vivo dissolution rate of nanobubbles. The gas pressure within a bubble is the sum of the equilibrium pressure, the Laplace pressure and the blood pressure. The Laplace pressure is the

pressure difference between the inside and the outside of a bubble (or a droplet) in the bloodstream [148], given as:

$$\Delta P = P_{inside} - P_{outsode} = \frac{2\sigma}{r} \quad (8)$$

where P_{inside} and $P_{outside}$ are the pressures inside and outside a bubble respectively, σ is the interfacial tension, and r is the bubble radius. A surfactant layer on the bubble surface is able to reduce the interfacial tension and decrease the Laplace pressure. As the Laplace pressure is reversely related to the size of a bubble, in accordance with the equation, smaller bubbles will have higher pressure values than larger bubbles. When the inner gas leaves the core, the bubbles shrink and the Laplace pressure increases, thereby accelerating the rate of gas dissipation and the resulting bubble shrink age until the system ruptures [149].

The solubility of the gas in the nanobubble has an important effect on the stability of the nanobubble. Simple air bubbles dissolve very rapidly in the blood under the combined action of Laplace pressure, arterial pressure, oxygen metabolism and ultrasound energy, hence have little utility. Nanobubble formulations can be stabilised by using a gas with a very poor aqueous solubility for thebubble core, such as perfluorocarbons (i.e. perfluorobutane) or sulphur hexafluoride, thereby reducing the dissolution of the gas into the bloodstream. For example, the encapsulation of suitable perfluorocarbons (gases that are insoluble in water) has been proposed to increase the duration of various bubble systems. Nanobubbles comprised of perfluorocarbon (PFC) gases, which have a higher molecular weight, have a longer residence time in the blood. Perfluorochemicals, and in particular PFCs, when used as the filling gas or part of it, delay bubble dissolution very effectively, due to very low water solubility, thus providing ample time for patient examination. The preferred PFCs are those that combine low water solubility and high vapour pressure. In the US, there are currently two perfluoropropane-based nanobubble products marketed for diagnostic imaging with ultrasound. One of these products, DefinityR, was developed by ImaRx and is currently marketed by Bristol-Myers Squibb for diagnostic ultrasound imaging. The other currently marketed product is OptisonR, nanobubbles stabilized by human serum albumin.

As I shown before, nanobubbles remain relatively stable in water for a long time (they have a long lifetime), or rise very slowly, gradual shrink, and finally collapse (i.e., shrinking collapse), whereas macrobubbles increase in size, rise rapidly, and burst at the

water surface. Figure 1.11 shows the key differences among macrobubbles, MBs and NBs. MBs tend to gradually decrease in size and subsequently collapse due to long stagnation and dissolution of interior gases into the surrounding water, whereas NBs remains as such for months and do not burst out at once [150]. It has been revealed that the interface of NBs consists of hard hydrogen bonds similar to those found in ice and gas hydrates. This in turn leads to reduced diffusivity of NBs that helps to maintain adequate kinetic balance of NBs against high internal pressure.

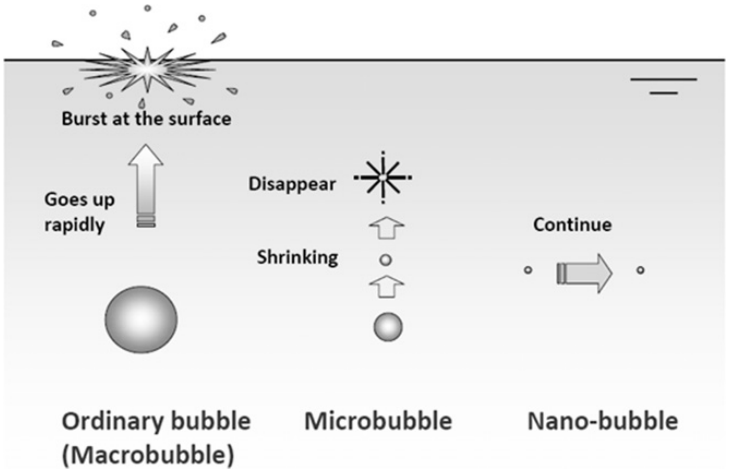

Fig. 1.11 Schematic diagram showing macro, micro and nanobubbles [151].

A further key factor to consider in bubble formulation is the shell composition. First of all, the composition of the shell can greatly influence bubble half-life, since it affects the gas exchange from the core to the external medium. The thickness and the elasticity of the shell determine microbubble stability [152]. Exposure to intense US energy can lead to rapid bubble destruction by cavitation due to their rapid contraction and expansion. This mechanical stress can weaken the bubble shell until bubble rupture [153]. Very soft shells can be ruptured by small pressure variations, but very hard shells would be not being able to oscillate. The most elastic shells are made of phospholipids [152]. The types of hydrocarbon tails of these lipids can also affect the shell properties. For example, saturated diacyl chains provide greater rigidity, often accompanied by lower gas permeability, compared to shorter chain lipids. As a consequence, microbubbles consisting of lipids with longer acylchains exhibit longer shelf-lives [154-155]. The presence of abundant surface electrostatic charges could disturbthe stability of phospholipid monolayer shells causing lateral electrostatic repulsions [156]. One way

of increasing the resistance of phospholipid monolayer-based microbubbles is to add polymers to the formulation [157-158]. The influence of polymers on bubble structure has been widely investigated. Lindner and colleagues studied the elasticity of polymer-albumin microbubbles by varying the polymercomposition in order to vary the shell properties [159]. Polylactides (PLA), low and high molecular weight poly-mers, and caprolactone were tested.

1.5.2 TERAPUTIC APPLICATIONS OF NANOBUBBLES

In paragraph 1.2.1.2 the bubble behaviour when subjected to an acoustic field and the biofisical effects provoked by cavitation has been described. Here, I will describe different methods of combining drugs with nanobubbles and the innovative technologies that allows therapeutic local administration of oxygen, drugs or other molecules transdermally (sonophoresis) or directly at the cellular level (sonoporation).

1.5.3 DRUG CONTAINING NANOBUBBLES

For drug delivery applications, it is possible to make therapeutic drug-carrying nanobubbles by incorporating the drugs into or onto the bubbles. As shown in Figure 1.12, drugs can be incorporated into acoustically active carriers in a number of different ways, ranging from association with the membrane to development of gas/ drug-filled microspheres. Drugs can be conjugated to the nanobubble membrane with the use of a charge dependent, noncovalent binding. Especially DNA that is a large negatively charged molecule is suitable for attachment to a positively charged membrane. Another mechanism to load a bubble with drugs is to incorporate the drug in the shell. This process is importantly influenced by the nature of the drug, in terms of lipophilicity and hydrophilicity. Although it seems difficult to enclose material within the nanobubble itself, as it is a gasfilled microsphere, theoretically a drug containing powder may be attached to the inside of the bubble wall. Furthermore, drugs can be bound by ligands that are embedded in the membrane. With respect to this type of conjugation, a specific technique which is based on an avidinebiotin model, used for binding of antibodies in other studies, may be of importance for the binding of certain drugs. Finally, even nanobubbles with multiple layers can be constructed, in which drugs can be dissolved.

The presence of gas in the drug delivery vehicles is to confer acoustic activity. The presence of the gas lowers the threshold for cavitation making the drug carriers sensitive to ultrasound for local activation, drug release and drug delivery. Additionally, drug delivery and release can be visualized with real-time ultrasound. These studies clearly suggest that nanobubbles can be used as a vehicle for drugs, and bubble destruction by high acoustic pressure ultrasound can be used for local delivery of materials attached to or entrapped in the bubble. As mentioned earlier, cavitation is probably the mechanism by which destruction of nanobubbles enables extravasation of red blood cells and increases cell permeability; however, the exact process is not clear and needs further investigation.

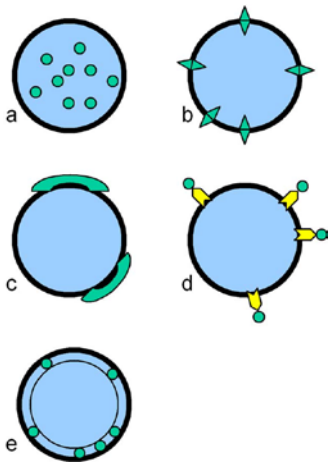

Figure 1.12 Several mechanisms to attach drugs to nanobubbles. a: Incorporation in the bubble; b: incorporation in the bubble membrane; c: attachment to the membrane; d: attachment to a ligand; e: incorporation in multilayer nanobubble [160].

1.5.4 NANOBUBBLES AS GENE DELIVERY SYSTEMS

Gene therapy, a promising therapeutic option for the treatment of genetic or acquired diseases, is based on the ability to introduce new genetic material into hosts. A major obstacle to gene transfer is the fact that naked nucleic acids are not efficiently taken up by cells due to their negatively charged phosphate groups, relatively large sizes and hydrophilic nature. Moreover, they are very susceptible to degradation mediated by nucleases present in the blood. To overcome these limitations, a number of gene delivery vectors have been developed, falling into either viral or non-viral categories. Micro- and nanobubbles provide a promising non-viral strategy for the site-specific

delivery of genetic material; this is due to their potential to be ‘activated’ in the presence of ultrasound (US) and mediate the delivery of DNA to specific cell targets. The insonated nanobubbles technique as a gene delivery system has become increasingly popular over recent times due to its versatility and ease of the use. The effect of US on cell permeability and its capacity to facilitate the entry of naked DNA into cells was first described by Fechheimer [161]. These first studies used a US frequency in the range of 20–50 kHz. However, when combined with cavitation these frequencies are able to induce tissue damage [162-163].To overcome this limitation, the delivery of genes using US at the frequencies applied for clinical imaging (1–3 MHz) has received a great deal of research attention. However, as these conditions result in very inefficient gene delivery, therapeutic ultrasound combined with nano/microbubble contrast agents has been investigated for enhancing gene transfection efficiency [164-165]. This combination method has many of the characteristics required for practical gene therapy including low toxicity, the potential for repeated applications, organ specificity and broad applicability to acoustically accessible organs. Under proper conditions, the combination of ultrasound and nano/microbubbles can create transient non-lethal perforations in cell membranes. Numerous studies have now shown that US is able to result in the direct transfer of genes into the cell cytosol, although the level of gene transfer is generally very low (alternatively, it can be incorporated into the shell of a multilayer polymer nanobubble, thereby increasing the quantity of DNA vehiculated (Figure 1.13B). A third approach involves incorporating DNA into lipoplexes,polyplexes, liposomes or nanoparticles, which are subsequently associated with the bubble surface by means of either physical or chemical interactions [166-167] (Figure 1.13C).When loading DNA to the external surface of a nanobubblethrough non covalent binding (Figure 1.13A), the nanobubbles must bedesigned to possess a positive surface charge in order to favourthe electrostatic interactions with the negatively charged nucleicacids. The above findings suggest that the combination of nanobubbles and ultrasound could be useful for gene delivery (Fig. 1.13(c)) [149].

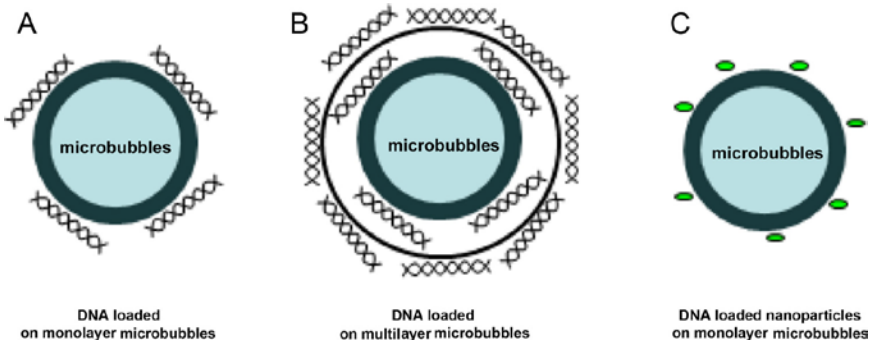

Figure 1.13. Technological approaches to attaching DNA to the micro-nanobubble shell. (A) Deposition on the surface of a monolayer-shelled bubble; (B) incorporation in amulti-layer shelled bubble; (C) binding of DNA-loaded nanocarriers onto the bubble shell.

1.5.5 TARGETED NANOBUBBLES

Targeted nanobubbles can be developed by incorporating targeting ligands onto the surface of the nanobubbles. As described earlier, nanobubbles can be loaded with genes and injected into a vein, followed by localized ultrasound. In this way, nanobubbles are a specific and local delivery is controlled by the local application of ultrasound. However, as currently used nanobubbles are relatively stable and circulate through the whole body, delivery of material could partly result in deposition of the contents of the nanobubble in tissue that is not the target tissue, e.g. in the chest wall, or in the lungs, in which nanobubbles with higher diameters are filtered. Therefore, it would be greatly desirable to have a nanobubble which can be targeted to a specific tissue by using ligands and receptors that are incorporated in the bubble shell (Figure 1.14). Using certain ultrasound imaging techniques (e.g., cavitation imaging), it is possible to detect a single nanobubble [168]. In terms of sensitivity to low concentrations of an imaging agent, ultrasound with nanobubbles rivals nuclear medicine and exceeds the capabilities of other commonly used imaging techniques such as magnetic resonance imaging and computed tomography. This would enable active attachment of nanobubbles to target tissue and create further possibilities for diagnostic imaging and therapy like local drug delivery to target lesions. The extreme sensitivity of ultrasound, to low concentrations of nanobubbles makes it feasible to do molecular imaging with targeted ultrasound contrast agents. An important difference, however, between ultrasound compared to

nuclear medicine is that the imaging agent is a microscopic entity or nanoscopic as opposed to a small molecule (e.g., a radionuclide chelate in nuclear medicine). This means that targeted nanobubbles may be larger entities than some nuclear imaging probes. Therefore, targets that are accessible via the vasculature are probably of greatest interest for the development of targeted nanobubble agents. Targeted nanobubbles have been developed into various types of tissue and processes, e.g., endothelialcells, thrombi, inflamed tissue and angiogenesis [160].

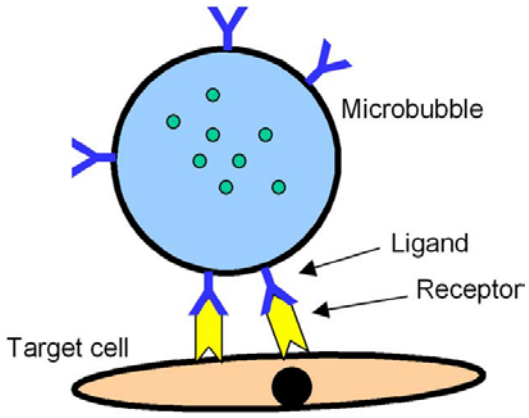

Figure 1.14. Targeted nanobubble, connected by ligand and receptor.

1.5.6 OXYGEN LOAD NANOBUBBLES

Oxygen is one of the most widely used therapeutic agents. It is a drug in the true sense of the word, with specific biochemical and physiologic actions, a distinct range of effective doses, and well-defined adverse effects at high doses. Oxygen is widely available and commonly prescribed by medical staff in a broad range of conditions to relieve or prevent tissue hypoxia. Hypoxia, a condition of inadequate oxygen supply to tissues or the body, can lead to severe tissue damage and can be life threatening. Tissue hypoxia can develop if there is a decrease in cardiac output (ischemic hypoxia), hemoglobin concentration (anemic hypoxia), or oxygen saturation (hypoxic hypoxia), or an increase in the metabolic demands of the body [169]. Hypoxia also induces physiological, cellular, and biochemical responses, which can effect pharmacological metabolism [170-171]. Hypoxia is the most crucial issue in the treatment of a variety of diseases, in particular in tumors. Tumors induce angiogenesis to increase their nutrient and oxygen supply, enabling their rapid growth [172]. However, the blood vessels in tumors are leaky and defective, with large pore cutoff sizes, and the endothelial cells are

misaligned or have large fenestrations [173]. Moreover, tumors have poor lymphatic drainage compared with normal tissues [173-174]. In general, acute mild hypoxia supports adaptation and survival. On the contrary, chronic extreme hypoxia leads to tissue loss. To solve this problem, in the recent years intensive research has been conducted to develop new carriers able to effectively release high oxygen amounts for sustained times [175-176]. Hemoglobin (Hb)-based oxygen carriers, using natural Hb as the oxygen transporting component, have been developed as cell-free suspensions, encapsulated within vehicles, or complexed with protective enzymes [175-176]. Researchers have also synthesized alternative carriers based on perfluorocarbons, which can carry molecular oxygen without actually binding to it, thus favoring gas exchange. However, they are not water-miscible, and therefore need to be formulated into emulsions for *in vivo* use [175-176]. Perfluorocarbon-based oxygen nanobubbles have been developed and reported to dissolve clinically relevant amounts of oxygen when administered in dosages that are approximately 1/500 of usual quantities in which perfluorocarbon-based oxygen carriers are administered [177]. Few years ago, our group developed a new kind of oxygen-filled nanobubbles, shelled with chitosan and cored with perfluoropentane, which proved to act as an efficient oxygen delivery system *in vitro* [178]. Oxygen bubble formulations were further optimized in order to reach the nanometer size range, and the new nanodevices, either coated with chitosan or dextran, were called oxygen-loaded nanobubbles (OLNs) [178-180]. Recently, nanobubbles have also been proposed to carry on molecules other than gaseous oxygen, such as DNA, thus opening the gates for future gene therapy applications [181].

1.5.7 SONOPORATION

The ability of nanobubbles to act as cavitation nuclei when destroyed can increase cell membrane permeability, if cells are located in close proximity to nanobubbles. Although ultrasound had been proven to increase cell membrane permeability on its own [182], the use of nanobubbles has a significant additive effect. Several explanations are offered for this phenomenon called ‘sonoporation’. First, nanobubbles, by acting as cavitation nuclei, can lower the threshold for cavitation (see paragraph 1.2.1.2). In body tissue or blood, cavitation sets fluid in motion and creates small shock waves that give rise to microstreaming along the endothelial cell. Destruction of

nanobubbles may cause high-energy microstreams, or microjets, that will cause shear stress on the membrane of an endothelial cell and increase its permeability [183]. This increase in permeability is probably due to transient holes in the plasma membrane and possibly the nuclear membrane (Figure. 1.15A). A second proposed mechanism, the generation of reactive oxygen species in endothelial cells under influence of ultrasound, was investigated by Basta et al [184]. As the use of nanobubbles together with ultrasound lowers the threshold for cavitation, this could possibly result in an increased production of free radicals, which are associated with cell killing in vitro and, as a consequence, may be also involved in enhancement of permeability of endothelial cell layers. A third interesting aspect is the rise in temperature in tissue following the application of high pressure ultrasound [185]. Bubble collapse following high energetic ultrasound can create high velocity jet streams that may cause a local, transient increase in temperature. As a rise in temperature influences the fluidity of phospholipid bilayer membranes, cell membrane permeability could possibly be changed directly as a consequence of the increased bilayer fluidity (Figure. 1.15B). Fourth, endocytosis or phagocytosis, active membrane transport mechanisms, may also be involved in the uptake of the bubble, bubble fragments or material entrapped in nanobubbles (Figure. 1.15C). A fifth mechanism by which the use of nanobubbles could facilitate the deposition of drugs or genes in a cell is exchange or fusion of the phospholipid nanobubble coating with the phospholipid bilayer of a cell membrane (Figure. 1.15D). This could result in delivery of the cargo of the nanobubble directly into the cytoplasm of the cell with the possibility of further uptake in endosomes or delivery to the cell nucleus.

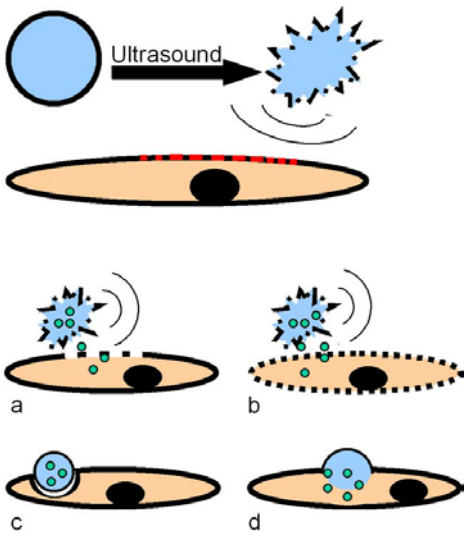

Figure 1.15. Destruction of nanobubbles by ultrasound resulting in increased membrane permeability by shear stress, temperature rise and activation of reactive oxygen species. Drug delivery by nanobubbles by: a: transient holes induced by shear stress; b: increase in membrane fluidity; c: endocytosis of nanobubbles; d: fusion of the nanobubble membrane with the cell membrane [186].

1.5.8 SONOPHORESIS

The skin has been investigated as route for drug administration for several decades and many drug delivery techniques to facilitate permeation of drugs across the skin have been explored. Sonophoresis describes the use of ultrasound to move low and high molecular weight drugs through intact living skin and into the soft tissues [187,188]. It is one of the most promising novel drug delivery system and has been shown to enhance the skin penetration and release rate of a number of drugs that have poor absorption/permeation profiles through the skin[189–192]. Sonophoresis is a localised, non-invasive, convenient, rapid topical administration method of delivering low molecular weight drugs as well as macromolecules into the skin [193]. This is a considerable technological advance compared to oral delivery because gastrointestinal degradation and first-pass metabolism through the liver are avoided [194]. Despite these advantages, the use of transdermal drug delivery (TDD) has been limited by innate barrier functions of the skin [195]. The epidermis is the functional barrier of the outermost part of the skin and protects the human body as a first-line defense against foreign substances such as bacteria and toxins. The skin, which consists of several layers including the stratum corneum (SC), epidermis, and dermis, is the primary

defense system of the body [196] (Figure. 1.16). The functions of skin include maintenance of body temperature, blockage of ultra-violet radiation, and providing a defense against harmful external pathogens such as bacteria and toxins. The most important layer of the skin that provides substantial protection from pathogens is the SC [197]. The SC is composed of corneocytes interspersed in a laminate of compressed keratin and intercorneocyte lipid lamellae, functions to conserve water and electrolytes, and is selectively permeable to certain substances such as drugs (see Figure 1.17). Naturally, the SC has a very low permeability to foreign molecules and is thus the main obstacle of TDD. Because of this barrier, available transdermal medicines are small molecules (<500 Da) that are active at low blood concentrations of a few ng/ml or less [198].

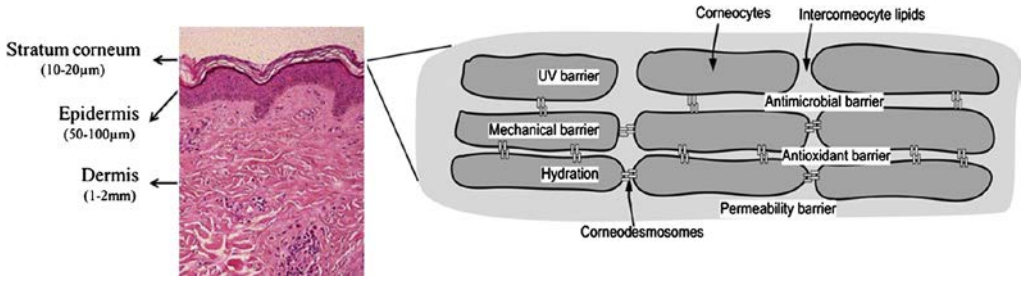

Figure 1.16. Cross section of human skin (left). Barrier function of the stratum corneum (right).

A number of methods have been proposed to overcome the natural barrier function of the skin, such as skin patches [199], iontophoresis [200], use of chemical enhancers [201], and ultrasound methods [202]. Recent research in sonophoresis has indicated that MHz range ultrasound has little effect on skin permeability even though 2–10 MHz is the most used frequency range in medical ultrasound imaging. On the other hand, low frequency (e.g.,100 kHz) ultrasound is better suited for the transdermal transport of various drugs such as insulin, erythropoietin and interferon [202-204]. Given that heat deposition is dominant at high frequency and cavitation effects are prominent at low frequency, the main mechanism for sonophoresis delivery is thought to be cavitational, and not thermal, effects [205]. The source of cavitation is believed to be small bubbles trapped in the skin during topical application of a drug solution and oscillation of these bubbles according to the applied ultrasound field. Since bubbles oscillate in asymmetric boundary conditions, microstreaming and asymmetric bubble collapse can occur [206]. Microstreaming can generate high velocity gradients and hydrodynamic shear stresses

[206]. Bubble oscillation around asymmetric boundary conditions by stable cavitation leads to a phenomenon called microstreaming, which can generate high velocity gradients and hydrodynamic shear stresses [206]. Microstreaming results from the unidirectional flow of fluid in response to bubble dynamics in an acoustic field. The characteristics of microstreaming are determined by fluid properties such as acoustic attention, viscosity, and density, as well as the ultrasound characteristics including temporal average intensity, frequency, transducer aperture size, and pressure amplitude. The velocity of microstreaming decreases with increasing fluid viscosity and increases with increasing acoustic attenuation. Collis et al. [207] studied several patterns of microstreaming and showed that many patterns are possible around a nanobubble. Each microstreaming pattern also generated different shear stress with distributions of compression and stretch in the vicinity of a bubble. The states of uniform shear stress and two types of divergence are illustrated in Figure 1.17

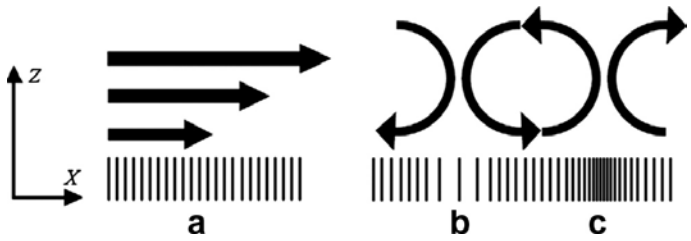

Figure 1.17. Illustration of the differences between uniform shear and surface divergence. (a) Uniform, high shear stress, no divergence and thus no stretch of cell surface, (b) high rate of positive divergence (as well as shear stress), cell/cell membrane in stretch-activated state, (c) high rate of negative divergence (as well as shear stress), and cell/cell membrane compressed together.

Teoretical and experimental studies have shown that microstreaming near a cell boundary can affect a cell membrane [208]. Second-order microstreaming flow may generate flow fields that develop shear stresses over a cell membrane, resulting in tension and stretching on membrane walls that cause channel activation, allowing delivery of compounds such as DNA for therapeutic purposes [209]. Asymmetric bubble collapse can induce jet streaming into the skin layer so that direct drug transport can occur. Therefore, an increase of cavitation is a logical way to increase skin permeability in sonophoresis. Adopting a low frequency ultrasound field is one way to increase existing bubbles in cavitation. When the frequency is low enough, it is assumed to be quasistatic field to sufficiently small bubbles. If small bubbles can rapidly grow

and collapse when adequately exposed to quasi-static rarefractional pressure, these bubble activities can be related to asymmetric bubble collapse. Figure 1.18 shows possible sites in which the cavitation effect may occur. Cavitation nuclei and air pockets in TDD can be formed in intracellular and/or intercellular structures. In addition, bubbles can be formed on the skin and coupling medium at the skin surface. However, small gaseous nuclei are more resistant to oscillation within densely packed tissue. This becomes especially apparent during high frequency (P ~ MHz) sonophoresis when skin density variations occur rapidly due to relatively short wavelengths in comparison to that at low frequency. Therefore, cavitation may preferentially occur within the coupling medium between the ultrasound transducer and skin surface and may locally increase skin permeability [206].

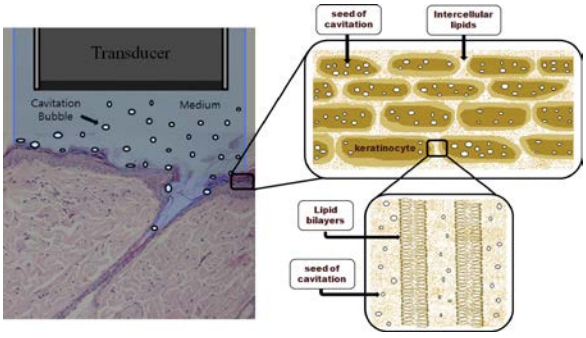

Figure 1.18. Schematic sketching of cavitation occurring in a variety of sites such as coupling medium, skin surface, and skin tissue. Cavitation occurs preferentially at the interface between keratinocytes and lipid bilayers.

Microstreaming is a characteristic of stable cavitation. For inertial cavitation, lower frequencies give bubbles more time to grow in the expansion cycle and consequently produce a more violent collapse during the compression cycle. The violent collapse of cavitation bubbles may generate either shock waves in the bulk of the liquid or a micro-jet near a boundary, which is referred to as asymmetric bubble collapse. Figure. 1.19 schematically shows the shock wave and micro-jet produced by inertial cavitation events. A spherical bubble collapse yields high-pressure cores that emit shock waves with amplitudes exceeding 10 kbar [210]. The disruption of a target exposed to such a pressure wave may occur through relative particle displacement, compressive failure, tensile stress, or shear strain [211]. When a bubble collapses asymmetrically nea ra boundary, it generally produces a well–defined, high velocity micro- jet [212]. Micro-jet distortion due to bubble collapse depends on the surface encountered by the bubble. If the surface is larger than the resonant size of the bubble (radius of 1–150 lm at

approximately 5 MHz–20 kHz), the resulting collapse will be in the form of a micro-jet (Figure 1.20).

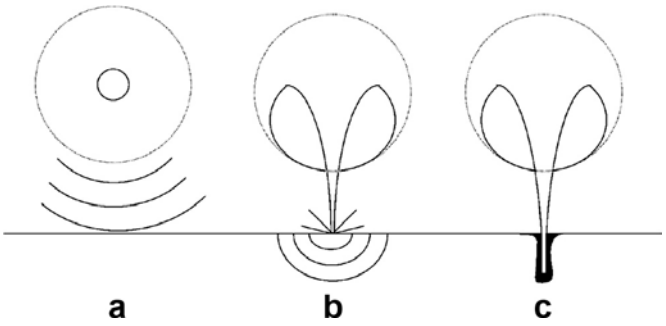

Figure. 1.19. Three possible modes through which inertial cavitation may enhance SC permeability. (a) Spherical collapse near the SC surface emits shock waves, (b) impact of an acoustic micro-jet on the SC surface, and (c) micro-jets physically penetrating into the SC.

As shown in Figure. 1.18 inertial cavitation has the potential to take place in keratinocytes, lipid bilayer regions, and crevices of hair follicles filled with coupling medium. Shock waves generated by inertial cavitation can cause structural alterations in the surrounding keratinocyte-lipid interface regions, resulting in the creation of diffusion channels through which drugs may be potentially delivered. Furthermore, impact pressure of the micro-jet on the skin surface may enhance SC permeability by disrupting SC lipid bilayers [213]. A micro-jet possessing a radius approximately one-tenth of the maximum bubble diameter impacts the SC surface without penetrating. When combined, these factors lead to lipid bilayer disorder and formation of aqueous channels in the skin through which drugs can permeate.

Transdermal delivery is perhaps the most widely recognized application of ultrasonically enhanced drug delivery based on the approval of the Sontra Medical (Echo Therapeutics, Inc) system for transdermal delivery of topical therapeutics in 2004 [214]. Numerous studies have been performed to confirm an enhancement of permeability by sonophoresis. Since the initial treatment of polyarthritis with hydrocortisone ointment by Fellingher and Schmidt in the 1950s, the transdermal delivery of therapeutic drugs such as fentanyl, caffeine, heparin, ketoprofen and insulin has become a major concern for clinical medicine. The field of sonophoresis is

intriguing. The pre-clinical evidence shows anecdotally that it may prove useful.However, many of the published studies, in general, lack sufficient scientific rigour.

1.6 THERAPEUTIC ULTRASOUND: OTHERS APPLICATIONS

Physiotherapy: Unfocused beams of ultrasound for physical therapy were the first clinical application, dating to the 1950s, which often has been referred to simply as “therapeutic ultrasound” [215]. This modality now typically has a base unit for generating an electrical signal and a handheld transducer. The handheld transducer is applied with coupling gel and moved in a circular motion over an injured or painful area of the anatomy to treat conditions such as bursitis of the shoulder and tendonitis by trained physical therapy technicians. The objective is to warm tendons, muscle, and other tissue to improve blood flow and accelerate healing. The coupling medium can also include various compounds for enhancing the treatment. Ultrasound application can assist by promoting transport of the compound into the skin, a method sometimes called sonophoresis. Drugs, such as lidocaine and cortisol, have been used extensively in sports medicine. The level of clinical benefit to the patient from physical therapy ultrasound treatments remains uncertain [215]. However, the risk of harm, such as burns, appears to be low when the modality is properly applied. The mechanism of action is known to be thermal. A non-focused beam with low-level energy deposition is typically used for physiotherapy. Overall, ultrasound for physical therapy has therefore provided a modest level of efficacy and patient benefit but also a low level of risk.

Lithotripsy: Lithotripsy has been the most common treatment for kidney stones since 1980s and continues to be the favored method for uncomplicated, upper urinary tract calculi, even with the advent of percutaneous surgical techniques. Ultrasound induced shock waves are used to disintegrate kidney and gallbladder stones. Main mechanisms studied in lithotripsy are erosion 5 [216], shear [211], and circumferential compression [216]. These mechanisms may all be activated to differing degrees by either the lithotripter shock pulse or the subsequent collapse of cavitation bubbles excited by the pulse.

Histotripsy: Histotripsy is a promising extracorporeal ultrasound technology that produces nonthermal tissue fractionation by cavitation (converting the targeted tissue into an a cellular liquid) [217]. Cavitation occurs when intense ultrasound pulses induce extreme pressure changes within the targeted tissue, resulting in the formation of a localized, highly dynamic cluster of microbubbles. These bubbles oscillate and violently collapse, producing localized stresses that mechanically fractionate and subdivide the targeted tissue, resulting in cellular destruction [218].

Bone healing and wound healing: There is some evidence in the literature that low intensity ultrasound can enhance repair rates and reduce healing times [219-220]. Dyson and Brookes (1983) [221] showed in their experiments in rat fibulae that when ultrasound exposures are carried out during the inflammatory and early proliferative phases of bone repair following fracture, healing can be accelerated, with direct ossification being observed. Mechanisms that have been proposed are signal transduction, gene expression enhancement, blood flow changes, tissue modeling or re-modeling effects or micro-mechanical stresses. There is experimental and some clinical evidence of the beneficial effects of very low ultrasound intensities on bone repair [222].

CHAPTER 2

MATERIALS AND METHODS

2.1. ULTRASOUND TRANSDUCERS CHARACTERIZATION: AN OVERWIEV

Before describing in detail the measurement techniques, it would be useful to consider in general terms which properties of the transducer fields are currently thought to be of most relevance to safety and quality control from a clinical point of view. Ideally, the full characterization of the ultrasonic field produced by a transducer would require knowledge of the distribution of acoustic pressure at every point of the space and at every instant in time. Probably one of the most commonly used parameter is the acoustic power. There are many methods for measuring the ultrasonic power, but currently the widely diffused is the radiation force balance. Despite its importance, ultrasonic power is not an exhaustive parameter. It gives a value of the energy output of the source, but doesn't give any information about how this energy is distributed in space and in time. Such information can be obtained by local measurements of other acoustic parameters such as acoustic pressure or intensity. Acoustic pressure can be measured directly with an hydrophone. Hydrophones, which could be considered as the equivalent of microphones for the ultrasonic frequencies, are tools able to generate an electrical voltage proportional to the acoustic pressure incident on their sensitive elements. Once the hydrophone has been correctly calibrated it is possible to know the

time variation of acoustic pressure in a measurement point from the electrical output of the device. So, by positioning the hydrophone within an ultrasonic field and acquiring its output electrical signal it is possible to reconstruct the shape, the amplitude and the pressure of the acoustic field generated by a transducer in the space. It should be noted that, in order to have information about the real parameters values in tissue during patient's treatment, the measurement should be conducted directly in tissues or in tissue mimicking materials. A large number of devoted tissue-mimicking materials (TMM) with specific and well-characterized physical properties have been studied and characterize during my work (see paragraph 2.5). Beside acoustic power and pressure, another important parameter, in particular for the clinical use, to provide a complete characterization of an ultrasonic field is the temperature increase in the focus region of the transducer in specified medium.

In this chapter, materials and methods for the characterization of ultrasonic transducers is described, while in the next chapter results obtained are shown.

2.2 ULTRASOUND TRANSDUCERS

Three Ultrasound-transducers are measured and compared:

- TRANSDUCER 1 (PTB-256, plane-wave transducer): 1.8611 MHz (Fundamental) and 6.2664 MHz (3^{rd} Harmonic);
- TRANSDUCER 2 (Sonic Concepts SU-102, HIFU transducer):3.5 MHz (Fundamental);
- TRANSDUCER 3 (Sonic Concepts H-106-MR, HIFU transducer):2.0 MHz (Fundamental) and 6.38 MHz (3^{rd} Harmonic)

The transducer's electric input for the excitation voltage is equipped with a (female or male) BNC connector. An electrical matching network, for HIFU transducers, is included into the transducer or is provided within an external box. The matching network ensures an electrical impedance close to 50 Ω at the designated working frequency (nominal frequency).

In the following forms the main information about the transducers are reported.

TRANSDUCER 1

Name:	TRASDU1
Manufacturer:	PTB
Type:	Piston-like
Model:	n.a.
S.N.:	256
Nominal frequency:	6.8611 MHz (fundamental) 6.2664 MHz (3rd harmonic)
Radius of curvature:	n.a.
Aperture/active diameter:	2.54 mm
Thru opening:	n.a.
Max. pulsed power level:	50 W (@ 6.8611 MHz)
Matching network (50 Ohm):	NO
Max. dimensions (Ø / height):	30.0 mm / 87.0 mm
Other:	Environment: submersible in water (0.05 m), 5°C t o 45°C
Connector:	BNC female on transducer

Figure 2.1. Transducer 1, PTB 256, piston-like

TRANSDUCER 2

Name:	TRASDU2
Manufacturer:	Sonic Concept
Type:	HIFU

Model:	SU-102
S.N.:	007
Nominal frequency:	3.5 MHz (fundamental)
Radius of curvature:	55.00 mm
Aperture/active diameter:	35.00 mm
Thru opening:	n.a.
Max. pulsed power level:	150 W (@ 3.5 MHz)
Matching network (50 Ohm):	Internal
Max. dimensions (weight / height):	122.0 mm / 27.0 mm
Other:	Environment: submmersible in water (0.5 m), 0°C t o 60°C Connector: BNC male on transducer

Figure 2.2. Transducer 2, Sonic concept SU-102, hifu.

TRANSDUCER 3

Name:	TRASDU3
Manufacturer:	Sonic Concept
Type:	HIFU
Model:	H-106-MRA
S.N.:	003
Nominal frequency:	2.0 MHz (fundamental) 6.38 MHz (3rd harmonic)
Radius of curvature:	63.20 mm

Aperture/active diameter:	64.0 mm
Thru opening:	n.a.
Max. pulsed power level:	400 W (@ 2.0 MHz)
Matching network (50 Ohm):	External
Max. dimensions (Ø / height):	82.0 mm / 19.0 mm
Other:	Environment: submmersible in water (0.5 m), 0°C t o 60°C

Connector: SMA male on transducer, SMA females on both ends of matching network

The matching network will function correctly only if it is connected directly to the transducer, with no added cable length.

Figure 2.3. Transducer 3, Sonic concept H-106-MRA, hifu.

2.3 ULTRASONIC FIELD CHARACTERIZATION: POWER

Knowledge of the strength of the ultrasonic fields produced in many technical applications is of increasing importance, particularly with respect to quality assurance and patient safety in the field of medical ultrasonics. The time-average ultrasonic power emitted by a transducer is one of the key values to be taken into account. Furthermore, according to both fundamental IEC standards dealing with the acoustic output of

medical ultrasonic devices, that of diagnostic devices (IEC 61157) and that of therapeutic devices (IEC 61689), the ultrasonic power is to be measured and declare.
The most common approach to total emitted power measurement, is based on radiation force balance method. When an ultrasonic beam encounter a target, the momentum transported by the wave is transferred to it.
The mass variation , for normal incidence, is proportional to the ultrasonic power emitted by the source according to the equation:

$$F = h\frac{W}{c} \qquad (1)$$

Where F is the time averaged force experienced by the target, W is the acoustic power emitted by the source transducer, c is the speed of sound in the propagation medium used and h is a proportionality factor whose value, as we will see, depends on the kind of target used and on the model adopted in order to describe the real ultrasonic field.
The international standard IEC 61161 acknowledges as the official method for determining the ultrasonic power, that based on the measurement of the radiation force by the use of a gravimetric balance.
At INRIM, the measuring system for the determination of US power based on a commercial radiation force balance (RFB System) has been developed. However, the measurements of high ultrasonic power, emitted by an HIFU transducer, are critical using conventional radiation force balances (RFBs) [223], therefore a second system based on a submergible load cell (SLC system) for ultrasonic power from 15 W to 200 W has been developed.

2.3.1 RADIATION FORCE BALANCE (RFB)

The measurement principle of the radiation force balance (RFB) is as follows: the ultrasonic beam to be measured is directed on to a target and the ultrasonic field exerts a force on the target that is connected to a gravimetric balance. The difference of the force on the target with and without ultrasound is measured from the apparent mass difference, Δm, of the target determined between the setting where no ultrasound is radiated and that where ultrasound is radiated. The force exerted by the ultrasound is so expressed as:

$$F = \Delta m \cdot g \tag{2}$$

where F is the radiation force and g is the gravity acceleration. Schematically a RFB set-up is composed by a few parts:

- a **target** that has to be perfectly absorbing or reflecting and large enough as to intercept all the ultrasonic beam;
- a **balance** for measuring the radiation force exerted on the target;
- a **connection system** to ensure that the target is correctly joint to the balance pan;
- a **water tank** in which both the transducer and the target have to be submerged so that the ultrasonic wave can propagate;
- a **support for the transducer** to hold up the transducer ensuring its right positioning and its dipping in the water tank.

THE BALANCE

The balance used is a “METTLER TOLEDO” model SAG 285. It is an electronic self compensating balance and has a resolution of 10 μg in the range 0-81 g and 100 μg in the range 81-210 g. Its sensor is covered by a rigid case and it can be remote controlled. The balance readings can be read on a digital display or can be acquired trough a software for a off line data analysis. Since the balance is really sensitive to vibrations, it has been posed on an anti-vibrating table. Furthermore the measurement system is covered by a transparent perspex box, whose aim is to insulate the system from the air turbulences which can be present in the laboratory.

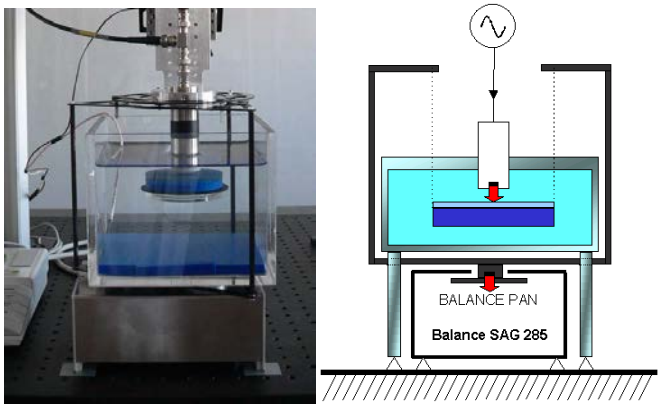

Figure 2.4. The radiation force balance realized at INRiM, with a schematic representation of the system showing the main parts of the system.

THE WATER TANK

The water tank is a transparent, perspex made, vessel which inner volume is 3.13 l. It is put onto the rigid case of the balance sensor, but it is not in contact with the balance pan. The walls of the tank can be covered by some polyurethane rubber slab in order to avoid any ultrasonic waves reflection from the border. This care is always taken any time the reflecting target is used, while can be neglected when an absorbing target is adopted.

THE TARGET SUPPORT

The target support has a twofold function. It has to connect the target to the balance pan and to keep the target suspended into the water. A rigid, carbon fibre made, structure is used. It surround the water tank and it is put in contact with the balance pan. The choice of using carbon fibre has been taken for its very suitable physical properties as it is a very rigid material, so that just a negligible portion of the radiation force is lost due to the structure elasticity, and it is at the same time very light. It is really important because the balance automatically reduces its resolution when it is solicited with higher loads. So it is important that the whole structure is as light as possible in order to have the maximum resolution available for executing the measurement. A picture of this part of the support can be seen in Fig 2.5 (a). A second part of the target support is placed onto the former and allows to dip the target into the water. Two different structures are available (Figure 2.5(b) and (c).

Figure 2.5. The target support in its three main parts. (a) The rigid structure punt on the sensitive element of the balance, (b) the target support used for absorbing target and low ultrasonic power is made of two disks connected with three very thin wires, (c) the target support used for high power measurements and with the reflecting target: the same two disks are joint together by three rigid rods.

THE TRANSDUCER SUPPORT

The transducer is held up by a support which allows its full movement. The transducer can be tilted along two axes in order to make its surface parallel to the target surface, so that orthogonal incidence is ensured. By means of two micrometric screws it is possible also to move the source transducer parallel to the target so that it could be aligned with the target axis. This is of primary importance when a reflecting target is used. Finally, the vertical movement of the target is accounted by a remote controlled stepper motor (NEWPORT ESP300) which allows a linear movement up to 10 cm with a controlled speed and with a spatial resolution of 10 nm. The motion controller allows to change the distance between the transducer and the target.

THE TARGETS

Two kinds of target (Figure 2.6) are available for the ultrasonic power measurement: an absorbing target and convex cone reflecting target.

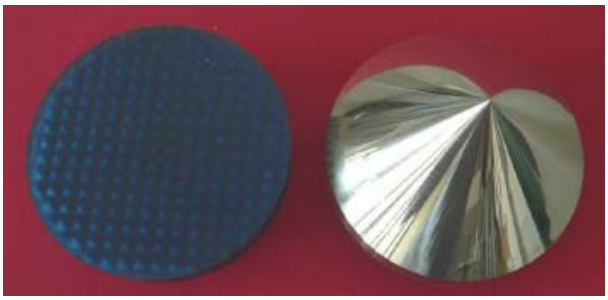

Figure 2.6. The two targets used: the polyurethane rubber absorbing target, on the left, and the conical metallic reflecting target, on the right.

The **absorbing target** is a disk, with a diameter of 8 cm, of a two layer polyurethane rubber. The target is composed of two layers with different acoustic properties. The upper one is a coupling layer, it has an acoustic impedance near to that of water and allows a good propagation of the ultrasonic radiation from the water to the absorbing layer. The second layer is the real absorber. Hollow microspheres are dispersed into the rubber so that the wave scattering is enhanced. The final result is a longer free path of the ultrasonic radiation inside the target with a significant increase in the absorption capability of the target. For ultrasonic power level higher than 1 W a **reflecting target** is used. It is a hollow convex cone with a base diameter of 8 cm and an height of 4 cm. Its lateral surface is made of a thin layer of Nickel, which is pasted over a plastic base. It is full of air in its interior, so that the very high acoustic impedance mismatch between water and metal-air interface ensure a complete reflection of the incident ultrasonic wave.

2.3.2 SUBMERSIBLE LOAD CELL (SLC)

The measurements of high ultrasonic power, emitted by an HIFU transducer, are critical using conventional radiation force balances (RFBs) [226]. At high power levels the absorbing targets are heated and pose problems of generation of drift in the signal due to thermal expansion and furthermore the target could be severely damaged. The reflecting target solves heating problems, but the rather large radiation forces and the imperfect centring may cause significant transverse components that cause unwanted movements of the target and disturbance of the force readout, and the correction factor for strong focusing fields is not yet solved.

The problems outlined above required the construction of a device with the following characteristics:

(1) Faster dynamic response, in order to be able to use shorter sinusoidal wave trains, for heating problems reduction.
(2) A solid fastening of the target to the sensing device, which is compliant only on then vertical axis and very rigid in the directions normal to this axis, as is typical of this kind of load cells.
(3) Positioning on the bottom of the tank, so that the transducer mounting is simplified; especially for HIFU it may be cumbersome providing an adaptor for mounting the transducer on the bottom of the tank.

The device chosen for this purpose is a submersible load cell (SLC), with full scale sensitivity of 50 g. The target is fastened to the SLC by means of a screw. This device fulfils requirements (1) to (3), but there are some drawbacks:

(1) The minimum measurable power is of the order of 1W, with a 1 s wave train, $U = 10\%$.
(2) The cell has to be calibrated *in situ* by standard calibrated weights to provide traceability to the mass quantity. A balance instead may be more conveniently calibrated in an accredited laboratory.

An additional advantage is that there are no effects due to surface tension, as all the measuring system is under water.

MEASUREMENT SET-UP

The device used for the ultrasonic power measurement is based on the RFB method, using a submersible load cell.

The ultrasonic power is determined from the measurement of the force exerted on a target by the field generated by an ultrasonic source. The absorbing target (diameter 150 mm) is connected to the load cell (Honeywell model 31) which measures mass variation due to the ultrasonic field when the source is alternately switched on and off. The signal produced by the load cell is conditioned by a strain gauge amplifier (Sensotec model UV-10) and then measured by a nanovoltmeter (Agilent 34420A). The load cell is screwed on the bottom of a tank with a volume of approximately 15 l. The short duration of the tone burst ($t \leq 1$ s) used for the measurement of the ultrasonic power, P_{out}, allows the use of the absorbing target even for high values ($P \leq 200$ W) of

ultrasonic power. The RMS voltage, U_{in}, of the transducer driving signal is determined, simultaneously with the mass variation, by means of a Rohde&Schwarz model URE-3 voltmeter. The electroacoustic radiation conductance G is calculated according to the relation

$$G = P_{out} U_{in}^{-2} = g \cdot u(T) \cdot \Delta M \cdot U_{in}^{-2} \qquad (3)$$

where g is the gravity acceleration evaluated in the INRiM laboratory, $u(T)$ is the speed of sound in water and ΔM is the apparent mass variation induced by the ultrasound field. In figure 2.7 the measurement apparatus is shown, with a detail of load cell and target in the upper right box.

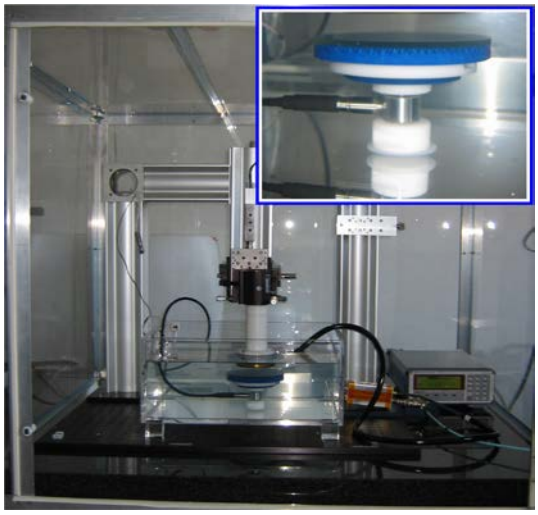

Figure 2.7. SLC measurement apparatus, with a detail of load cell and target in the upper right box.

THE TARGET

The target is rigidly connected to the sensing element of the load cell with a screw. The two parts who make the target are shown in the lower box of figure 2.8, in the upper box the assembled target is presented.

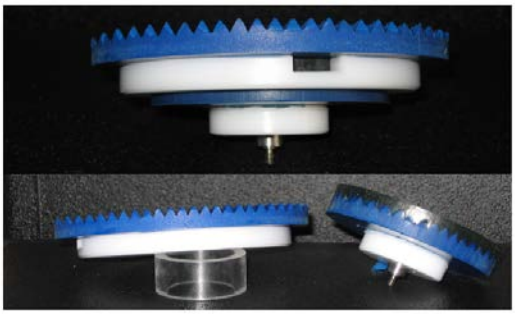

Figure 2.8. Target for SLC measurement apparatus.

The target is made of two polyurethane rubber discs and connected by means of a mechanical coupler. The lower disc is 14 mm thick and has a diameter of 80 mm, the upper one is 10 mm thick and its diameter is 120 mm. The underlying layer (blue rubber, stamped in order to form small pyramids) is the part really responsible for the ultrasonic field absorption. The upper disc is made only of blue rubber pyramids without transparent layer.

The absorbing element surface is composed of a large number of pyramids; they serve to break the ultrasonic wave front favouring the ultrasonic radiation scattering and absorption.

MEASUREMENT PROCEDURE/TECHNIQUE

In analogy with the measurement system based on a commercial balance, for the SLC system a calibration (during measurement conditions) is necessary before the ultrasound power measurements. Calibration of the cell is obtained by measuring the output voltage of the cell when charged with calibrated weights and calculating the linear regression curve relating weight and output signal [226]. This procedure allows us to calculate the force induced by the ultrasonic field, by measuring the variation of the output voltage of the cell during the insonation time. The computer program for the management and the control of the parameters influencing the measurement, such as water temperature, distance between transducer and target, power amplifier output level etc, is basically the same program used for the RFB system. The computer program controls the devices that carry out the measurement (generators, transducer movement) and acquires the values of signals sent to the transducer, of the force on the target and the values of the environmental quantities that influence the calculation of the power. The software program has been derived from the one that controls the RFB measurements.

2.4 ULTRASOUNIC FIELD CHARACTERIZATION: PRESSURE

Ultrasonic power is surely a parameter of interest in transducers characterization, but the information it gives is not complete. Some other parameters have to be measured if a fully satisfying description of the ultrasonic field produced by a transducer is desired. Moreover, the only ultrasonic output power doesn't give enough information about how likely potentially harmful physical effects are to be produced and where the ultrasound field propagates in biological tissues. For these reasons a set of parameters has been defined whose values are able to give information about the shape and the time variation of the ultrasonic beam as well as about the spatial and temporal localization of the highest acoustic pressure and intensity levels. The reference standard for these measurements is the international standard IEC 6127-1 [227]. Since from the purpose of the standard it appears that the key instrument of the whole measurement system is the hydrophone, the basic field parameter is the acoustic pressure, as it is the quantity that can be directly measured by the hydrophone. All the other parameters are calculated from the acquired pressure value.

2.4.1 HYDROPHONES

The hydrophone is the device that allows the ultrasonic pressure measurement, it can be considered as the equivalent of microphones for the ultrasonic frequencies, are tools able to generate an electrical current proportional to the acoustic pressure incident on their sensitive elements. Due to the wide range of medical applications of ultrasounds, and to the subsequent wide range of ultrasonic fields to be measured, it is not possible to have a single instrument suitable for each measurement. At INRIM laboratories, a set of hydrophones with different characteristics and different applications fields are available. Four main kinds of hydrophones are present: some needle type of different sizes and sensitivity, one membrane Hydrophone, a special HIFU addicted needle type and a Fiber Optic Probe Hydrophone (FOPH). The main properties of each hydrophone are summarized in Table 2.1.

Hydrophone		Technical characteristics				
Brand	Type	Size / mm	Sensibility / mV/MPa	Bandwith /MHz	Pressure Range /MPa	Impedance
PA	PVFD needle	0.5	400	1-20	0.05-20	50 Ω
PA	PVFD needle	1.0	800	1-20	0.05-20	50 Ω
Force	PVFD needle	0.5	250	0.5-20	0-100	50 Ω
Onda	PVFD membrane	0.5	250	0.5-45	0-100	50 Ω
Onda	PVFD needle for HIFU	0.4	70	1-10	10-500	50 Ω
Onda	PVDF needle	0.4	170	1-10	10-100	50 Ω
RP Acoustic	Fiber optic	0.1	2	1-100	-60-400	50 Ω

Table 2.1. Main characteristics of the hydrophones present at INRiM.

As can be seen from the table, the hydrophones adopted are different for kind and size, which determine different sensitivity and consequently different conditions for their use. The fiber optic hydrophone is the hydrophone mainly used in this work, for this reason in the following paragraph a more detailed description of this instrument is provided.

FIBER OPTIC PROBE HYDROPHONE (FOPH)

The fiber optic probe hydrophone is a novel instrument for the absolute measurement of short time high positive and negative pressures in liquids. The sensitive element for measuring pressure is the tip of an optical glass fiber. The pressure signal is detected by the changing light reflection at the glass fiber/water interface caused by the pressure/density influence on the refractive index of water. The most important advantages of FOPH, in comparison to piezoelectric hydrophone are the following:

- Simple and quick calibration without reference standard. Because of the self calibration the fiber optic probe hydrophone can be used as a measuring standard itself.
- High spatial resolution (100 μm)
- Bandwith 0-100 MHz

- Theoretical bandwith 0-30 GHz
- Because of the hydrophone's small diameter, a directively dependence of the sensitivity can only be noticed for frequencies higher than 1MHz
- Complete and repeteable reproduction of positive and negative pressure amplitudes.
- A damaged glass fiber tip can easily be repaired within a few minutes.
- Because of the optic principle of measurement, there is an extreme insensitiveness to electromagnetic interference.
- No aging, because neither electrical lines none piezoelectric material have contact with water.

Numerous possible application exist in the medical field, in general ultrasonic calibration and measurement as well as in the characterization of technical ultrasonic equipment, in particular using this instrument is possible to provide measurement in the focus and the extended wave field of medical instruments for ultrasound cancer therapy (HIFU) and measurement in the focus and the extended wave field of ultrasonic instrument for medical diagnosis (RM) [228].

Figure 2.9. Main device and photodetector of the Fiber Optic Probe Hydrophone FOPH 2000

OPERATION PRINCIPLE

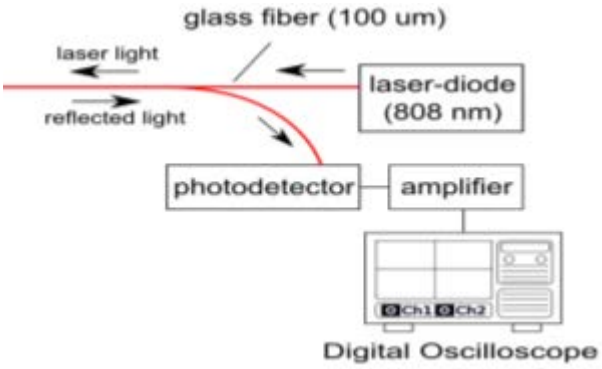

Figure 2.10. Operation principle of the Fiber Optic Probe Hydrophone

Pressure waves in liquids cause changes mass density of the medium which modulate the optical refractive index. With the Fiber Optic Probe Hydrophone the change of the refractive index can be measured by the light reflection at the tip of a glass fiber submerged in a liquid. Laser light (λ=808 nm) is coupled into the rear end of the glass fiber and is partly transmitted through and partly reflected at the fiber tip (figure 2.7). The ultrasonic field causes a variation of the refractive index, so the intensity of the reflected light is modulated. The reflected light is coupled by an optical fiber coupler to a fast semiconductor-photodetector and is converted to an electric signal which reproduces, after being amplified, the value of acoustic pressure incident on the fiber on the oscilloscope screen. With respect to the stationary light reflection signal, the simple calibration instruction allows the determination of the relation between pressure and photodiode signal. In addition to the properties set out above, optical hydrophones have important advantages compared to a conventional hydrophone: the calibration is carried out in a simple and fast way; a damaged glass fiber tip can easily be repaired, in addition to being a tool completely compatible with MRI. Due to the fact that the refractive index of a liquid depends on the pressure and temperature, the hydrophone not only can be used as pressure measuring instrument (paragraph 2.4.4), but it can also be used as temperature measuring instrument as it will be explained more in detail in paragraph 2.4.4.

Before starting a measurement, the quality of the glass fiber end surface must be checked as explained in paragraph 2.4.3.

2.4.2 SCANNING TANK SYSTEM

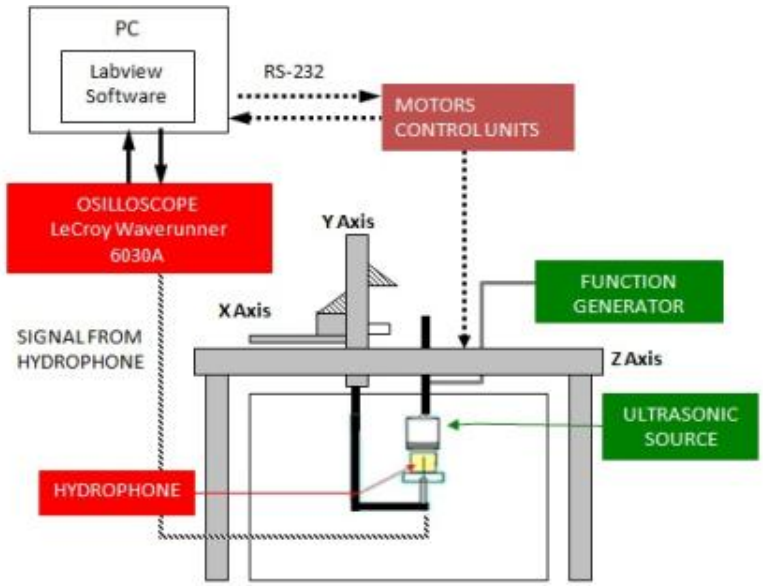

Figure 2.11. Schematic diagram of the ultrasound measurement system present at INRiM.

A typical measurement system for pressure field characterization (Fig 2.11) is composed by different parts that are described below.

HYDROPHONES

It is useful to have more than one instrument so that different hydrophones could be used for application and pressure range in which they are more suitable. If low sensitivity hydrophones are used, or if the ultrasonic pressure level to be measured is very low, it is possible to use special preamplifier to increase the electrical signal generated by the hydrophone (only for traditional needle hydrophones).

WATER TANK

It is where the measurement takes place. The tank should be large enough to allows a good movement range for the hydrophone and the possibility to perform free field measurement. As the basin walls can be sources of reflected waves, it could be useful to cover them with absorbing lining, especially when continuous waves devices are characterized.

The water tank in which the measurements take place is a Perspex (plexiglass) made

tank with 12 mm thick transparent walls. The dimensions of the basin are 1.0 x 0.5 x 0.5 m. It is usually filled with 200 l of distilled and deionised water. The water tank is connected to the MECS (Measurement Environment Conditioning System) water conditioner. This system provides microprocessor-controlled heating, degassing, UV filtration and de-ionization functions to maintain optimal water cleanliness and to allow repeatable measurements.

POSITIONING SYTSTEM

This part of the system is mainly concerned with the movement of the hydrophone within the measurement tank. A four legs frame made by aluminium is mounted around the water tank and support the motion system. This is composed by three linear motion stages for controlling the hydrophone movement along the three orthogonal axes. Each linear actuator is based on a 2.5 mm pitch ball screw that is driven by a step motor giving a positional resolution of 6.0 μm per step. As a safety precaution all drivers have two limit switches that can be used to prevent the actuator from moving beyond particular user definable positions. These switches are usually used to prevent the hydrophone from being driven into the walls of the tank, or in obstacles placed within the tank such as the transducer under measurement. Each motor is fitted with a rotary encoder that provides feedback to the drive controller about how far the drive has actually moved.

When the encoders are activated their output is feedback to the drive controller, so that, if there is a difference between the requested distance to be moved by the actuator and the real movement, the drive controller calculates the necessary correction and automatically moves the drive as appropriate. Each motion actuator has its own dedicated drive controller which deals with all aspects of motion control. In addition to supplying power to the steppers motors, they also implement the actions required by the limit or emergency stop switches, as well as administering position maintenance instructions when the system is used with drive encoders. The stepper motor drive control unit communicates with the Host PC via RS-232 interface.

TRANSDUCER HOLDER

The support for the transducer has to allow a rotation of the transducer in order to align the ultrasonic field axis with the direction of maximum sensitivity of the hydrophone. The transducer to be tested is mounted on a rigid support partially or totally immersed

in water and connected to a tilter that allows to rotate the source around two axis. This is necessary because, as will be shown in the measurement procedure description, the possibility of tilting the transducer is essential for a correct alignment of the field axis with the hydrophone

SIGNAL ACQUISITION SYSTEM

The signal acquisition system consists on a digital oscilloscope (*LeCroy Waverunner 6000A)*, to acquire the electrical signal from the output of the hydrophone and a PC for remote controlling of the position and acquisition systems and for the data analysis. The time resolution and the sampling frequency of the instrument have to be high enough to allow a good sampling of the electrical signal at the frequencies of the device to be characterised.

HOST PC AND MEASUREMENT SOFTWARE

A personal computer runs the software which is the heart of the measurement system. The PC uses a RS-232 communication card to interface with the stepper motor drive control unit, it communicates with the digital storage oscilloscope via an Ethernet (RJ45) connector ad it is able to control any other instrument (such as a function generator for generating arbitrary waveform with transducers, or a digital multimeter for temperature control) via a GPIB port. The ultrasonic measurement system (UMS) is controlled from the host PC by means of dedicated LabWIEW™ based software that controls all aspects of the operation of the system including:

- Initialization of communication interfaces via the LECroy VISA passport for communication with the DSO;
- Motion of the stepper motors actuators;
- Waveform acquisition by the oscilloscope and subsequent transfer of data to the host PC;
- Archival and post processing of acquired data.

The software has been extended and improved during thesis work, in particular, has been implemented to what concern:

- The hydrophone automatic alignment in the point in which the electrical signal at the hydrophone output is maximum. The hydrophone is automatically positioned by the software in that point;
- The run time visualization of the point that is being measured during a planar or a linear scan;
- The automatic calculation of α and β parameters in order to check the quality of the glass fiber tip when the fiber optic probe hydrophone is used;
- The waveform acquisition by the oscilloscope and the subsequent data transfer to the PC in presence of a fiber optic hydrophone;
- Pressure and temperature calculation has been implemented in the main program when a fiber optic hydrophone is used;

So by the software the operator can control any part of the measurement procedure. Trough the software it is possible to set both the direction of the scan, along one axis or over a planar surface, and the spatial resolution of the scan. Then it is possible to set some data acquisition parameters such as the number of averages to be done by the oscilloscope or to specify the hydrophone used and to load the proper calibration curve for the instruments so that the right conversion from voltage to pressure units can be done. Finally it is possible to define what acoustic parameters have to be measured by the system. During linear and planar scan the software controls the waveforms acquisition by the DSO. For each measurement point the corresponding electrical waveform acquired by the oscilloscope is stored in a proper file for post-processing elaboration.

2.4.3 MEASUREMENT PROCEDURE

MEASUREMENT SYSTEM PRAPARATION

The set-up preparation requires the water thank to be filled with distilled and degassed water. Before starting the measurement both the transducer and the hydrophone have to be immersed in water. On insertion of both the ultrasonic transducer and the hydrophone in the water, it can often happen that some air bubbles appears on the active faces of both the devices. Such bubbles are removed before the beginning of the measurement by means of a soft brush or by gentle water jet. Periodical checks are also conducted during the measurement itself in order to remove every accidental bubble

which can significantly modify the source emission or the sensitivity of the hydrophone. Finally the hydrophones used at our laboratories are recommended to be immersed in water some minutes before the measurement in order to obtain good temperature equilibrium and a full wetting of the active element surface.

1. Check of the fiber optic probe hydrophone quality

These point is done only if the measurement are conducted using a fiber optic probe hydrophone, FOPH system, if a conventional hydrophone is used to perform the measure, this point is unnecessary.

1. Select on the oscilloscope: DC, 1MΩ input. Set the bandwidth of the measurements to 2MHz. Set the photodetector ON.
2. Read the DC-photovoltage V_b on the oscilloscope when the laser is off (V_b should be in the range of 50 mV to 150 mV)
3. Switch on the laser , wait at least 5 minutes until the laser is stabilized
4. Make sure that the fiber tip is in the water
5. Set the main device in operation. Turn the mode knob in the position: MEASUREMENTS.
6. Read the data of the DC- photovoltage V_{water} on the oscilloscope. V_{water} should be in the range of 500 mV to 1000 mV.
7. Calculate the value of the DC- photovoltage $V_0 = V_W - V_B$
8. Switch the input of the oscilloscope to AC 1 MΩ.
9. Calculate the parameters α and β, which are respectively the internal light scattering factor and the quality of the glass fiber tip, by using the following formula:

$$\beta = (V_{water} - V_B)/(V_{air} - V_B) \quad (4)$$

Where: V_B: DC-photovoltage when the laser is off

V_{Water}: DC-photovoltage when the laser is on and the fiber tip is in water

V_{air}: DC-photovoltage when the laser is on and the fiber tip is in air

If β < 0.12: the glass fiber end surface is of good quality. It is possible to start with the measurement.

If β > 0.12: the glass fiber end surface is damage or dirty. The loss of stray light is too high end the signal to noise ratio is decreasing. In this case a new fiber end surface should be prepared by cleaving the fiber.

$$\alpha = \frac{1}{(V_{\mathrm{w}} - V_{\mathrm{B}})/(V_{\mathrm{oil}} - V_{\mathrm{B}}) - 1} \qquad (5)$$

Where: V_B: DC-photovoltage when the laser is off

V_{oil}: DC-photovoltage when the laser is on and the fiber tip is in the Index-adjusted liquid.

Values of α< 0.3 can be tolerated. If α is higher, it is necessary to check the fiber optic installation.

Inserting in a program, the parameters V_B, V_{Water}, V_{air} and V_{oil}, the parameters α and β are calculated automatically. If the values of α and β can be tolerated, it is possible to perform pressure or temperature measurement.

2. Alignment of the ultrasonic transducer and the hydrophone

The third step of the measurement procedures is the alignment of the transducer with the hydrophone. The goal of the step is to make the ultrasonic beam axis to coincide with the axis of the hydrophone. The method usually followed requires a recursive procedure based on the hydrophone signal maximization which brings to the alignment by subsequent refinements. The alignment procedure starts with the hydrophone at a quite long distance from the source. The transducer is then tilted until the electrical signal at the hydrophone output is maximized (a). Then the hydrophone is moved toward the source. When they are quite near the hydrophone is moved in a plane orthogonal to the direction of motion and placed in the position which maximizes its output (b). Once again the two objects are put at a long distance and the whole procedure is repeated. This process is then repeated several times, until no

remaximisation of the signal is required when moving from one distance to the other. The number of iterations required can change significantly, but it is usually reduced when the distance between the two positions is set as large as possible. Once the two instruments are well aligned the preliminary preparation is concluded and the measurement itself can begin.

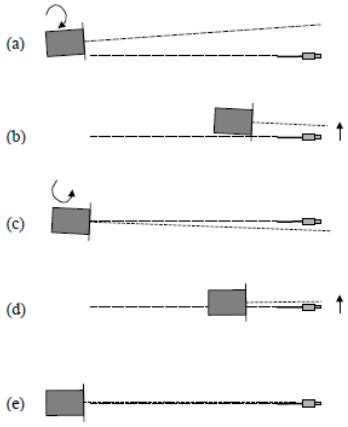

Figure 2.12. Procedure for aligning the transducer and the hydrophone.

3. Spatial scanning of the ultrasonic field.

Once the source and the receiver have been well aligned and parameters α and β can be tolerated if a fiber optic is used, the characterization itself can take place. Before starting the measurement, the hydrophone has to be set in the point of main interest (usually the point in which the acoustic waveform is maximized). Spatial scans, both linear and planar, are conducted in order to find the point of maximum electrical signal at the hydrophone output. For this purpose, the program has been realized, as described before. Checked the signal maximization, it is possible to go on with the planar scans which are needed for the ultrasonic beam characterization. A really complete description of the ultrasonic field would require a three dimensional scan with an adequate spatial resolution of the measurement point over a volume large enough to contain the entire acoustic beam generated by the source. Obviously it cannot be done in routine measurements as it would take a too long time. For this reason the real scanning procedure tries to give a good compromise between the requirements for as complete as possible information and short time consumption. Three planes are of greatest interest, it is to say the axial planes and the transversal plane where the signal acquired reaches its maximum. The size and spatial resolution of the planar scans have to be chosen taking in mind some elements. The optimal distance between adjacent measurement

points is that in which the points are at a distance equal to the hydrophone active element radius. Taking nearer points would be of little practical utility, but would increase significantly the scan duration. Once the spatial resolution of the planar scan has been set, the number of points to be measured would be determined only by the size of the area that will be scanned. This area has to be large enough to give the searched information about the beam shape, but little enough not to take a too long scan time. The aim of the planar scans are the determination of the beam area and the evaluation of the beam shape. Concerning the length of the scanning, it ideally should be long enough to put in evidence the level increase toward the focus and the intensity decrease beyond the focus.

During the scanning procedure, the hydrophone is moved at any point of the measurement array, and for each point the digital oscilloscope acquires the electrical signal from the hydrophone, or, if it has been set so, the average of a number of signals taken in the same condition, which can significantly reduce the random noise superimposed to the acoustical origin signal. Each electrical waveform is then stored as a file on the host PC.

Therefore any planar or linear scans don't give information about the pressure field if they are not processed by the software and if the electrical signals are not converted in pressure waveforms. The relationship between the acoustic pressure stimulus and the voltage response is different using a PVDF hydrophone or a fiber optic probe hydrophone. In the following paragraph the measurements procedures for the fiber optic probe hydrophone and for a PVDF hydrophone are described.

2.4.4. PRESSURE CALCULATION: FIBER OPTIC PROBE HYDROPHONE

The equation to perform sound pressure measurement with the FOPH hydrophone is the following:

$$p = \left(\left(1.453 * \frac{1 - \sqrt{0.0019867 * \left(1 + (1+\alpha) * \frac{\Delta V}{V_0} \right)}}{1 + \sqrt{0.0019867 * \left(1 + (1+\alpha) * \frac{\Delta V}{V_0} \right)}} - 1 \right) / 0.329 \right)^{7.44} * 295.6 - 295.5 [\text{MPa}] \qquad (6)$$

Where ΔV is the voltage variation, V_0 is the DC- photovoltage and α is the internal light scattering factor of the glass fiber tip.

This equation is implemented in a program. During the scanning procedure, the hydrophone is moved at any point of the measurement array, and for each point the digital oscilloscope acquires the signal from the hydrophone, or, if it has been set so, the average of a number of signals taken in the same condition. Each waveform is then stored as a file on the host PC.

The previous equation is given to the manufacturer of the hydrophone, and is based on the fact that between the pressure and the electric photodetector signal is determinate by the acoustic-optical properties of water and the DC- photodetector voltage which depends on the laser power. A change of pressure in water results in a change of density and thereby in a change of the refractive index and the reflection factor at the glass fiber/water interface. The signal of the hydrophone is the time dependent intensity of the laser light reflected at the fiber tip. The photodetector signal and the reflection coefficient are related as follows:

$$\frac{\Delta R}{R_0} = (1+\alpha)\cdot\frac{\Delta V}{V_0} \qquad (7)$$

Where: R_0: light reflection at the glass fiber/water interface;
ΔR: reflection coefficient variation;
α: internal light scattering factor of the fiber optic system
V_0: reference voltage $V_0 = V_W - V_B$;
ΔV: voltage variation;

2.4.5. PRESSURE CALCULATION: PVDF HYDROPHONE

For a PVDF hydrophone, the relationship between the acoustic pressure stimulus and the voltage response, in general, could be not simply linear, but it is frequency dependent. The voltage waveform *v(t)* from the hydrophone, acquired through the digital oscilloscope and stored in the PC, is converted in a pressure signal, *p(t)*, trough a deconvolution, using the sensitivity curve of the hydrophone $M_L(f)$ corrected for the electrical load at the hydrophone output:

$$p(t) = \frac{v(t)}{M_L(f)} \tag{8}$$

Where:

$$M_L(f) = M_C \frac{C_H}{C_H + C_C + C_A} \tag{9}$$

M_c is the end of the cable open circuit sensitivity, C_H is the corrective term accounts for the cable capacitance of the hydrophone, C_C *is* the capacitance of the right angle connection used to connect the pre-amplifier and C_A is the capacitance of the amplifier.

The frequency response of the hydrophone, $M_L(f)$, is obtained from its calibration certificate. The calibration curve for each hydrophone needs to be loaded on PC before the post processing elaboration since it is a necessary step to the right conversion. This approach has been shown to provide a more accurate voltage-to-pressure conversion process and has so been included in the IEC Hydrophone Use standards. Converting voltage signals to pressure, it is possible to obtain the results of the acoustic field spatial scans in terms of acoustic pressure. From the pressure waveforms, the peak to peak acoustic pressure and the pulse pressure integral are also calculated and stored on the PC.

The peak to peak acoustic pressure is defined as:

$$p_{pkpk} = p_c - p_i \tag{10}$$

Where $p_c = \max[p(\Delta t)]$ (11)

and $p_c = \min[p(\Delta t)]$ (12)

are respectively the maximum and the minimum value assumed by the acoustic pressure during the acquisition period.

The pulse pressure squared integral, $p_{i,}$ is defined as the time integral of the square of the instantaneous acoustic pressure in the pulse, integrated over the whole of the pulse.:

$$p_i = \int_{-\infty}^{\infty} [p(t)]^2 dt \tag{13}$$

Such an equation assumes that *p(t)* is a continuous function of the time, but in the real case what is done is digitising the signal, so that, the acoustic pressure is better represented by a function of the discrete time . For such a function the equivalent to the above integral is the sum:

$$p_i = \frac{1}{f_n}\sum_{n=0}^{N-1}\left[p(n\Delta t)\right]^2 \qquad (14)$$

where, *f,* is the sampling frequency and *N* is the number of the acquired samples.
From the pressure maps it is also possible to calculate spatial average parameters that give some information about the energy concentrated by the ultrasonic source over the whole area of interest. Many parameters can be defined just averaging the pressure parameters over all the spatial points above a requested threshold, but what is usually required by the main safety standards, is the spatial-average-temporal-average intensity (I_{SATA}). It can be calculated from the pulse pressure squared integral as:

$$I_{sata} = \frac{PRR}{\rho c}\frac{\sum \mathrm{p_i} \text{ for all points which } \mathrm{p_i} > 0.25\,\mathrm{p_i}\text{ (maximum)}}{\text{Total number of points counted}} \qquad (15)$$

Where *PRR* is the pulse repetition rate, which is the inverse of the time interval between two identical pulses, and $c\rho$ is the acoustic impedance of the propagation medium. This coefficient is due to the conversion from pressure to intensity and assumes a plane wave approximation.

2.5 ULTRASONIC FIELD CHARACTERIZATION: TEMPERATURE

Despite the fact that the HIFU are widely used in the therapeutic applications there is poor knowledge regarding the interaction of the ultrasonic beam with the tissues and the possible consequent side effects. In order to fully understand the effect of therapeutic focused ultrasound in tissue, it is necessary to measure temperature rises. While non-invasive measurement using, for example, MRgFUS

and ultrasound techniques is preferable clinically and is free from artefact of implantable devices, these cannot always provide sufficient spatial, temporal and thermal resolution and, in the case of MRgFUS, is costly and not widely available. Consequently, an alternative approach is to measure the temperature field through sensors placed in tissue simulators. With this aim, a fiber optic hydrophone and some thermocouples are used as temperature measurement instruments.

2.5.1 TEMPERATURE MEASUREMENT: FIBER OPTIC PROBE HYDROPHONE

In paragraph 2.4.4, the pressure measurement method using a FOPH is described. Due to the fact that the refractive index of water depends on pressure and temperature, it can also be used as temperature measuring instrument with high spatial and high temporal resolution. To perform temperature measurements is necessary to use the following procedure:

- Prepare the hydrophone (see paragraph 2.4.3) for the measurement and connected the fiber holder to the positioning system;
- Measure the initial water temperature T_0 with a conventional thermometer;
- Select the following setting on the oscilloscope: DC, $1M\Omega$ input. Set the photodetector in operation;
- Set the bandwith of the measurements to 2MHz;
- Read the DC-photovoltage V_b on the oscilloscope when the laser is off (V_b should be in the range of 50 mV to 150 mV);
- Swich on the laser, wait at least 5 minutes until the laser is stabilized;
- Read the data on the DC- photovoltage V_{water} on the oscilloscope;

The values V_b and V_{water} are inserted on the labwiev program, after that the measure is possible. The temperature is calculated with the relation*:*

$$T = \left(\left(\left(\left(\frac{\Delta V}{V_0}+1\right)*\left(\frac{1.72*10^{-4}*(T_0-5)^{1.64}-0{,}0146}{1+\alpha}+1\right)-1\right)*(1+\alpha)+0.0146\right)/1.72*10^{-4}\right)^{\frac{1}{1.64}}+5 \quad (16)$$

where: T: water temperature in °C;

T_0: water initial temperature °C;

V_0: DC photodetector signal at atmospheric pressure in V

ΔV : Change of the photodetector signal in V

α: internal light scattering factor of the fiber optic system.

The equation is valid in the water temperature range 5°C - 95°C.

2.5.2 TEMPERATURE MEASUREMENT: THERMOCOUPLES

Thermocouples consist of two wires of different metals connected at one end to form a junction. The principle is generally attributed to Seebeck (1821), who demonstrated that an electromotive force (e.m.f.) is generated when such a junction is placed in an environment at a temperature that is different to that at the free ends. Thermocouples are often the method of choice for temperature measurement [230-231]. They consist of two wires, generally between 12 and 50 mm in diameter, soldered or spot welded together to form a junction or multiple junctions. Apart from the practical difficulties of inserting the thin wires into tissue, the use of metal thermocouples introduces two main problems. First, the thermal conductivity of metals is between 10 and 1000 times greater than soft tissue, leading to a 'thermal conduction error'. Dickinson [231] found that this leads to averaging of the temperature over a region much larger than the junction size. This can be minimised by using small-diameter, low-thermal conductivity wire [231-232]. Second, the density of metal is between 3 and 10 times greater than that of soft tissue (e.g. copper is 8900 kgm^{-3}). Consequently, as the ultrasound wave passes, there is relative movement of the tissue and the wire. Friction from this movement results in 'viscous heating' in a thin region around the wire, and leads to an artificially high temperature measurement [233]. However, the contribution of viscous heating on measured temperature rises seems to reduce with decreasing thermocouple diameter and increasing beam width of the HIFU field [234].

For these reasons, thermocouple is not the optimal instrument for temperature measurement, often they have been used to calibrate less invasive techniques. Thermocouples used during my work are type T, exploited to characterize the fiber optic probe hydrophone and inserted in tissue mimicking phantom to evaluate temperature increase in the focus of an HIFU transducer.

For this type of termocopule, a voltage-to-temperature conversion equation, is used to reduce the data from mV to temperature. The thermocouples are calibrated at INRIM laboratories and the corresponding equation in the range 0–400°C is a 6^{th} order polynomial:

$$T = d_0 + d_1E^1 + d_2E^2 + d_3E^3 + d_4E^4 + d_5E^5 + d_6E^6$$

The constants are as follows:

$$d_1 = 2{,}592800 * 10^{-2}$$
$$d_2 = -7{,}602961 * 10^{-7}$$
$$d_3 = 4{,}637791 * 10^{-11}$$
$$d_4 = -2.165394 * 10^{-15}$$
$$d_5 = 6{,}048144 * 10^{-20}$$
$$d_6 = -7{,}293422 * 10^{-25}$$

The maximum specified error for the temperature range is no more than ±0.025°C. This is a type B uncertainty.

2.5.3 TEMPERATURE MEASUREMENT: IN SITU AT IEO

An HIFU ultrasound guided system (USgFUS) is installed at Istituto Oncologico Europero (IEO) of Milan. The USgFUS system produces and focuses high intensity ultrasounds by a single-element parabolic transducer, constituted by a PZT piezoelectric ceramic material with fixed focal length (160mm) that works at 1 MHz and can reach total power outputs between 70 and 400 W. The geometrical focal spot is about 1mm x 5 mm. However, the dimensions of the ablations induced in tissues highly depend on the intensities reached in the focus, which can be around 10 kW/cm^2, and sonication exposure times, usually around 2-4 seconds for typical treatments. The imaging transducer with frequency of 3.5/5.0 MHz is mounted at the centre of the combined treatment head to guide the localization of target tissue and to monitor the therapeutic effects in real-time. The combined treatment head is placed within a water reservoir that is filled with circulating degassed water. In figure 2.13 a photo with a schematic description of the JC- Haifu components installed at IEO is given.

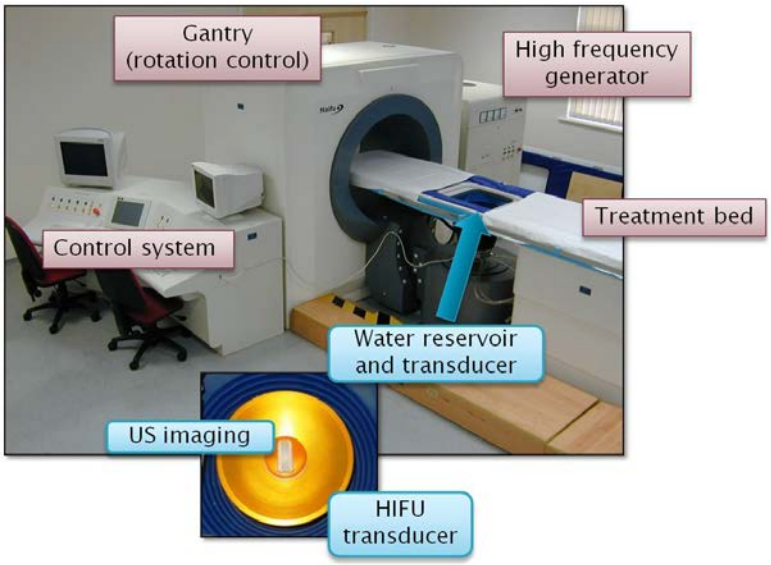

Figure 2.13. Scheme of USgFUS at IEO.

A cylindrical polyacrylamide gel phantom (60 mm radius, 40 mm height) was prepared at INRIM in order to reproduce soft tissue behaviour (1023±5 g/cm density, 1550±23 m/s sound velocity, 0.067 dB/cm attenuation coefficient) (see paragraph 2.6.2). Needle thermocouples, inserted in the phantom, were used to evaluate temperature increase (ΔT) at typical clinical settings (power outputs of 80W, 150W, 300W, 400W and sonication times of 3 s) inside the focus and at 5 mm out of it.

2.6 ULTRASONIC FIELD CHARACTERIZATION: TISSUE MIMIKING MATERIALS

The characterization of ultrasonic fields generated in water by transducers as provided by national and international standards is surely a fundamental tool for the control of device performance and for patient safety protection, but the information they give is not complete. As a matter of fact, they describe the morphology and intensity of the field, but not the effect induced by this field in real tissue. Some parameters have been defined, such as mechanical index or thermal index [229], in order to give indications about how intense these effects should be, but these parameters should be considered as

general indication and do not allow any quantitative estimation of the physical effect they refer to. As an example, it is not possible to estimate the real temperature rise generated by ultrasound exposure in tissue from the Thermal Index or the real presence of cavitation and the intensity of the effect from the Mechanical Index. A new approach is required, based on simulation of physical effects and the quantitative measure of them through in vitro measurements. HIFU dosimetry studies are usually performed on biological tissues, but this approach has two drawbacks: 1) tissues are opaque and development of coagulative lesions cannot be visually observed in real-time, and 2) the natural heterogeneous structure of tissue may complicate direct comparison with numerical models [235].Therefore, the issue is to realize new materials for simulation of acoustic properties of real tissue, new parameters which really refer to biophysical effects, and a robust methodology for measuring them. Many phantoms have been devised to mimic tissue, in particular for imaging applications [236], but the exploration of the high temperature and pressure regimes involved in HIFU exposures require a TMM with different properties. An ideal phantom for HIFU conditions has specific physical and acoustical requirements to match biological tissues. The material must have thermal properties similar to human tissues, but they also must simulate human tissues for impedance, density, acoustic absorption, non linearity parameters and thermal diffusivity. In addition to the properties listed above, for real-time visual observation of HIFU-induced lesions evolution in the phantom, a high degree of optical transparency in its pretreated state is desirable. Also, the phantom must change in a permanent, localized, and observable way in response to HIFU heating. To address these issues, in the last years, many studies has been conducted on optically transparent TMM, generally based on Agar or polyacrylamide hydrogel, in some cases with the presence of a thermally sensitive indicator protein (Bovine Serum Albumin) that becomes optically diffusive when denatured by high temperature [237]. At relatively low power (< 60 W), they have strength enough to not alterate under strong radiation stress and acoustic streaming induced by HIFU, even if, when temperatures > 60 °C are reached, melting processes or, in the case which was present, the denaturation of the protein dissolved, cause a non-reversible process thus limiting their reuse.

An ideal phantom for HIFU conditions has not been realized yet, but to develop measurement techniques, validate theoretical models, and characterize specific HIFU ablation devices, a large number of devoted tissue-mimicking materials (TMM) with specific and well-characterized physical properties, have been reported [238]. In my

PhD activity three different TMM have been realized in our laboratories: Agar-based TMM, Poliacrylamide TMM and a thermocromic silica gel. By means of these materials it has been possible to analyze the different behaviours and the heating effects caused by focused ultrasonic transducers in function of the power, frequency and irradiation time.

2.6.1 AGAR-BASED TMM

To produce the TMM based on Agarosepolymer, the liquid component (distilled water) is mixed to the dry components (Agar, 3% in weight). The solution is hated at 90 °C and then cast into a cylindrical mould. Benzalkonium chloride (0.9% in weight) or Silicon Carbide(SiC, 1% in weight) can be added to the solution while it is left to cooling, respectively to control microbial invasion, and to vary the backscatter coefficientproduce the TMM based on Agarosepolymer, the liquid component (distilled water) is mixed to the dry components (Agar, 3% in weight). The solution is hated at 90 °C and then cast into a cylindrical mould. Benzalkonium chloride (0.9% in weight) or Silicon Carbide (SiC, 1% in weight) can be added to the solution while it is left to cooling, respectively to control microbial invasion, and to vary the backscatter coefficient

Agarose-based techniques are the most widely used of the soft tissue substitute preparation techniques described in the literature. The broad use of agarose-based substitutes is a result of their well- characterized performance, the ease of fabrication (the mixture can be heated in a microwave) and the flexibility that the process provides, allowing the incorporation of additional ingredients to achieve a range of acoustic properties. Studies on this agar-based TMM showed that a limited variation of scattering ingredients during the manufacturing process resulted in TMMs with varying attenuation and backscattered proprieties [239]. Agarose is derived from agar, a hydrophilic colloid that is extracted by boiling algae. Agar-based tissue mimicking material is the only TMM that has been acoustically characterized at high frequencies (17 to 23 MHz). At these frequencies, its speed of sound was found to be independent of frequency and attenuation coefficient was found to have a linear response to frequency [240]. Interestingly, this is the only material that exhibits a linear response to attenuation with frequency of approximately $f^{1.01}$. Moreover, the acoustic property of all

TMMs varied with temperature, with the minimum variation observed in the agar-based TMM. Material properties have been reported to remain stable for as long as two and a half years under optimal storage conditions. However, in routine laboratory use without careful handling, longevity is often limited to less than one month because of microbial invasion or damage to the delicate structure.

2.6.2 POLYACRYLAMIDE TMM

The second sample used for the measurement system testing is a poliacrylamide gel similar to those described in scientific literature [241]. This gel has acoustic properties similar to biological tissue and it has been realized in our laboratory through a solution of 100ml of distilled water, 10g of acrylamideand 526mg of N, Nbisacrilamide, 1mlof a solution 10% in weight of ammonium persulfateand 0.5 ml of N, Ntetramethylethylenediamine (TEMED) which initiates polymerisation. The sample is prepared by the mixing of all the components except the TEMED. The liquid solution prepared is poured in the plexiglass made cylindrical stamp of height equal to4.5cm and a diameter of 5 cm. Than the TEMED is added so starting the geling process. This concentration allows the polyacrilamide gel to be very clear and transparent, because the normally exothermic polymerization reaction does not release enough heat to denature the embedded proteins. The use of a transparent material that mimics tissue response to HIFU exposure would facilitate dosimetry studies, transducer evaluation, and the development of theoretical and numerical models of HIFU treatments. A transparent phantom would indeed permit reducing the number of experiments to accomplish any of the goals listed above, compared to the procedure required for doing the same on biological tissues[242].

2.6.3 THERMOCROMIC SILICA GEL

The third sample is an innovative tissue simulator containing thermosensitive chemical component . By mean of this material it has been possible to "visualize" the effect of heating induced by HIFU transducers. The material was a silica based hydrogel containing cobalt chloride salt. Aqueous solutions of cobalt chloride are pink colored, such color is due to the formation of the ion $[Co(H_2O)_6]^{2+}$, while when the salt is

dissolved in Propanol, a deep blue solution is obtained, that is due to the formation of $[CoCl_4]^{2-}$ ion. As reported in [243], with an opportune ratio, between water and chloride anion, is possible to obtain a thermochromic silica gel because when temperature increase/decrease a desorption/adsorption of water occurs, thus the change from pink-red to violet-deep blue is observed. In order to obtain a thermochromic gel that had a transition temperature in the interval of interest, the samples were prepared following the composition reported in [243], expressed in terms of molar ratio: 1 of tetrametilorthosilicate ; 8.4 of 1-Propoanol; 6.6 of water and 0.1 of CoCl2. The solution was stirred for 30 min up to complete homogenization to accomplish the hydrolysis and to favor partial policondensation reaction, afterwards, it has been casted in a square cuvette in order to record the colour variation with good resolution, using a digital camera.

Thermochromic materials have already been proposed in the past for investigate the heating effect caused by no-focused ultrasounds, using film of liquid crystal [244]; however the lack of adsorption of the film have limited its investigating properties; recently a standard acoustic absorber containing a thermochromic pigment was employed to study the heating effect of ultrasonic device commonly used in physiotherapy, but the transition temperature is quite low (< 50°C) and when it was subjected to longer exposure time, a non linearity into the temperature propagation and "blurring effects" have been observed. Thermochromic gel is also an emerging research field, because of the interest into sensoring and smart materials applications. Different preparations of thermochromic gels has been reported during last five years [245], but in most of these cases they can be used as two dimension materials and do not have sufficient rigidity to be casted in three dimension TMM; newly, preparation of a reversible thermochromic gel based on silica hydrogel with a temperature transition in the range of 30-70 °C in function of the molar ratio of the chemical precursors, has been reported [243].

The thermochromic gel proposed represents a smart and cheap tool for an immediate characterization of focused ultrasonic fields and evaluation of temperature rise induced by HIFU transducers. Using different transducers, operating at different frequencies and with different shape of the emitter, it has been possible verify how the effects of temperature rise are not exclusively correlated with the power used, but rather influenced by the frequency and the geometry of the focused acoustic field and thus from the interaction of the beam with the gel.

MEASUREMENT SYSTEM FOT THERMOCROMIC SILICA GEL

The heating effects in a thermochromic silica gel have been evaluated using a type T thermocouple inserted in the sample. The thermocouple is positioned in the point of maximum temperature, which is supposed to be the focus region of the ultrasound beam, or in the pre-focus region, in order to evaluate the temperature in the external lines. For these experiments, two HIFU transducers are used: a single-element concave transducer MR-106, (transducer 3) with a working frequency of 2 MHz, diameter of 64 mm and focus at 51.7 mm, (it can also work at its third harmonic, f = 6.3 MHz), and a single-element concave transducer SU-102, with a working frequency of 3 MHz, diameter of 35 mm and focus at 51.8 mm (transducer 2).The ultrasound source is powered by a wave function generator Agilent 33250A through an amplifier (AR 500A100A).The power used for these experiment was in the range of 20-100W.The transducers and the thermochromic TMM are immersed in deionised water. The voltage signal, acquired by the thermocouple, is visualized by a nanovoltmeter (Agilent 34420) and a custom-made LabWIEV program collects and plots the signal (see figure 2.14).

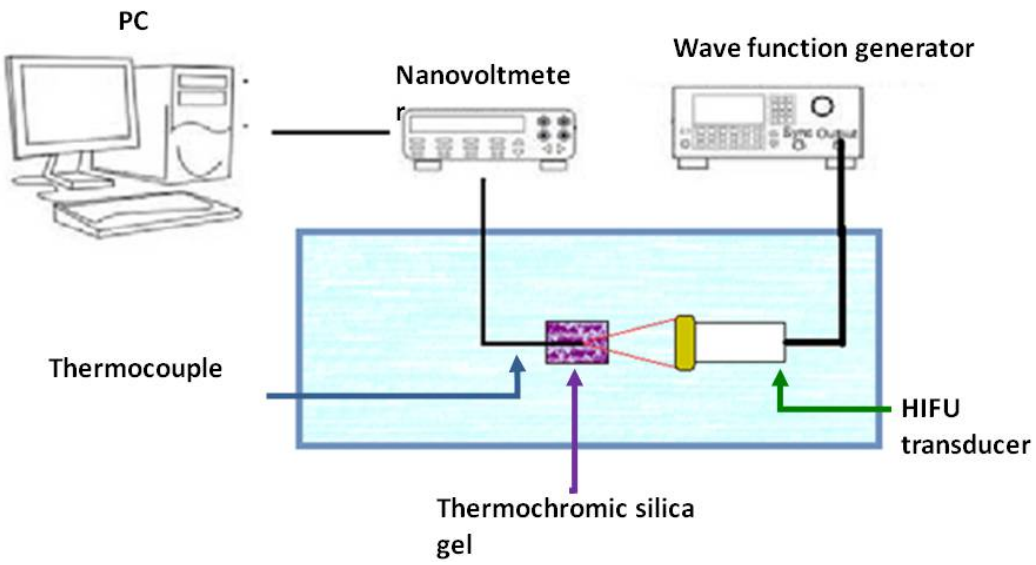

Figure 2.14. Scheme of experimental apparatus

2.7 OXYGEN LOAD NANOBUBBLES

Oxygen nanocarriers have been developed at INRIM to treat a variety of hypoxia-related diseases and in particular hypoxic cancerous tissues. This is an innovative, effective, almost non-invasive and low-cost nano-technological device. Different formulations of oxygen-loaded nanobubbles (OLNs) were realized to improve the available nanotechnology of gas delivery by studying new core/shell nanocarriers. OLNs could result effective in oxygen release, without losing the favorable properties of the nanobubbles explained in chapter 1 (e.g. nanometer size range, stability, sensitivity to ultrasounds, lack of toxicity, low manufacturing costs) and could be prepared in formulations suitable for topical treatment of dermal tissues. The main feature of these new nanocarriers consisted of employing 2H,3H-decafluoropentane (DFP) or Perfluoropentane (PFP) for the oxygen-storing core structure. Notably, DFP displays oxygen-solubilizing capabilities as high as OLNB core-associated PFP [246]. However, unlike PFP, which has a boiling point of 32 ºC and is gaseous at body temperature, DFP is a clear, colorless fluorocarbon with a boiling point of 51ºC, thus resulting liquid at 37°C. For that reason, the new nanocarriers were named oxygen-loaded nanodroplets (OLNDs). Dextran was kept as the main constituent of the polysaccharidic shell as for former OLNs, since dextran-based formulations have been extensively tested for biocompatibility, and dextran-based hydrogels are currently used as matrices in tissue engineering, without showing signs of inflammation *in vivo*. Recent toxicological studies on mechanically processed polysaccharides of different molecular weight showed that dextran, along with the products of its mechano-chemical processing, can be classified as class 4 (low-toxicity) substance. On the other hand, chitosan was also chosen to build the polysaccharidic shell of OLNDs. This polysaccharide is a positively charged, partially deacetylated form of chitin, a natural substance found abundantly in the exoskeletons of insects and the shells of crustaceans. The repeating units of chitosan are β(1-4)-linked glucosamines, thus it contains a large number of hydroxyl- and amino-groups providing several possibilities for derivatization or grafting of desirable bioactive groups. Chitosan also displays high biocompatibility, healing capabilities, anti-cancer activity and anti-microbial properties against some

bacteria (e.g. methicillin-resistant *Staphylococcus aureus*) and fungi (e.g. *Candida albicans*). Due to these characteristics, it has been investigated for use in several biomedical applications, including wound dressings and drug carriers.

Along with OLNDs, complementary control preparations were also evaluated, including OLNBs, oxygen-free nanodroplets (OFNDs), oxygen-free nanobubbles (OFNBs), and oxygen-saturated solution (OSS). All preparations were made either in liquid (water) or gel (hydroxyethylcellulose, HEC) formulations. For selected experiments with cell cultures, two additional OLND phosphate-buffered saline (PBS) formulations were also prepared by using dextran or fluorescein isothiocyanate (FITC)-conjugated dextran, respectively (see figure 2.16). Furthermore, 346 nm UV exposure for 20 min was chosen as a sterilizing procedure, which proved to be effective in a long-term manner without inducing O_3 or significant singlet oxygen generation.

2.7.1 OVERVIEW OF OLNs EXPERIMENTS

Immediately after manufacturing, OLND and control preparations were characterized for: morphology, by optical and transmitting electron microscopy (TEM); average diameters, particle size distribution, polydispersity index and zeta potential, by dynamic light scattering; and oxygen content (before and after UV sterilization), through a chemical assay.

Note that since the zeta potential measures charge repulsion or attraction between particles, it is a fundamental parameter to determine nanoparticle physical stability, with zeta potentials lower than -30 mV or larger than +30 mV being generally required for physical stability of colloid systems [250]. Although nanodroplets and nanobubbles displayed zeta potentials slightly larger than -30 mV, our formulations proved to be physically stable over time for the steric repulsion of the polymer chains, as assessed by monitoring their sizes and zeta potential by dynamic light scattering for 72 h after manufacturing. In addition, nanoparticle charge makes them suitable for topical treatment, enhancing their interaction with skin and improving their therapeutic effect on inflamed cutaneous tissues, either without or with concomitant US treatment.

OLND toxicity on human cells was evaluated by testing in vitro cultures of human HaCaT keratinocytes, a cell line immortalized from a 62-year old Caucasian male donor.

As a next step, OLND abilities to release oxygen in vitro were comparatively evaluated. Following dissolution of the same amount of nanocarrier-containing gel (2% HEC) in a hypoxic solution, OLNDs released larger amounts of oxygen for longer times (up to 6 h) than OLNBs and OSS. Oxygen release was compared also following sonication. In fact US is expected to impact on oxygen release kinetics through several mechanisms. Firstly, US can induce bubble formation after acoustic droplet vaporization. Under particular gas content and bubble radius conditions, bubble oscillations might lead to a more violent release mechanism due to cavitation, that is the formation, growth, and implosive collapse of bubbles in a liquid (see paragraph 1.2.3).

Finally, US might elicit sonophoresis, temporarily enhancing skin leakage thus favoring transdermal drug release (see paragraph 1.5.4). To monitor the effect of US on the ability of OLNDs to trespass the dermal layer, a home-made apparatus consisting of two sealed cylindrical chambers separated by a layer of pig ear skin was employed. One chamber (the oxygen-donor), containing OLNDs or control solutions, was connected to an US-transducer, with the beam directed towards the membrane; the other chamber (the oxygen-recipient) was filled with hypoxic solution and monitored by an oxymeter. The US transducer (f = 2.5 MHz; P = 5 W) was alternatively switched on and off at regular time intervals of 5 min for an overall observational period of 135 min, and oxygen concentration was monitored in the recipient chamber every 45 min.

Once proven in vitro that OLNDs were more effective than former OLNBs and OSS in releasing oxygen, without being toxic on human keratinocytes, and that gel formulation appeared suitable for treatment of skin membranes, OLND gel formulation was tested for oxygen delivery in vivo. To test OLND effects on tissue oxygenation without US treatment, the shaved hindlimbs of nine anaesthetized mice were topically treated with OLND, OFND or OSS gel formulations. Before, during and after treatment (10 min), the subcutaneous levels of oxy- and *deoxy-Hb* were monitored by photoacoustic imaging. Such innovative hybrid technique, which can image both light absorption properties and acoustic transmission properties of an object in a two-dimensional slice using a computed tomography photoacoustic imager [251], is applicable to the quantification of tissue chromophores such as *oxy-Hb* and de*oxy-Hb* for the measurement of physiological parameters such as blood oxygen saturation and total Hb

concentration [252]. OLNDs were finally tested in vivo. The skin oxygenation of the shaved hind limbs of nine anaesthetized mice topically treated with OLND, OFND or OSS gel formulations was monitored by visualizing the subcutaneous levels of *oxy-Hb* and *deoxy-Hb* through photoacoustic imaging before, during and after the treatment (10 min). This innovative hybrid imaging technique, based on the light absorption and the acoustic transmission properties of a tissue slice interrogated by a computed tomography photoacoustic imager, can quantify the density of tissue chromophores such as *oxy-Hb* and *deoxy-Hb* and measure some physiological parameters such as blood oxygen saturation and total Hb concentration.

Lastly, the OLND ability to improve tissue oxygenation in vivo after US treatment was investigated. The shaved abdomens of five anaesthetized mice were topically treated with OLNDs and sonicated for 30 sec (f = 1 MHz). Skin oxygenation was investigated through transcutaneous oxymetry before and after the treatment. This technique measures the oxygen transcutaneous tension *($tcpO_2$)* through a non-invasive method which elicits a heating-related vasodilatation, generating fast diffusion of gases from the vessels to an electrode located on the skin. When capillary *oxy-Hb* dissociation occurs, the reaction of oxygen reduction generates a current which is directly proportional to capillary oxygen arterial pressure. Monitoring $tcpO_2$ is a well-consolidated technique extensively used also in clinical practice. Basal $tcpO_2$ values in mice were inhomogeneous, possibly as a consequence of the different level of peripheral vasoconstriction induced by anesthesia. Nevertheless, after topical administration of US-activated OLNDs, hypoxic mice displayed larger oxygenation levels in a time-sustained manner (up to 1 h). A graphic to summarise all the experiments performed with OLNs is given in figure 2.15.

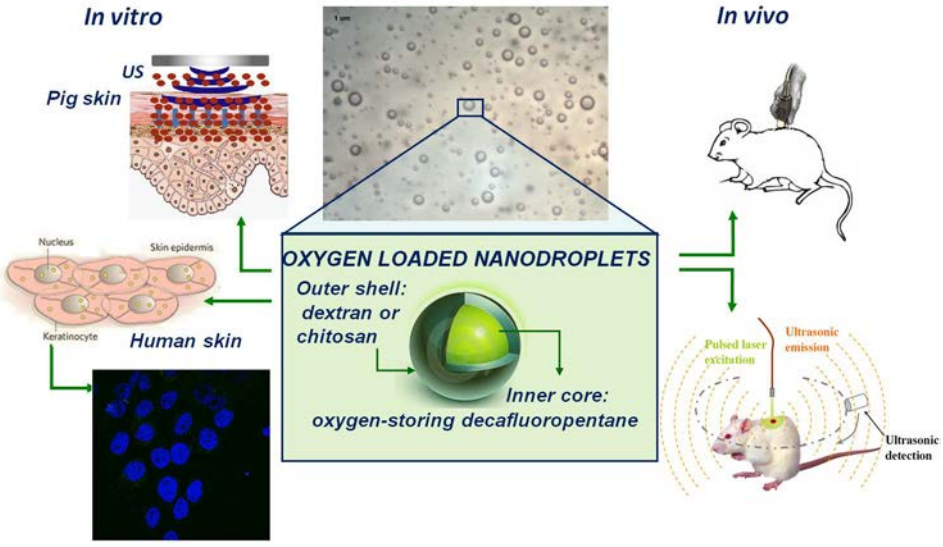

Figure 2.15. Overview of the experiments performed with OLNs

2.7.2 DEXTRAN AND CHITOSAN OLNs: MATERIALS

Unless otherwise stated, all materials were from Sigma-Aldrich (St Louis, MO). Ethanol (96%) was obtained from Carlo Erba (Milan, Italy); Epikuron 200® (soya phosphatidylcholine 95%) was kindly gifted by Degussa (Hamburg, Germany); palmitic acid, decafluoropentane (DFP), perfluoropentane (PFP), dextran sodium salt (MW = 100.000), chitosan (medium MW) and polyvinylpyrrolidone (PVP) were from Fluka (Buchs, Switzerland); ultrapure water was obtained using a 1-800 Millipore system (Molsheim, France); Ultra-Turrax SG215 homogenizer was from IKA (Staufen, Germany); Delsa Nano C analyzer was from Beckman Coulter (Brea, CA); Philips CM10 instrument was from Philips (Eindoven, The Netherlands); XDS-3FL microscope was from Optika (Ponteranica, Italy); cell culture RPMI 1640 medium was from Invitrogen, (Carlsbad, CA); cell culture Panserin 601 medium was from PAN Biotech (Aidenbach, Germany); PEN-STREP was from Cambrex Bio Science (Vervies, Belgium); LSM710 inverted confocal laser scanning microscope was from Carl Zeiss (Oberkochen, Germany); Synergy HT microplate reader was from Bio-Tek Instruments (Winooski, VT); Zoletil 100 was from Virbac (Carros Cedex, France); Rompun was from Bayer (Leverkusen, Germany); Vevo® LAZR system for photoacoustic imaging was from Fujifilm Visualsonics (Amsterdam, the Netherlands); TINA TCM30 oxymeter was from Radiometer (Copenhagen, Denmark). HaCaT cells were kindly provided by

Dr. F. Silvagno, Dep. of Oncology, University of Torino. BALB/c mice were bred under specific pathogen-free conditions by Fujifilm Visualsonics (Amsterdam, The Netherlands) or at the Molecular Biotechnology Center (Torino, Italy).

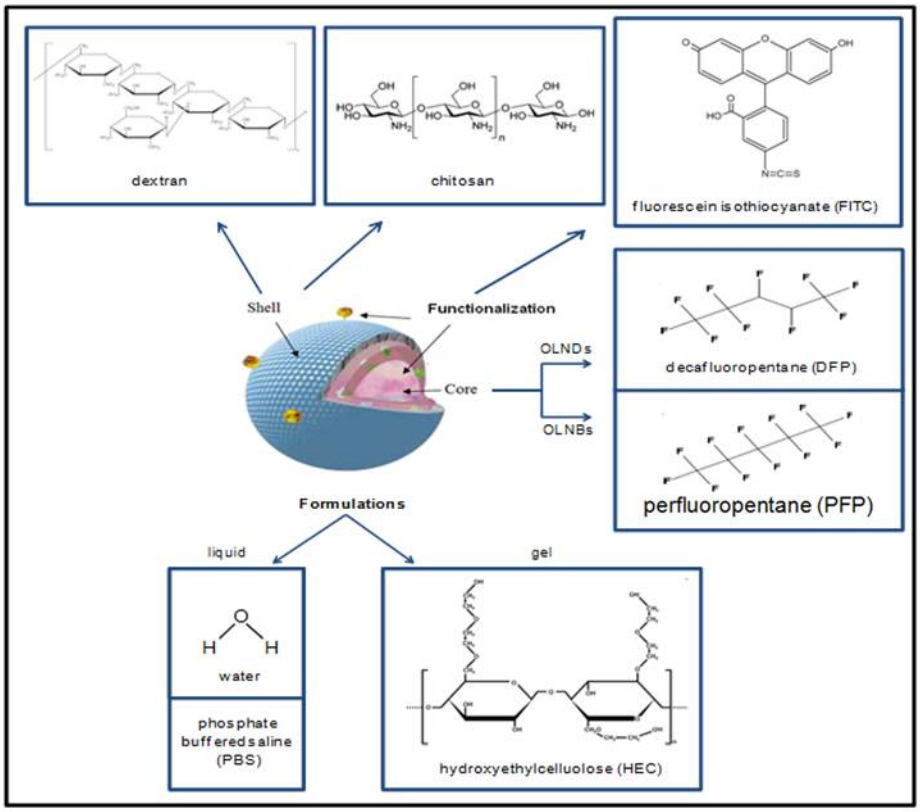

Figure 2.16. Schematic structure of OLND and OLNB liquid/gel formulations.

2.7.3 DEXTRAN AND CHITOSAN OLNS: PREPARATIONS

PREPARATION OF LIQUID FORMULATIONS

Compositions of all formulations are detailed in Tables 3.15 and 3.17. For oxygen-loaded nanodroplet (OLND) liquid formulations, 1.5 ml DFP along with 0.5 ml PVP and 1,8 ml Epikuron® 200 solved in 1% w/v ethanol and 0.3 % w/v palmitic acid solution were homogenized in 30 ml water (preparation A) or phosphate buffered saline (PBS) (preparations C-D) for 2 min at 24000 rpm by using Ultra-Turrax SG215 homogenizer. Thereafter, the solution was saturated with O_2 for 2 min. Finally, 1.5 ml dextran sulfate (preparations A, C) or fluorescein isothiocyanate (FITC)-labeled dextran sulfate (preparation D) solution was added drop-wise whilst the mixture was

homogenized at 13000 rpm for 2 min. For OLNs prepared with chitorsan as core, a 2.7% w/v chitosan solution (pH 5.0) was added drop-wise whilst the mixture was homogenized at 13000 rpm for 2 minutes. For oxygen-loaded nanobubble (OLNB) water formulation, the protocol developed by Cavalli and colleagues [180] was applied by using PFP as a core fluorocarbon. Oxygen-free nanodroplet (OLND) and nanobubble (OFNB) water formulations were prepared according to OLND and OLNB protocols without adding O_2. For oxygen-saturated solution (OSS) water formulation, OLND preparation protocol was applied omitting dextran sulfate and DFP addition. For more details, see Table 3.14 and 3.16.

PREPARATION OF GEL FORMULATIONS

To obtain gel formulations, 0.8 mg hydroxyethylcellulose were solved in 20 ml water, and subsequently mixed 1:1 with OLND, OFND, OLNB, OFNB, or OSS water formulations.

STERILIZATION

OLNDs, OFNDs, OLNBs, OFNBs, and OSS were sterilized through 346 nm UV exposure for 20 min. Thereafter, UV-treated materials were incubated with cell culture RPMI 1640 medium in a humidified CO_2/air-incubator at 37°C up to 72 h, not displaying any signs of microbial contamination when checked by optical microscopy. Moreover, UV-sterilized O_2-containing solutions underwent further analyses through O_3 measurement and electron paramagnetic resonance (EPR) spectroscopy, showing no O_3 generation and neglectable singlet oxygen levels immediately after UV exposure.

2.7.4 DEXTRAN AND CHITOSAN OLNS: PHYSICAL-CHEMICAL CHARACTERIZATION

MORPHOLOGY

The morphology of OND and ONB formulations was determined by transmitting electron microscopy (TEM) and by optical microscopy. TEM analysis was carried out using a Philips CM10 instrument, whereas optical microscopy was carried out using using a XDS-3FL microscope. ND and NB formulations were dropped onto a Formwar-coated copper grid and air-dried before observation.

SIZE, PARTICLE SIZE DISTRIBUTION AND ZETA POTENTIAL

Average diameters, polydispersity indexes, and zeta potentials of OLNDs and OLNBs were determined by dynamic light scattering using Delsa Nano C instrument, displaying a (0.6 nm - 7μm) range for measurements of particle size distribution. Each value reported is the average of three measurements of ten different formulations. The polydispersity index indicates the size distribution within a OLND or OLNB population. For zeta potential determination, formulation samples were placed into an electrophoretic cell, where an electric field of approximately 30 V/cm was applied. Each sample was analyzed at least in triplicate. The electrophoretic mobility was converted into zeta potential using the Smoluchowski equation [250].

OXYGEN CONTENT

Oxygen content of OLNDs, OLNBs and OSS was evaluated by adding known amounts of sodium sulfite and measuring generated sodium sulfate, according to the reaction:

$Na_2SO_3 + ½\ O_2 \longrightarrow Na_2SO_4$

STABILITY

The stability of formulations stored at 4°C, 25°C or 37°C was evaluated over time up to 72 h by determining morphology, sizes and zeta potential of OLNDs and OLNBs by optical microscopy and light scattering.

2.7.5 DEXTRAN AND CHITOSAN OLNs: BIOCOMPATIBILITY ASSESSMENT

HUMAN KERATINOCYTE CELL CULTURES

HaCaT, a long-term cell line of human keratinocytes immortalized from a 62-year old Caucasian male donor,[33] was used for assessment of OLND biocompatibility. Cells were grown as adherent monolayers in Dulbecco's modified Eagle's medium (DMEM) supplemented with 10% foetal bovine serum (FBS), 100 U/ml penicillin, 100 μg/ml streptomycin (PEN-STREP) and 2 mM L-glutamine in a humidified

CO_2/air-incubator at 37°C. Before starting the experiments, cells were washed with PBS, detached with trypsin/ethylenediaminetetraacetic acid (EDTA) (0.05/0.02% v/v), washed with fresh medium and plated at a standard density (10^6 cells/well in 6-well plates) in 2 ml FBS-free Panserin 601 medium to prevent serum interference in the toxicity assay.

Evaluation of OLND uptake by human keratinocytes

HaCaT cells were plated in 24-well plates on glass coverslips and incubated in Panserin 601 medium for 24 h with/without 200 µl FITC-labeled OLNDs in a humidified CO_2/air-incubator at 37°C. After 4',6-diamidino-2-phenylindole (DAPI) staining to visualize cells nuclei, fluorescence images were acquired by a LSM710 inverted confocal laser scanning microscope equipped with a Plan-Neofluar 63×1.4 oil objective, that allowed a field view of at least 5 cells. Wavelength of 488 nm was used to detect OLNDs, and of 460 nm to detect the labeled nuclei. The acquisition time was 400 ms.

OLND CYTOTOXICITY

The potential cytotoxic effects of OLNDs were measured as the release of lactate dehydrogenase (LDH) from HaCaT cells into the extracellular medium. Briefly, cells were incubated in Panserin 601 medium for 24 h in the presence or absence of increasing doses (100-400 µl) of OLNDs, either in normoxic (20% O_2) or hypoxic (1% O_2) conditions, in a humidified CO_2/air-incubator at 37°C. Then, 1 ml of cell supernatants was collected and centrifuged at 13000g for 2 min. Cells were washed with fresh medium, detached with trypsin/ EDTA (0.05/0.02% v/v), washed with PBS, resuspended in 1 ml of TRAP (82.3 mM triethanolamine, pH 7.6), and sonicated on ice with a 10 s burst. 5 µl of cell lysates and 50 µl of cell supernatants were diluted with TRAP and supplemented with 0.5 mM sodium pyruvate and 0.25 mM NADH (300 µL as a final volume) to start the reaction. The reaction was followed measuring the absorbance at 340 nm (37 °C) with Synergy HT microplate reader. Both intracellular and extracellular enzyme activities were expressed as µmol of oxidized NADH/min/well. Finally, cytotoxicity was calculated as the net ratio between extracellular and total (intracellular + extracellular) LDH activities.

HUMAN KERATINOCYTE CELL VIABILITY

Cell viability was evaluated using 3-(4,5-dimethylthiazol-2-yl)-2,5-diphenyltetrazolium bromide (MTT) assay. HaCaT cells were incubated in Panserin 601 medium for 24 h with/without increasing doses (100-400 µl) of OLNDs, either in normoxic (20% O_2) or hypoxic (1% O_2) conditions, in a humidified CO_2/air-incubator at 37°C. Thereafter, 20 µL of 5 mg/mL MTT in PBS were added to cells for 3 additional hours at 37 °C. The plates were then centrifuged, the supernatants discarded and the dark blue formazan crystals dissolved using 100 µL of lysis buffer containing 20% (w/v) sodium dodecyl sulfate (SDS), 40% N,N-dimethylformamide (pH 4.7 in 80% acetic acid). The plates were then read on Synergy HT microplate reader at a test wavelength of 550 nm and at a reference wavelength of 650 nm.

2.7.6 DEXTRAN AND CHITOSAN OLNS: *IN VITRO* EXPERIMENTS

OXYGEN RELEASE WITHOUT US

The concentration of oxygen released by diffusion from OLND, OLNB and OSS liquid or gel formulations into a hypoxic solution was monitored up to 6 h through Hach Langhe LDO oxymeter, displaying an accuracy of 0.01 mg/l. Before each measurement, the oxymeter was calibrated in air, waiting for stable temperature and humidity conditions to be reached.

OXYGEN RELEASE WITH US AND TRESPASSING OF SKIN MEMBRANES

To study the ability of US-activated OLNs to release O_2 through biological membranes, a US probe with a high frequency transducer (f = 2.5 MHz; P = 5 W) was used, combined with a home-made apparatus with two sealed cylindrical chambers (lower chamber: OLND, OFND, OLNB, OFNB or OSS solutions; upper chamber: hypoxic solution) separated by a layer of pig ear skin employed as a model of biological membrane (see Figure S7 for details). US treatment was performed for 5 min; thereafter, O_2 concentration in the hypoxic chamber was monitored up to 135 min every 5 min by Hach Langhe LDO oxymeter (accuracy: 0.01 mg/l). Because of the local heating caused by US, the O_2 sensor was positioned laterally in order to

prevent possible damage of the oxymeter, whereas the transducer was held in a fixed position, within the donor compartment (see figure 2.17). The acoustic power of the transducer was determined through a balance's radiation force with a reflecting target, with an uncertainty of 4%.

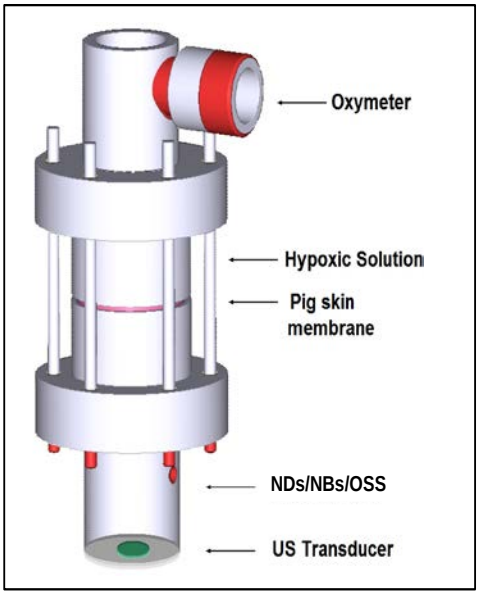

Figure 2.17. Home-made apparatus measuring O_2 release across a natural membrane after OLN sonication.

2.7.7 DEXTRAN AND CHITOSAN OLNS: *IN VIVO* EXPERIMENTS

MICE

Before performing the experiments, healthy BALB/c mice were shaved locally (abdomens or hindlimbs depending on the study, as described in the following paragraphs) and anaesthetized by injecting intramuscularly a mixture of tiletamine/zolazepam 20 mg/Kg (Zoletil 100) and 5 mg/Kg xylazine (Rompun). All procedures were done in accordance with the EU guidelines and with the approval of the Università di Torino animal care committee.

PHOTOACOUSTIC IMAGING

The shaved hindlimbs of nine anaesthetized mice were topically treated with OLND, OFND or OSS gel formulations. Before, during and after treatment (10 min), the subcutaneous levels of oxy- and de-oxy-hemoglobin were monitored by photoacoustic imaging, which was performed with Vevo® LAZR system featuring a hybrid ultrasound transducer (central frequency: 21 MHz; spatial resolution: 75 μm).

MEASUREMENT OF $TcpO_2$ WITH US

The shaved abdomens of five anaesthetized mice were topically treated with OLNDs and ultrasonicated for 30 sec using a home-made ultrasound (US) equipment (frequency: 1 MHz). Before and after treatment (1 h), the transcutaneous tension of oxygen ($tcpO_2$) was measured through TINA TCM30 oxymeter. The TINA TCM30 oxymeter provides the measure the oxygen partial pressure of the transcutaneous capillary blood ($tcPO_2$). All $tcpO_2$ measurements were taken after physiological stabilization.

CHAPTER 3

RESULTS

3.1 ULTRASONIC FIELD CHARACTERIZATION: POWER

The first step for transducer's characterization is the measurement of the total, time-averaged ultrasonic output power, P_{out}, emitted by transducers, described in paragraph 2.2, is measured. The acoustic power values were obtained with the system based on radiation force balance method using, in these cases, a submersible load cell (SLC). A detailed description of the system has been provided in paragraph 2.3.1.

A continuous-wave, sinusoidal excitation voltage has been applied to the transducer (including the impedance matching network) and measured. There are five voltage levels, namely "low", "medium", "high", "very high" and "ultra high". The specified RMS voltage values, U_s, and the specified frequency values, f_s, are given in Table 3.1.

N	Transducer Type	f_s / MHz	*Level* / W	U_S / V_{rms}
1	TRANSDUCER 1 PTB 256	1.8611	10 (low)	42.00
3			20 (medium)	60.0
4		6.2664	10 (low)	41.0
6			20 (medium)	58.0
1	TRANSDUCER 2 Sonic Concept SU-102	3.5	20 (medium)	33.0
3			50 (high)	53.0
4			75 (very high)	61.0
5			100 (ultra high)	70.0
1	TRANSDUCER 3 Sonic Concept H-106-MR	2.0	20 (medium)	41.0
3			50 (high)	62.0
4			75 (very high)	78.0
5			100 (ultra high)	90.0
6		6.38	10 (low)	29.0
7			20 (medium)	40.0
8			50 (high)	61.0
9			75 (very high)	76.0

Table 3.1 RMS voltage values, U_s, and the frequency values, f_s, for five voltage levels.

The electro-acoustic radiation conductance *G* must be calculated according to

$$G = \frac{P_{out}}{U_{in}^2} \tag{1}$$

G is expressed in Siemens, S, or decimal submultiples of this unit. The input voltage U_{in} refers to the transducer input and is to be measured at a point as near as possible to the transducer input connector.

For each transducer, power level and for each frequency, the final measured value of ultrasonic conductance is reported in tables 3.2, 3.3 and 3.4. The *G* values are calculated as the mean of the four measures, realized for each measurement condition. The highest

uncertainty among the four obtained for each conductance for each fixed power level and frequency is taken as the uncertainty for the mean value.

TRANSDUCER 1

N	f_S / MHz	P / W	G / mS	U_{in} / V	$U(G)$ / %
1	1.8611	10	5.50	43.61	8.90
2	1.8611	20	5.53	62.17	8.43
3	6.2664	10	6.00	41.01	8.91
4	6.2664	20	5.91	58.44	8.45

Table 3.2. Power level, frequency input voltage and ultrasonic conductance related to transducer 1.

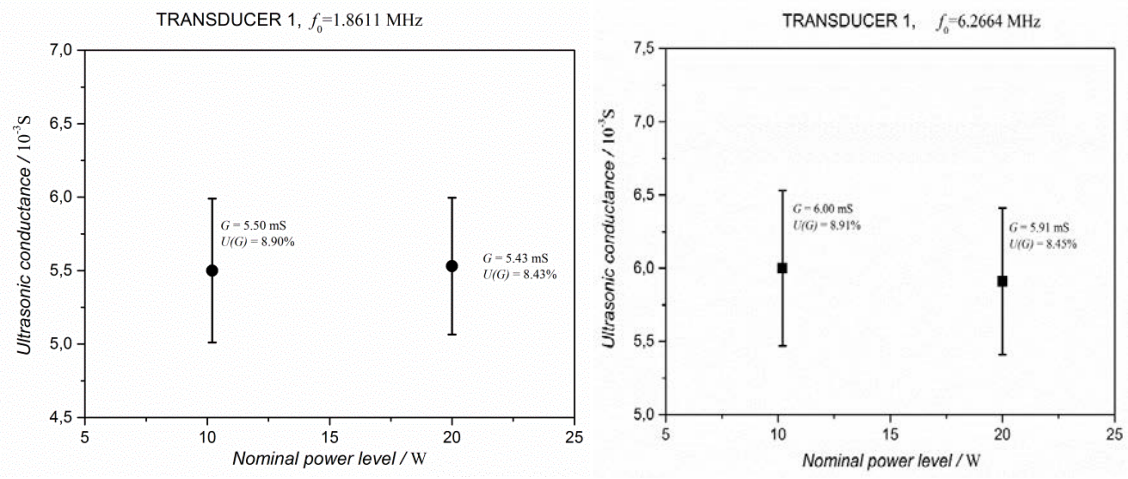

Figure 3.1. Transducer 1: ultrasonic conductance at two different power level.

TRANSDUCER 2

N	f_s /MHz	P / W	G / mS	U_{in} / V	U(G) / %
1	3.50	20	16.67	33.79	8.50
3	3.50	75	18.09	60.79	8.11
4	3.50	100	18.79	70.16	8.10

Table 3.3. Power level, frequency input voltage and ultrasonic conductance related to transducer 2.

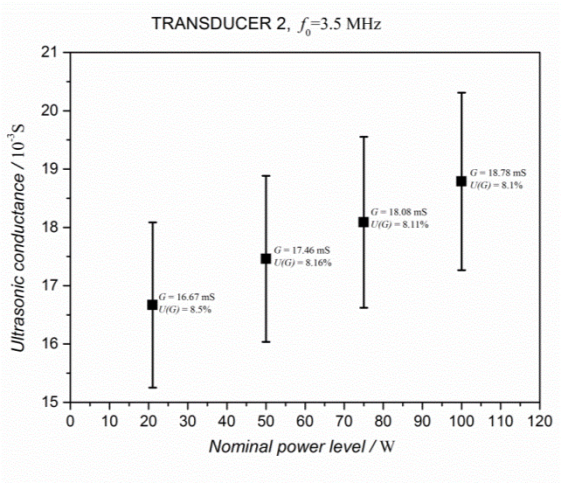

Figure 3.2. Transducer 2: ultrasonic conductance at four different power level.

TRANSDUCER 3

N	f_s /MHz	P / W	G / mS	U_{in} / V	$U(G)$ / %
1	2.00	20	12.20	38.42	8.66
2	2.00	50	12.22	61.73	8.27
3	2.00	75	12.24	78.77	8.21
4	2.00	100	12.42	89.45	8.20
5	6.38	20	13.68	38.89	8.60
6	6.38	50	13.34	61.92	8.25
7	6.38	75	13.17	76.07	8.20

Table 3.4. Power level, frequency input voltage and ultrasonic conductance related to transducer 3.

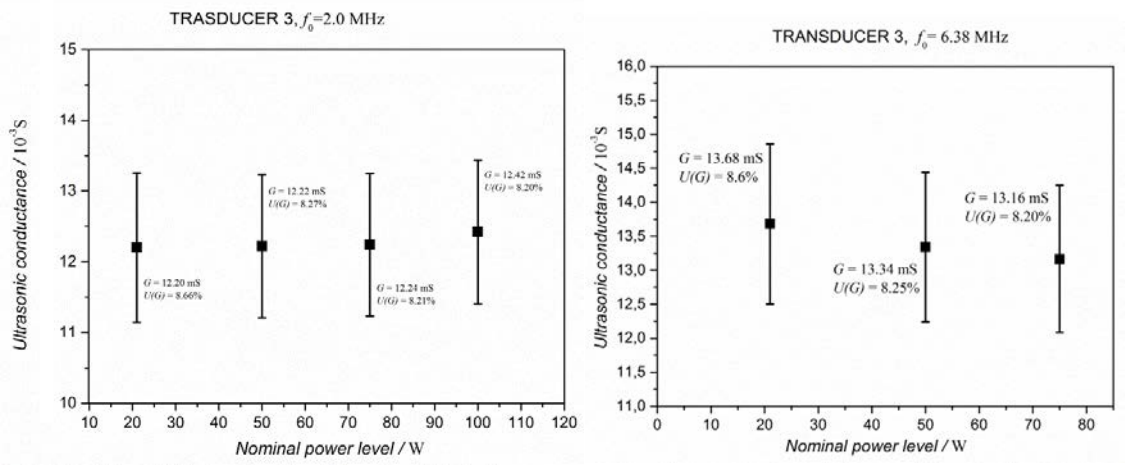

Figure 3.3. Transducer 3: ultrasonic conductance at three different power level

3.2 ULTRASOUNIC FIELD CHARACTERIZATION: PRESSURE

Subsequently to the measurement of the ultrasound power emitted by the three transducers, the acoustic pressure is measured. The ultrasonic measurement has been conducted in the scanning tank as described in paragraph 2.4.2.

To obtain a pressure field characterization, a series of planar scans are performed around the focus region and the pre focus region (10 mm from the focus) for each transducer. The aim of these scans has been to define the beam dimension and shape. Ultrasound sources are set for operating at 50 W. In figures 3.4, 3.5 and 3.6, a planar scan for each transducers, in the focused region and in pre-focused region (10 mm far from the focus) are shown. These are representative images from several independent experiments. The pressure 3-d diagram of an HIFU fields was performed using an optical hydrophone while a needle hydrophone (Onda PVDF needle, see table 2.1) is employed when a planar wave transducer is investigated.

For transducer 1 in the focus, the surfaces scanned have a dimension of 40 x 40 points with 1.00 mm resolution. Consequently, the planar scan requires 1600 points. For transducers 2 and 3, and transducer 1 at 10 mm from the focus, the surfaces scanned have a dimension of 30 x 30 points with 0.20 mm resolution, so that each planar scan requires 900 points. The planar scanning is always performed in *x*-*z* plane which is perpendicular to the propagation direction of the ultrasound beam.

For each measurement point the oscilloscope has acquired waveforms with a sampling frequency of 5 Gigasamples/s for a time period of 1000 ns. In order to reduce the random noise, each acquired electrical waveform has been the result of 10 averages. Each electrical waveform has been acquired and stored in the host PC for off-line conversion into acoustic pressure and elaboration.

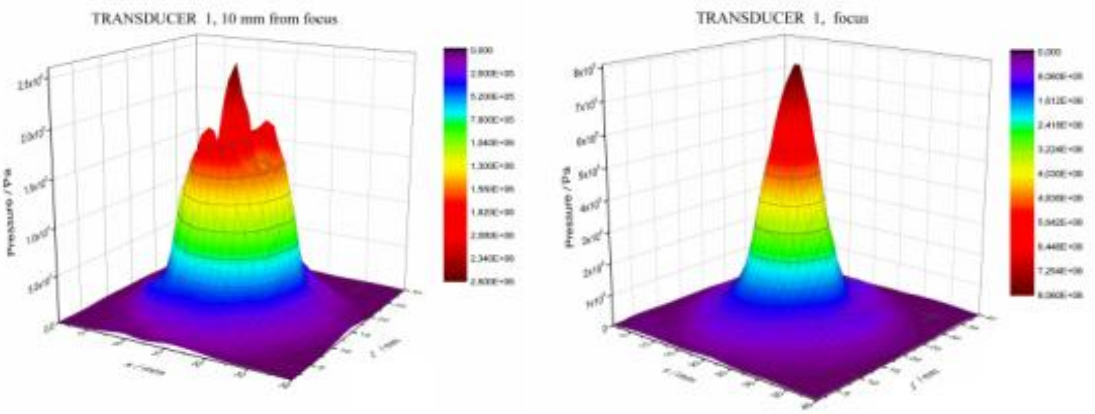

Figure 3.4**.** Three- dimensional representation of acoustic pressure measured in the focus (left) and pre-focus region (right) for transducer 1. The *x-z* plane is perpendicular to the propagation direction of the ultrasound beam.

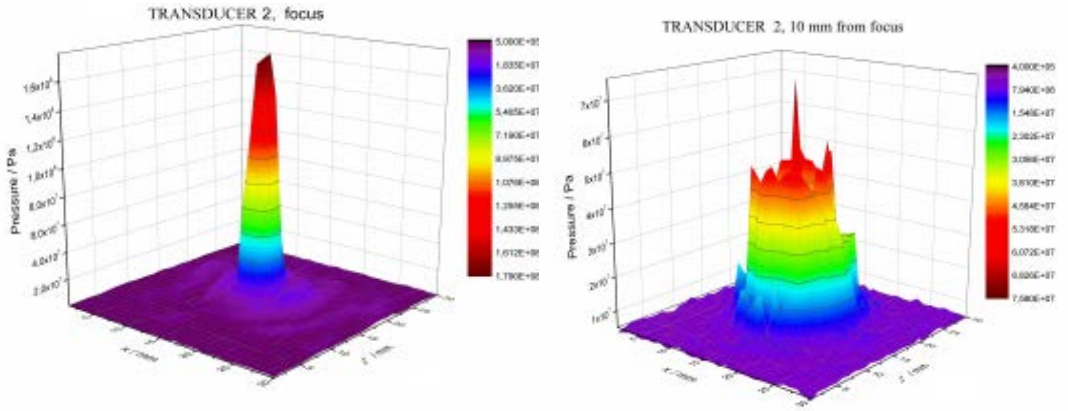

Figure 3.5. Three- dimensional representation of acoustic pressure measured in the focus (left) and pre-focus region (right) for transducer 2. The *x-z* plane is perpendicular to the propagation direction of the ultrasound beam.

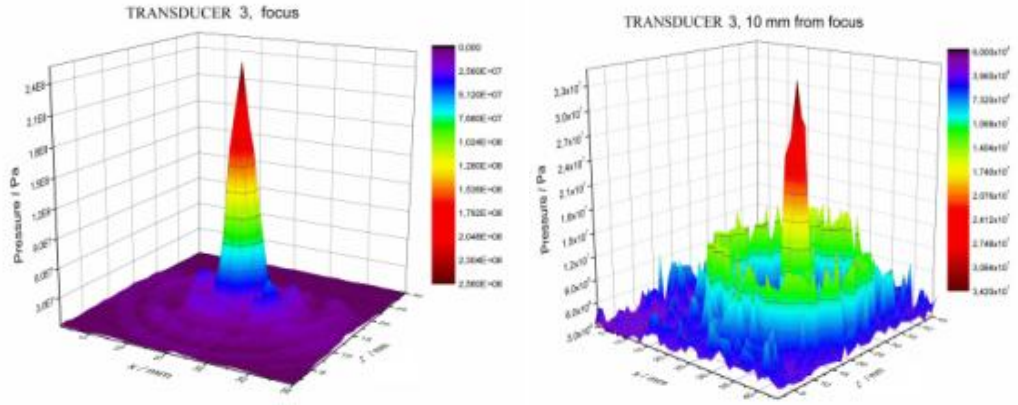

Figure 3.6. Three- dimensional representation of acoustic pressure measured in the focus (left) and pre-focus region (right) for transducer 3. The *x-z* plane is perpendicular to the propagation direction of the ultrasound beam.

The focus is situated at 55 mm for transducer 2 and at 63 mm for transducer 3 (see paragraph 2.2). Using transducer 1, piston-like transducer, the surface is scanned at 20 cm from the source, in the far field region.

It is easy to see from the graphs 3.4, 3.5 and 3.6 the pressure in the focus is higher for HIFU transducer (Transducer 2 and Transducer 3), than for a planar wave transducer (Transducer 1). For Transducer 2 and Transducer 3 the pressures in this point are respectively 1.6×10^8 Pa and 2.3×10^8 Pa, while for transducer 1 the maximum pressure reached is 7.5×10^6 Pa. In the graphs obtained using an HIFU source, it is also possible to observe that the pressure level reached in the pre-focused region is still high and, especially for the smaller transducer (Transducer 2), it is evident the presence of external "lobes" with high acoustic pressure level due to the more tapered shape of this transducer.

3.2.1 PRESSURE MEASUREMENT UNCERTAINTY

Here I present an overview of the main contributions to the final uncertainty associated to acoustic pressure measurement dividing if a needle hydrophone or a optic hydrophone is used.

PRESSURE UNCERTAINTY USING A NEEDLE HYDROPHONE

The voltage waveform $v(t)$ acquired by the hydrophone is converted in a pressure signal, $p(t)$, using the sensitivity curve of the hydrophone $M_L(f)$ according to:

$$p(t) = \frac{v(t)}{M_L(f)} \qquad \text{[MPa]} \qquad (2)$$

The pressure uncertainty, calculated according to the law of propagation, is:

$$u(p(t)) = \sqrt{u^2(v(t)) + u^2(M_L(f))} \qquad \text{[MPa]} \qquad (3)$$

Where:

- $u(v(t))$ is the type A uncertainty on the voltage values. It is calculated from the voltage value acquired by the hydrophone during a planar or linear scan when the transducer doesn't emits any waveform. Three independent measurements have been carried out and taken into account in the final result.
- $u(M_L(f))$ is the composed uncertainty associated to the product of the end of cable hydrophone sensitivity and a correction due to all the electrical load. $M_L(f)$ is calculated by:

$$M_L(f) = M_C \frac{C_H}{C_H + C_C + C_A} \qquad \text{[MPa]} \qquad (4)$$

and it is given by:

$$u(\mathrm{M_L(f)}) = \sqrt{c^2{}_{Mc}\left(u^2(M_C)\right) + c^2{}_{C_C}\left(u^2(C_C)\right) + c^2{}_{C_A}\left(u^2(C_A)\right) + c^2{}_{C_H}\left(u^2(C_H)\right)} \qquad (5)$$

where:

$u(M_C)$ is the type B uncertainty associated to the end of cable open circuit sensitivity;

$u(C_C)$ is the type B uncertainty associated to the right angle connection used to connect the pre-amplifier (Onda AH2020) and the hydrophone;

$u(C_A)$ is the type B uncertainty associated to the capacitance of the amplifier;

$u(C_H)$ is the type B uncertainty associated to the end of cable capacitance of the hydrophone;

Table 3.5 shows the uncertainty contribution to the $M_L(f)$*:*

	Contribution	X_i	x_i	c_{xi}	$u(x_i)$	$\lvert c_{xi}u(x_i)\rvert$
	$M_L(f)$	$M_L(f)$	$1.48\cdot10^{-7}$ V/Pa	-	$1.66\cdot10^{-8}$ V/Pa	-
1	$u(M_C(f))$	$M_c(f)$	$1.69\cdot10^{-7}$ V/Pa	0.87	$1.90\cdot10^{-8}$ V/Pa	$1.65\cdot10^{-8}$ V/Pa
2	$u(C_H)$	C_H	$6.32\cdot10^{-11}$ F	$0.29\cdot10^{-3}$ V/FPa	$1.58\cdot10^{-12}$ F	$4.65\cdot10^{-10}$ V/Pa
3	$u(C_C)$	C_C	$1.60\cdot10^{-12}$ F	$-2.05\cdot10^{3}$ V/FPa	$4.00\cdot10^{-14}$ F	$8.18\cdot10^{-11}$ V/Pa
4	$u(C_A)$	C_A	$7.50\cdot10^{-12}$ F	$-4.09\cdot10^{3}$ V/FPa	$1.88\cdot10^{-13}$ F	$7.67\cdot10^{-10}$ V/Pa

Table 3.5. Uncertainty contribution to $M_L(f)$

The uncertainty on the capacity of the hydrophone and of the other electrical loads are furnished by the producers (type B) and are usually on the order of less than 3% while the main contribution is given by the uncertainty on $M_C(f)$, which is usually more than 10%. This uncertainty is given by the laboratory that has calibrated the hydrophone and it can be quite different concerning what kind of hydrophone is used. In table 3.6 the main contributions to the uncertainty budget are expressed as relative quantities.

Source of uncertainty	*Relative uncertainty* / %
$v(t)$	2.83
$M_L(f)$	11.25
$u(p(t))$	11.60

Table 3.6. Uncertainty budget for pressure measurement using a needle hydrophone.

PRESSURE UNCERTAINTY USING A FIBER OPTIC PROBE HYDROPHONE

In this paragraph I give an overview of all the terms contributing to the final pressure uncertainty when a fiber optic hydrophone is used. Using this instrument, the relation to obtain pressure measurement is:

$$p = \left(\left(1.453 * \frac{1 - \sqrt{0.0019867 * \left(1 + (1+\alpha) * \frac{\Delta V}{V_0} \right)}}{1 + \sqrt{0.0019867 * \left(1 + (1+\alpha) * \frac{\Delta V}{V_0} \right)}} - 1 \right) / 0.329 \right)^{7.44} * 295.6 - 295.5 \quad \text{[MPa]} \quad (7)$$

while the composed uncertainty associated to pressure values is the sum in quadrature of three terms:

$$u(p(t)) = \sqrt{u^2(\alpha) + u^2(\Delta V) + u^2(V_0)} \quad \text{[MPa]} \quad (8)$$

Where:

- $u(\alpha)$ is the uncertainty of the internal light scattering factor of the optical hydrophone. α is given in paragraph 2.4.3 and is given by:
- $u(\Delta V)$*:* type A uncertainty associated to change of the photodetector signal in *V;*

- $u(V_0)$*:* is the type A uncertainty associated to DC photodetector signal at atmospheric pressure in *V;*

$$\alpha = \frac{1}{(V_w - V_B)/(V_{oil} - V_B) - 1} \tag{9}$$

while the uncertainty is calculated according to the law of propagation of the uncertainty, as

$$u\ (\alpha) = \sqrt{c_{V_w}^2\ \left(u^2(V_w)\right) + c_{V_B}^2\left(u^2(V_B)\right) + c_{V_{oil}}^2\left(u^2(V_{oil})\right)} \tag{10}$$

Where:

$u\,(V_W)$: is the type A uncertainty of the DC-photovoltage when the laser is on and the fiber tip is in water;

$u\,(V_B)$: is the uncertainty type A of the DC-photovoltage when the laser is off;

$u\,(V_{oil})$: is the uncertainty type A of the DC-photovoltage when the laser is on and the fiber tip is in the index-adjusted liquid;

Table 3.7 shows the uncertainty contribution to the internal light scattering factor α.

	Contribution	X_i	x_i	c_{xi}	$u(x_i)$	$\lvert c_{xi}u(x_i)\rvert$
	$u(\alpha)$	α	0.07	-	$1.82\cdot10^{-3}$	-
1	$u(V_W)$	V_W	0.81 V	$-1.14\cdot10^{-4}$ V^{-1}	$1.00\cdot10^{-3}$ V	$1.14\cdot10^{-4}$
2	$u(V_B)$	V_B	0.10 V	$-1.54\cdot10^{-3}$ V^{-1}	$0.50\cdot10^{-3}$ V	$7.70\cdot10^{-4}$
3	$u(V_{OIL})$	V_{OIL}	0.16 V	$1.65\cdot10^{-3}$ V^{-1}	$1.00\cdot10^{-3}$ V	$1.65\cdot10^{-3}$

Table 3.7. uncertainty contribution to the internal light scattering factor α.

The uncertainty of temperature values in Table 3.10 is dominated by estimate of the internal light scattering factor α with a constant relative contribution to $u(\alpha)$ = 2.44 %. Uncertainty on α values are problematic to reduce. For optimal functioning of the fiber optic probe hydrophone, the surface at the end of the fiber, which is the sensitive

element of the system, has to be properly cut. This is not always a clear and easy operation and, even if α values can be tolerated (if α < 0.3, parameter given to the manufacter to be accepted) some damage could be occur on the fiber tip. In figure 3.7 this phenomena is underlined: two images of the fiber tip are provided and in both cases α values are allowed (α = 0.07 in the left figure and α= 0.12 in the right figure) but a significantly difference occurs on the fiber tip, the second one is damaged and pressure values could be under estimated. The figures are provided using a scanning tunnelling microscopy.

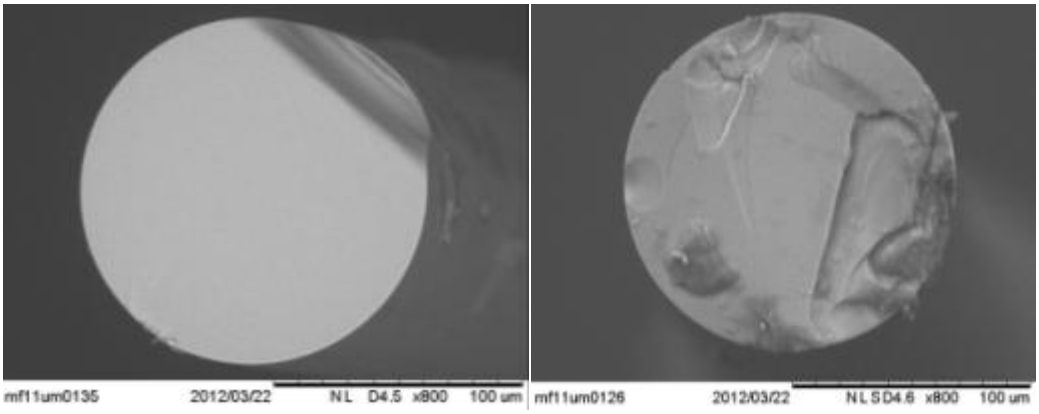

Figure 3.7. Two different images of the fiber tip provided using a scanning tunneling microscopy

In table 3.8 the uncertainty sources and their contributions to the final pressure uncertainty are summarized:

Source of uncertainty	*Relative uncertainty* / %
α	2.44
ΔV	2.22
V_0	0.16
$u(p(t))$	3.30

Table 3.8. Main contributions to the pressure uncertainty.

3.3 ULTRASOUNIC FIELD CHARACTERIZATION: TEMPERATURE

In the previous paragraphs the transducers characterization, regarding power and pressure has been provided. Beside them, in order to fully understand the effect of therapeutic focused ultrasound in tissue, accurate measurements of temperature rises are necessary. For this reasons a complete characterization of the temperature rise in the focus of an HIFU source is provided.

3.3.1 TEMPERATURE CHARACTERIZATION: COMPARISON BETWEEN THERMOCOUPLE AND FIBER OPTIC HYDROPHONE

As a first step, temperature rise near the focus of an HIFU transducer is provided using two different instruments: a fiber optic hydrophone and a thermocouple. Optical methods, for ultrasound field, is a new approach for temperature measurement that has been developed during this work. For this reason, thermocouples have been also applied in order to compare the optical hydrophone response when it is subjected to a temperature variation. A thermocouple and the optical hydrophone are embedded in a tissue mimicking material that simulates the thermal and acoustic properties of soft-tissue. The TMM chosen is a polyacrilamide gel realized at INRIM. The measurements are performed in the scanning tank system described in paragraph 2.4.2. This system allows the positioning of the optical fiber tip (which is the sensible part of the fiber) and the end of the thermocouple approximately at the focus of the transducer (the positioning is based on the prior knowledge of the parameters about the transducer). The fine adjustment of the position is then achieved by a temperature scanning in the region of interest with a smallest step (0.1 mm) in 3-dimensions. When the thermocouple and the fiber optic hydrophone are in the focal region, the temperature rise generated by the focused ultrasound reaches the maximum. To study the temperature elevation at the focal spot, the phantom is exposed to a power of 50W, 75W and 100W for an exposure time of 5 s. In these experiments, Transducer 3 has been used. Results are shown in Figure 3.8.

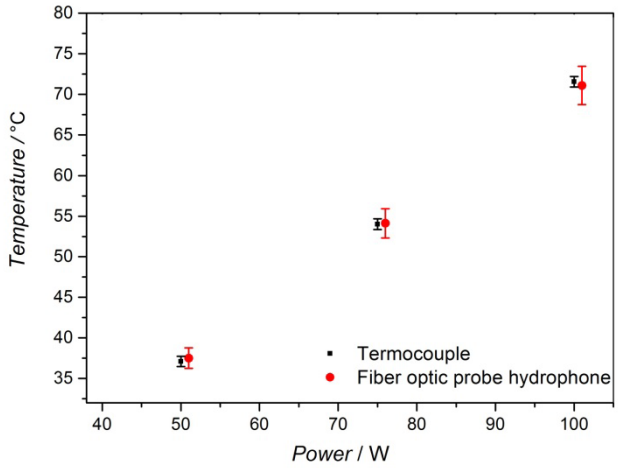

Figure 3.8. Temperature rise for three value of ultrasound power obtained using a thermocouple (square symbols) and an optical hydrophone (circle symbols).

In figure 3.8 the results obtained using the thermocouples (square symbols) are compared with the results achieved with an optic hydrophone (circle symbols) for the three power values taken into account. The graphs indicate that the measurements obtained with the different systems are not significantly different. The agreement between a traditional instrument for temperature measurements (thermocouple) and the new system based on an optical hydrophone is satisfactory and differences are within the calculated uncertainty (see paragraphs below).

3.3.2 TEMPERATURE CHARACTERIZATION: THERMOCOUPLES UNCERTAINTY

The uncertainty on temperature measurement, $u(T_T)$, is given by:

$$u(T_T) = \sqrt{u_r^2(T_T) + u_s^2(T_T)} \tag{10}$$

calculated as a combination of two components that constitute the uncertainty of the data:

- $u_r(T_T)$ is the type B uncertainty given to the laboratories which has been calibrated the thermocouple;
- $u_s(T_T)$ is the type A uncertainty associated with the sample measurements. It is the estimated variance of the mean which characterizes the variability of the values.

In the table below the uncertainty contribution associated to the three different values of ultrasonic power are summarized:

	Relative uncertainty / %		
	P = 50 W	P = 75 W	P = 100 W
	T = 37.10 °C	T = 54.02 °C	T = 76.00 °C
$u_r(T_T)$	0.90	0.90	0.96
$u_s(T_T)$	0.07	0.05	0.04
$u(T_T)$	0.91	0.90	0.96

Table 3.9. Main contributions to the temperature uncertainty using a thermocouple.

3.3.3 TEMPERATURE CHARACTERIZATION: FIBER OPTIC PROBE HYDROPHONE UNCERTAINTY

For a fiber optic hydrophone, the uncertainty is given by:

$$u(T_F) = \sqrt{u_s^2(T_F) + u_c^2(T_F)} \tag{11}$$

where:

- $u_s(T_F)$ is the type A uncertainty associated with the sample measurements, it is the estimated variance, deviation standard of the mean which characterizes the variability of the values.

- $u_c(T_F)$*:* is the composed uncertainty associated to the parameters which compare in equation 2.16 for temperature calculation. They are composed according to:

$$u_c(T_F) = \sqrt{u^2(\alpha) + u^2(\Delta V) + u^2(V_0) + u^2(T_0)} \qquad [°C] \tag{12}$$

Where: $u(\alpha)$: is the composed uncertainty associated to internal light scattering factor of the fiber optic system. It is already given in table 3.7

$u(\Delta V)$: type A uncertainty associated to change of the photodetector signal in *V;*

$u(V_0)$: type A uncertainty associated to DC photodetector signal at atmospheric pressure in *V;* ;

$u(T_0)$: type B uncertainty associated to water initial temperature °C;

The contributions to the uncertainty $u_c(T_F)$ of the temperature are summarized in Table 3.10.

Source of uncertainty	*Relative uncertainty* / %
α	2.44
ΔV	2.22
V_o	0.16
T_o	0.05
$U_c(T_F)$	3.30

Table 3.10. Contributions to the relative uncertainty of the temperature using a fiber optic probe hydrophone.

In the table below the uncertainty contribution associated to the three different values of ultrasonic power are summarized:

Source of uncertainty	*Relative uncertainty / %*		
	P = 50 W	P = 75 W	P = 100 W
	T = 37.50 °C	T = 54.12 °C	T = 71.1 °C
$u_c(T_F)$	0.57	0.34	0.35
$u_s(T_F)$	3.30	3.30	3.30
$u(T_F)$	3.35	3.31	3.32

Table 3.11. Main contributions to the temperature uncertainty using a FOPH hydrophone.

The uncertainty related to the measurement performed using an optical hydrophone are higher than the measurement realized with a thermocouple, but taking into account that

this is an instrument for the high pressure measurement, an uncertainty of 3.30% can be tolerated.

3.3.4 TEMPERATURE CHARACTERIZATION IN AGAR-BASED TMMs

In the previous paragraph the fiber optic hydrophone has been validated as temperature instrument. Now, using this instrument, temperature increase induced by a focused ultrasound field (Transducer 3) in another TMM (agar-based gel, described in paragraph 2.6.2) is evaluated. The experimental set up is the same used in the previous section. By means of a micro positioning system, the polyacrilamide TMM under study, including the optical fiber, is moved to reach the point of maximum revealed temperature, which is supposed to be the focus region of the ultrasound beam.

Firstly, the temperature elevation generated by an HIFU source (set to work at P=100 W) in the TMM phantom is spatially mapped in the focal plane. An *x*–*z* axes planar scan perpendicular to the propagation direction of the ultrasound beam is performed. In figure 3.9, a three- and two-dimensional representation of the temperature distribution is shown.

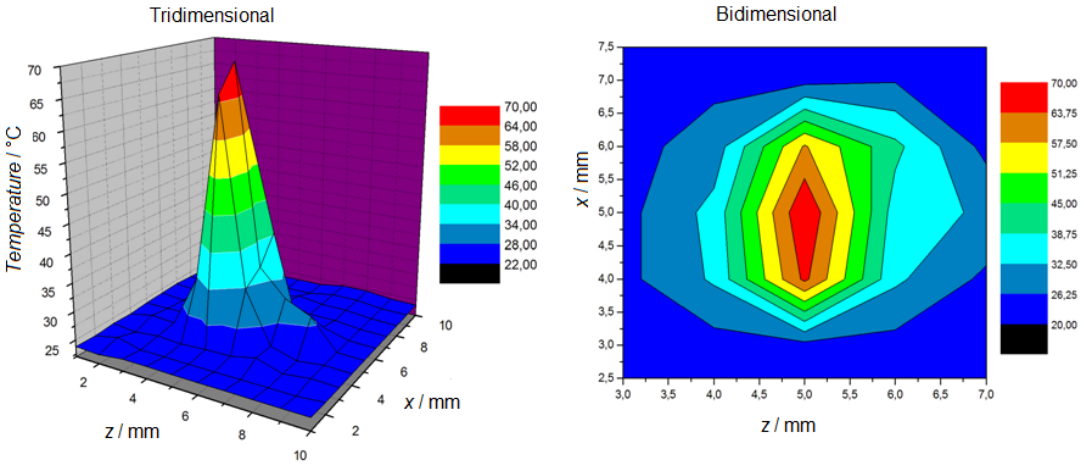

Figure 3.9. Three- and two-dimensional representation of the temperature spatial distribution around the ultrasound beam focus region. The colour map represents temperature variation from 20 °C to 70 °C.

The temperature reached in the focus is about 70°C. This value, obtained in a agar-based gel, is similar to those acquired in the same conditions (P = 100 W in the focus) using a polyacrilamide TMM. The uncertainty associated to the temperature increase has been already evaluated in paragraph 3.3.3, but in this case, only the contribution due to $u_c^2(T_F)$ is taken into account. In table 3.10 contributions to the temperature uncertainty are summarized.

Subsequently to a spatial scan of the temperature reached around the focus, temperature rises in different TMMs are performed. Four different Agar-based TMMs have been prepared, in order to study the changing in temperature increase when the percentage in volume of scattering agents (kieselguhr) is varied. Agar TMM have no scattering agents, while in Agar 2, 3 and 4 there is an increasing percentage in volume of them, respectively 2%, 3% and 4%. The TMMs are described accurately in paragraph 2.6.1. Even in this case, data are acquired by means of a fiber optic hydrophone when the gel is subjected to a focused ultrasound field produced at four different values of power (20W, 50W, 75W, 100W). The exposure time is 5 s every measurement. Temperature values are calculated as the mean of five measures realized for each measurement condition. In graph 3.10 data obtained are shown.

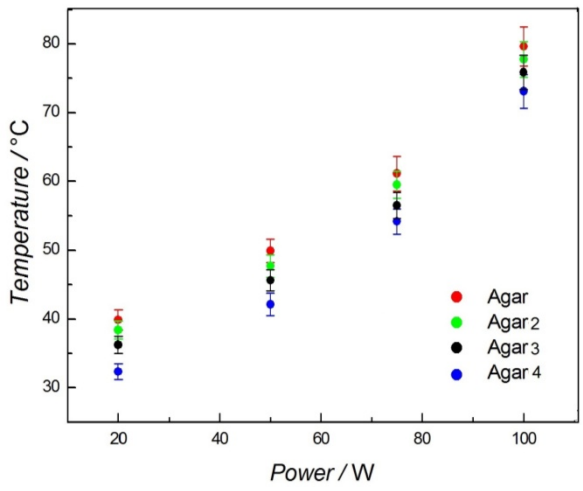

Figure 3.10. Temperature increase at different power values, in four Agar-based TMM.

From the graph it is possible to observe that increasing the percentage in volume of scattering agents, temperature variation during 5 s of exposure is reduced. This can be conducted to an increase of absorption and scattering phenomena caused by wave

interactions with structures or inhomogeneities of the medium (in this case: scattering agents). Error bar associated to temperature values are calculated as a quadrature combination of two components: the uncertainty relative to the fiber optic system (which components are described in table 3.10) and the uncertainty associated to the repeteability of the measuring data.

3.3.5 TEMPERATURE CHARACTERIZATION IN THERMOCHROMIC TMMs

After TMMs based on agar and polyacrilamide, a third sample has been synthesized. This is a thermochromic silica gel, an innovative TMM that allows not only the investigation of temperature rise, but also the "visualization" of the heating effects induced by an HIFU transducers.

QUALITATIVE EVALUATION OF TEMPERATURE EFFECTS

First of all, a quantitative evaluation of temperature effects has been provided, in order to visualize the heating regions, their shape and to verify the propriety of being reversible. In Figure 3.11 a sequence of the thermochromic gel exposed to the HIFU transducer 2 operating at 100 W is shown. It is possible to observe that, after the immediate formation of a blue region, in the focus, the heating effect propagates very rapidly towards the transducer, with the formation of blue “stream-lines” just after 300 ms (see fig 3.11, frame 8-9). A direct correlation of temperature, with color transition acquired, was difficult to performed since the optical conditions (illumination, presence of plexiglass windows with different thick) were not stable enough, however, on the bottom it is reported as a reference, a color scale graduated, as function of temperature, that have been recorded keeping a gel sample in a thermostatic bath. Indeed, from figure 3.11, it is possible to note the reversible propriety of this TMM .

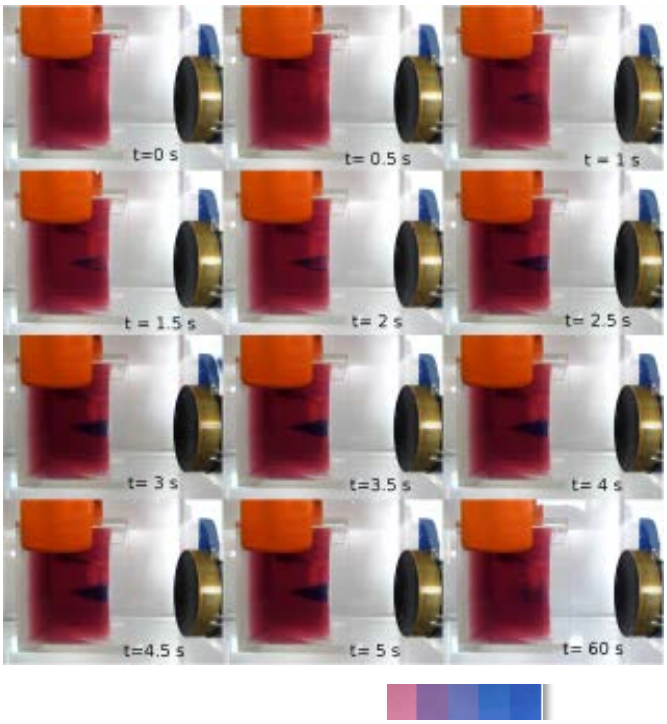

Figure 3.11. Sequence of color variation induced by HIFU transducer (Transducer 2, 100W). Frame period from top left: 0.5 s. Total insonation time. Last frame is reported to show the reversible effect

When conducting repeated experimental investigations, at high acoustic power (100 W) for longer time exposure (>2 s), the superheating, combined with mechanical effects, become dramatic and induces the formation of non reversible cavities, thus limiting the use of this material for trials at high power. As an example, in figure 3.12 are shown three frames of the gel exposed to 100 W for 5 s. Picture 3.12a: before to start the ultrasonic irradiation; 3.11b: immediately after that the ultrasonic irradiation was stopped, 3.12c: 60 s later respect to the frame 3.12b. In this last frame it is possible to see some small blue spots, which are cavities that probably are formed owing to the heating effect and a consequent lowering of cavitation threshold, probably associated with boiling phenomena.

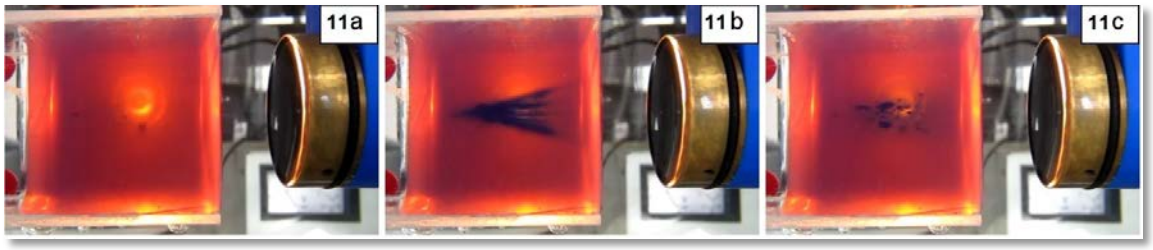

Figure 3.12. Sequence of color variation induced by HIFU transducer 2 (f =3 MHz, P=100W) for an insonation time of 5s. 11a before the radiation start, 11b just after the radiation was stopped, 11c 60 second after the radiation was stopped, in this last picture presence of cavities, due to mechanical damage of the TMM are well visible.

On Figure 3.13 it is shown a sequence of the thermochromic gel exposed to Transducer 3 working at 100 W. This picture shows that, although the acoustic power was similar, the different frequency and the different geometry of focusing of the transducer, causes a different “heating area”, highlighted by the color variation.

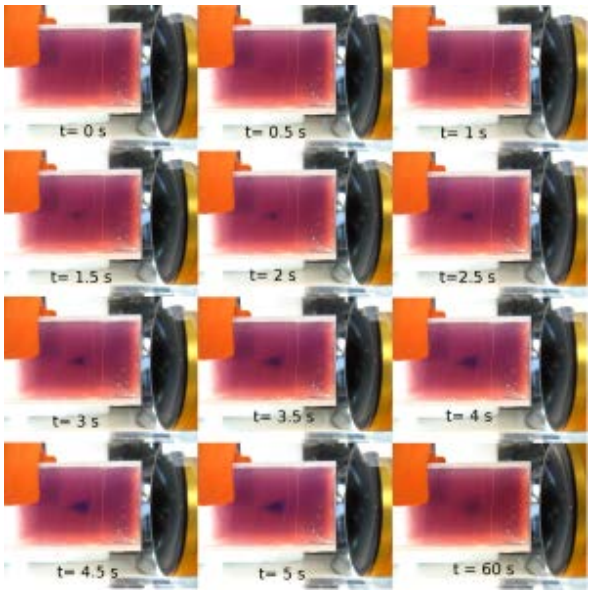

Figure 3.13: Temperature rise and subsequent color variation induced by Transducer 3 (HR-106 operating at 100 W frequency of 2 MHz for 5 sec). It is possible to note that the heating propagation effects are less evident maybe because of the different focalization’s shape.

From these preliminary observations we can affirm that: -a temperature of about 50 °C can be reached immediately even in the pre-focused region and the phenomenon is more evident when using a transducer with a more tapered shape; - the area in which is

possible to induce the rise of temperature is influenced by the shape of focused acoustic field.

Since, as it was evidenced by the 3-d acoustic pressure diagram reported in Fig. 3.5, the emission shape of Transducer 2 is more tapered and very high pressure levels are reached also in the pre-focused region, the formation of a larger heated area could be unsurprising but, more interestingly, this phenomenon has evidenced that, when working at typical power employed in medical application, several side effect, like anomalous heating or formation of cavities could occur during a longer exposure time (> of 2 s).

QUANTITATIVE EVALUATION OF TEMPERATURE RISE

Exploiting the very narrow color variation of the area exposed to focused ultrasound and the reversible properties of this material, temperature rise by means of a needle thermocouples inserted in different regions (focused and pre-focused) is evaluated. The measurement set up is reported in paragraph 2.6.3. All the performed measures, reported in table 3.12 and 3.13, are expressed in term of increment of T, since the starting temperature of the material was not the same for each measurement.

Insonation time / s	*Nominal Power* / W	Region	ΔT / °C	*Relative uncertainty* / %
5	20	Focus	19.91	3.08
5	50	Focus	21.58	2.54
5	100	Focus	34.91	2.22
5	50	Pre-focus	30.68	3.05
5	100	Pre-focus	32.11	2.65

Table 3.12. Increment of temperature measured in focus and pre-focus region using Transducer 2.

Insonation time / s	*Nominal Power* / W	Region	ΔT / °C	*Relative uncertainty* / %
2.00	20	Focus	28.08	3.10
2.00	50	Focus	35.35	2.98
2.00	100	Focus	50.40	2.35
2.00	50	Pre-focus	32.80	3.08
2.00	100	Pre-focus	44.61	2.93
5.00	20	Focus	32.02	2.72
5.00	50	Focus	39.01	2.40
5.00	100	Pre-focus	55.42	2.85

Table 3.13. Increment of temperature measured in focus and pre-focus region using Transducer 3.

The relative uncertainty to temperature values given in tables 3.12 and 3.13 are calculated as a composed uncertainty of two components: the type B uncertainty relative to the thermocouple ($u_R(T_T)$, which is given from the manufacturer and is described in paragraph 3.3.1) and the uncertainty associated to the repeatability of the measuring data ($u_s(T_T)$, estimated variance of the mean which characterizes the variability of the data).

On Figure 3.14 and 3.15 some examples of temperature rise with needle thermocouples using the two transducers are shown.

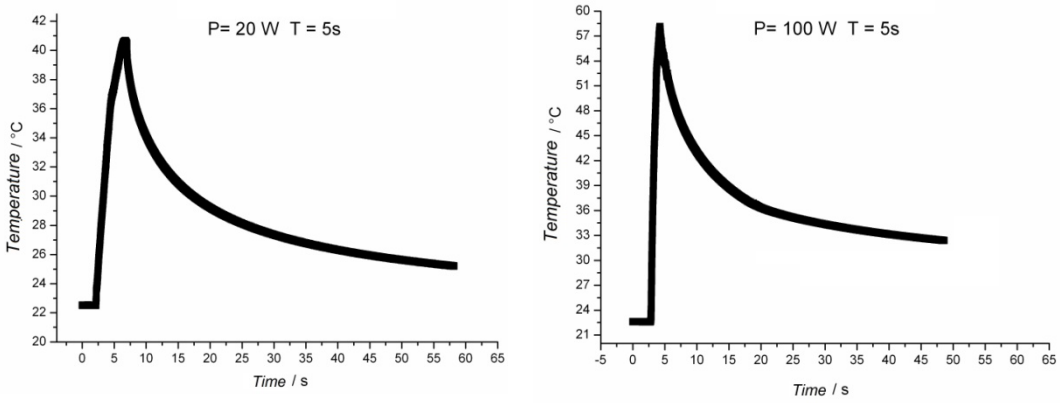

Figure 3.14: Increment of temperature measured in focus region using Transducer 2.

In figure 3.14, are shown two representative graphs registered at the same insonation time (5 s), varying the output power levels of the transducer (P = 20W in the left figure and P = 100W in the right). Increasing the power level, the temperature reached is higher. Moreover, the length of time necessary for temperature decreasing is longer for an output power of 100 W. After 50 s from the beginning of the insonation the temperature into the gel exposed to a power of 100 W is still 36 °C, while for a power level of 20 W the temperature reached is 25°C, almost the same of those before the insonation.

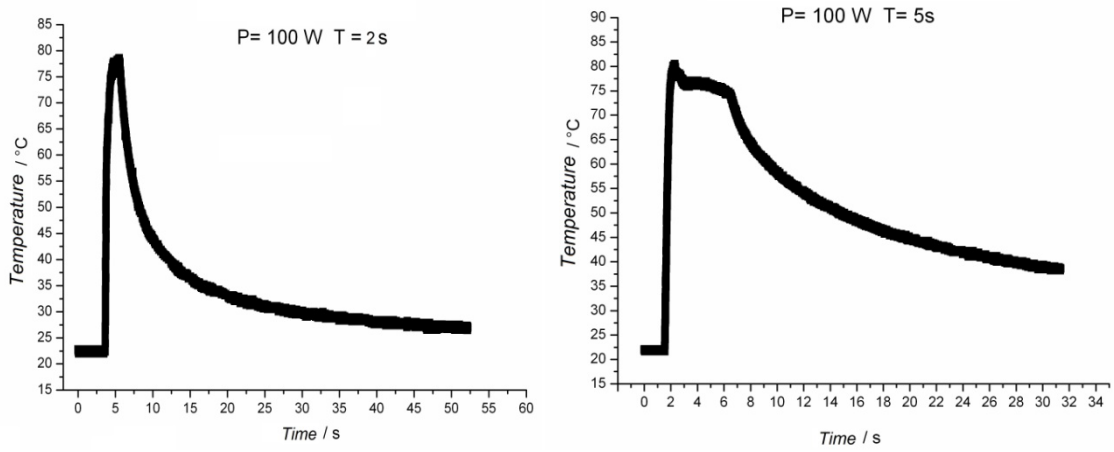

Figure 3.15: Increment of temperature measured in focus region using Transducer 3.

From the figure above it is possible to observe that even if the ultrasonic pressure is the same in the two measurements provides (P = 100W), temperature rise become very instable increasing the time of insonation, visible on a “plateau” in the graph of temperature rise. This is probably due to a chemical alteration of the gel: bubbles near the focus region and liquefaction of the gel itself can occur.

Beside these considerations, several papers have recently reported the artifact effect caused by viscous heating phenomena during evaluation of temperature rise induce by HIFU in tissues or TMM, measured with thermocouples. A rigorous evaluation of these artefact would require the knowledge of thermophysical parameters of the TMM but unfortunately I have not the possibility to measure them. Nevertheless, it is reasonable suppose that the overestimation of 10-15%, like those that have been reported, take place.

3.3.6 TEMPERATURE MEASUREMENT IN TMM AT IEO

After gel characterization and temperature rise evaluation performed in laboratory, the evaluation of temperature increase in a tissue-mimicking phantom induced by a USgFUS system at Istituto oncologico Europeo (IEO) in Milan. As seen in paragraph 1.4.6, the USgFUS is not able to provide treatment monitoring by thermal map which is allowed using MRgFUS. These activities are conducted with the aim to give some contribution in such sense, even considering the thermocouple artifacts described in paragraph before.

The measurements were performed on the JcHaifu apparatus. It has a single element transducer, with fixed focal length (160 mm), small focal region dimension and output frequency (1 MHz). The target lesion is covered and treated by moving the transducer. A cylindrical polyacrylamide gel phantom (60 mm radius, 40 mm height) was prepared in order to reproduce soft tissue behaviour (1023±5 g/cm density, 1550±23 m/s sound velocity, 0.067 ± 0.002 dB/cm attenuation Needle thermocouples, inserted in the phantom, were used to evaluate temperature increase (ΔT) at typical clinical settings (power outputs of 80W, 150W, 200W, 300W and sonication times of 3 s) inside the focus.

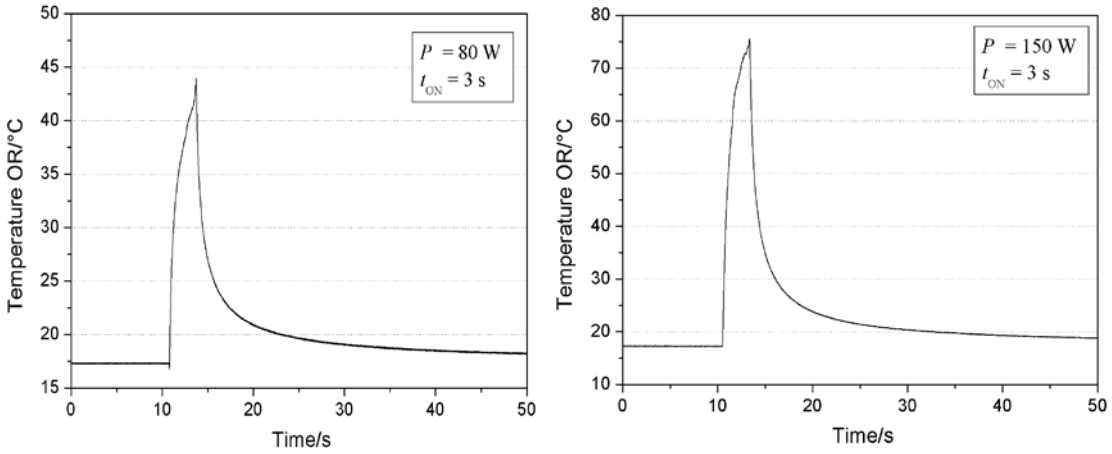

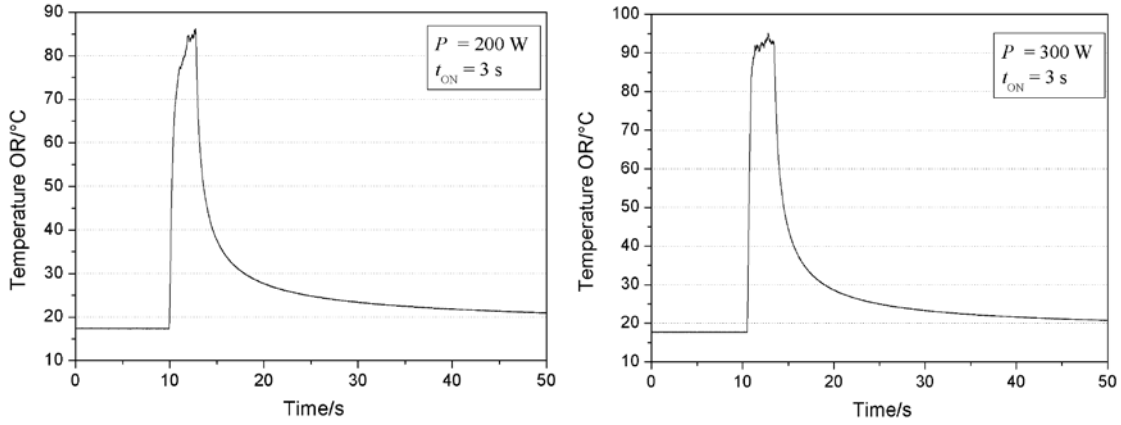

Figure 3.16. Typical rising curves of temperature recovered in focus region of an USgFUS apparatus.

Typical rising curves of temperature, with fixed time constant, were recovered, and exponential decrease was found when the HIFU field turned off. The maximum ΔT was reached inside the focus after 3 s of sonication, and was in the range of 45±5 °C, 75±5 °C, 85±5 °C and 92±3 °C for 80W, 150W, 200W and 300W power outputs, respectively. The absolute maximum temperature of 95 °C was never exceeded. As seen in the previous paragraph (and it can be also seen in figure 3.16 at P = 200 and 300 W), a damage of the gel occurs at high power emitted from the transducer. For this reason, repeatability of measurements was not possible after sonications at the highest power outputs (400W). In figure 3.17 the damage of the gel after insonation at P = 400 W for 3 s are visualized. The formation of an echoic region and the damage of the gel are underlined in the picture below.

Figure 3.17. Ecogenic formation and chemical alteration of the gel after 3 s of insonation at P =100 W.

In the measurements shown, the heated region is concentrated inside the geometrical focus, confirming the precision and high focalisation of the HIFU system. The high

temperatures reached could induce tissue boiling, however they are concentrated in the small focal region for less than 3s. Furthermore, the lower attenuation coefficient of gel phantom, the absence of interfaces compared with biological soft tissues, and viscous effects of needle thermocouples may have overestimated the ΔT. Thermal effects should be further studied in order to assure the validity of the treatment.

3.4 DEXTRANE NANOBUBBLES

In the following paragraph I will provide the results obtained with oxygen load nanobubbles, prepared using dextran as outer shell and perfluoropentane (PFP) or decafluoropentane as inner core. I will refer to dextran OLND for those prepared with DFP and dextran OLNB for those prepared with PFP.

3.4.1 CHARACTERIZATION OF DEXTRAN NANOBUBBLES

OLN COMPOSITION

In table 3.14. the compositions and the percentage weight/volume (w/v %) for OLND, OFND, OLNB, OFNB (oxygen free nanobubbles) and OSS (oxygen saturated solution) formulations are reported. Preparations A corresponds to OLND, OFND, OLNB, OFNB and OSS water liquid formulations, while preparations B corresponds to OLND, OFND, OLNB, OFNB and OSS 2% HEC gel formulations. Preparation C is the OLND in PBS liquid formulation. Preparation D corresponds to FITC-labeled OLND in PBS liquid formulation.

MORPHOLOGY

Dextran OLND and OLNB are prepared in liquid (water) or gel (HEC) formulations and has been checked for morphology by TEM or by optical microscopy. Results are shown in figure 3.18 as representative images from ten different preparations for each formulation. Panel A. TEM image of OLND water formulation. Magnification: 15500X. Panel B. Optical microscopy image of OLND water formulation. Magnification: 60X. Panel C. Optical microscopy image of OLND HEC formulation. Magnification: 60X. Panel D. TEM image of OLNB water formulation. Magnification:

15500X. Panel E. Optical microscopy image of OLNB water formulation. Magnification: 60X. Panel F. Optical microscopy image of OLNB HEC formulation. Magnification: 60X.

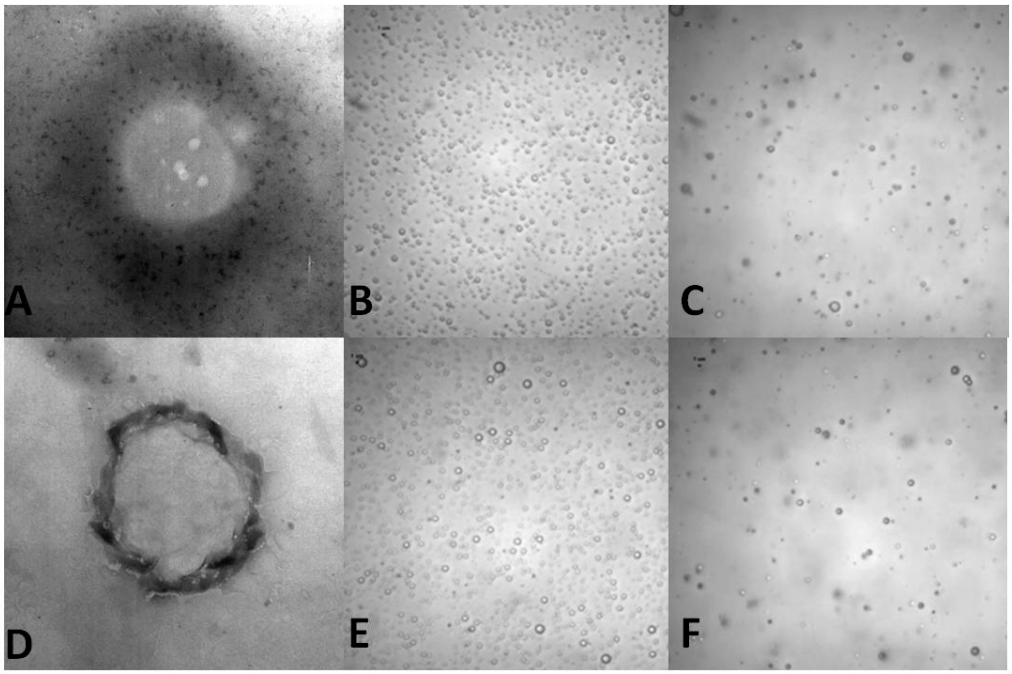

Figure 3.18. Dextran OLND and OLNB morphology.

SIZE, PARTICLE SIZE DISTRIBUTION AND ZETA POTENTIAL

Water formulations were characterized for average diameters (*d*), polydispersity index, and zeta potential by light scattering, and for oxygen content through a chemical assay. Results are shown as means ± SD from ten preparations (average diameters, polydispersivity index, and zeta potential) or three preparations (oxygen content) for each formulation. Results are shown in Table 3.15.

	fluorocarbon boiling point	*O_2 content* (g/ml+SD)		*d* (nm+SD)	*polidispersivity index*	*zeta potential* (mV+SD)
		before UV	after UV			
OLND	51 °C	0.43 ± 0.01	0.42 ± 0.01	596.35 ± 149.09	0.13	25.68 ± 1.00
OFND	51 °C	/	/	239.54 ± 96.20	0.10	25.17 ± 1.00
OLNB	32 °C	0.43 ± 0.01	0.42 ± 0.01	486.87 ± 147.62	0.11	27.31 ± 1.00
OFNB	32 °C	/	/	212.31 ± 94.82	0.95	26.54 ± 1.00
OSS	/	0.41 ± 0.01	0.40 ± 0.01	/	/	/

Table 3.15. Physical-chemical characterization of OLNDs, OFNDs, OLNBs, OFNBs and OSS.

Ingredients	OLNDs				OFNDs		OLNBs		OFNBs		OSS	
	Prep. A (%w/v)	Prep. B (%w/v)	Prep. C (%w/v)	Prep. D (%w/v)	Prep A (%w/v)	Prep. B (%w/v)	Prep. A (%w/v)	Prep. B (%w/v)	Prep. A (%w/v)	Prep. B (%w/v)	Prep. A (%w/v)	Prep. B (%w/v)
dextran sulfate	0.14	0.07	0.14	/	0.14	0.07	0.14	0.07	0.14	0.07	/	/
FITC-dextran sulfate	/	/	/	0.137	/	/	/	/	/	/	/	/
DFP	6.89	3.37	6.87	6.87	6.87	3.37	/	/	/	/	/	/
PFP	/	/	/	/	/	/	7.01	3.44	7.01	3.44	/	/
palmitic acid	0.02	0.02	0.02	0.02	0.02	0.01	0.02	0.01	0.02	0.01	0.02	0.01
Epikuron® 200	0.05	0.03	0.05	0.05	0.05	0.03	0.05	0.03	0.05	0.03	0.06	0.03
Pvp	0.07	0.03	0.07	0.07	0.07	0.03	0.07	0.03	0.07	0.03	0.08	004
ethanol	3.99	1.96	3.99	3.99	3.99	1.96	3.99	1.96	3.99	1.96	4.40	2.16
filtered H_2O	88.87	92.58	88.83	88.83	88.87	92.58	88.73	92.51	88.73	92.51	95.44	95.80
NaCl	/	/	0.03	0.03	/	/	/	/	/	/	/	/
sodium phosphate biphasic	/	/	0.01	0.01	/	/	/	/	/	/	/	/
HEC	/	1.96	/	/	/	1.96	/	1.96	/	1.96	/	1.96
O_2*	YES	YES	YES	YES	NO	NO	YES	YES	NO	NO	YES	YES

Table 3.14. Composition of OLND, OFND, OLNB, OFNB and OSS formulations.

Dextran OLND and OLNB water formulation were checked for size distribution by light scattering. Results are shown in figure 3.19 as a representative image from ten different preparations.

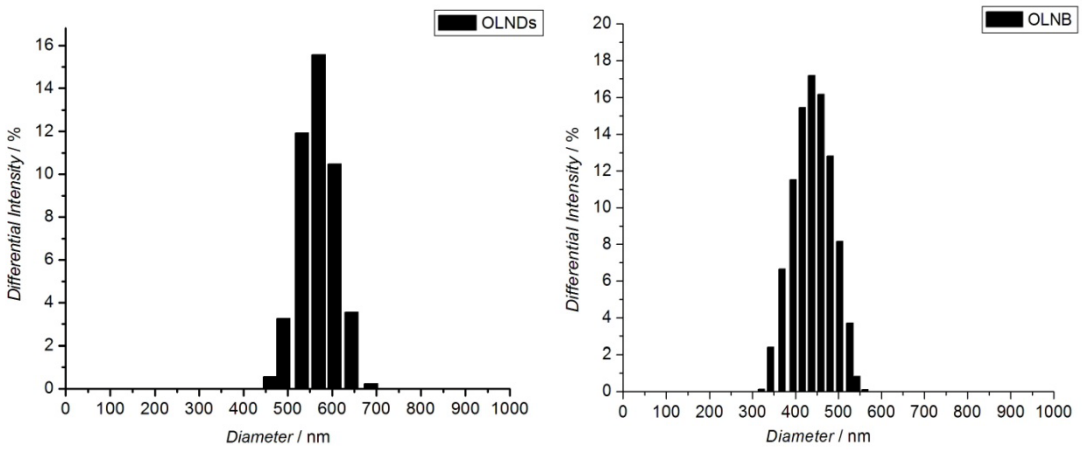

Figure 3.19 Dextran OLND and OLNB size distribution.

Either OLNDs or OLNBs displayed spherical shapes, nanometric sizes, with average diameters ranging from ~500 nm (OLNBs) to ~600 nm (OLNDs) for oxygen-loaded carriers and from ~210 nm (OFNBs) to ~240 nm (OFNDs) for oxygen-free carriers, and negatively charged surfaces as a consequence of the presence of sulfate groups in dextran molecule. OLNDs displayed also a good oxygen capacity, storing ~0.40 g/ml of oxygen either before or after UV sterilization. Such oxygen amount was similar to that of OLNBs or OSS, thus allowing the use of similar volumes of OLND, OLNB and OSS preparations during the subsequent experiments aimed at comparing *in vitro* and *in vivo* oxygen release abilities.

Current ONDs and ONBs displayed zeta potentials slightly higher than -30 mV. Nevertheless, formulations proved to be stable over time, as emerged from confirming analyses of OLD/OLB sizes and zeta potential performed by dynamic light scattering 72 h after manufacturing.

3.4.2 *II VITRO* DETERMINATION OF OXYGEN RELEASE FROM DEXTRAN OLNs

After nanobubbles characterization, their ability to release oxygen *in vitro* has been extensively studied. Firstly, oxygen-loading capacity has been evaluated without ultrasound and then several sonophoresis experiments have been performed. OLNs has been manufactured both in liquid and gel formulations. Gel formulation has been prepared in order to simulate a real treatment through the skin.

OXYGEN RELEASE WHITHOUT US

OLND, OLNB and OSS HEC gel formulations were monitored up to 6 h through an oxymeter for oxygen delivery by diffusion. The oxymeter displays an accuracy of 0.01 mg/l. Before each measurement, the oxymeter was calibrated in air, waiting for stable temperature and humidity conditions to be reached. Results are shown in figure 3.20 as a representative image from three independent experiments.

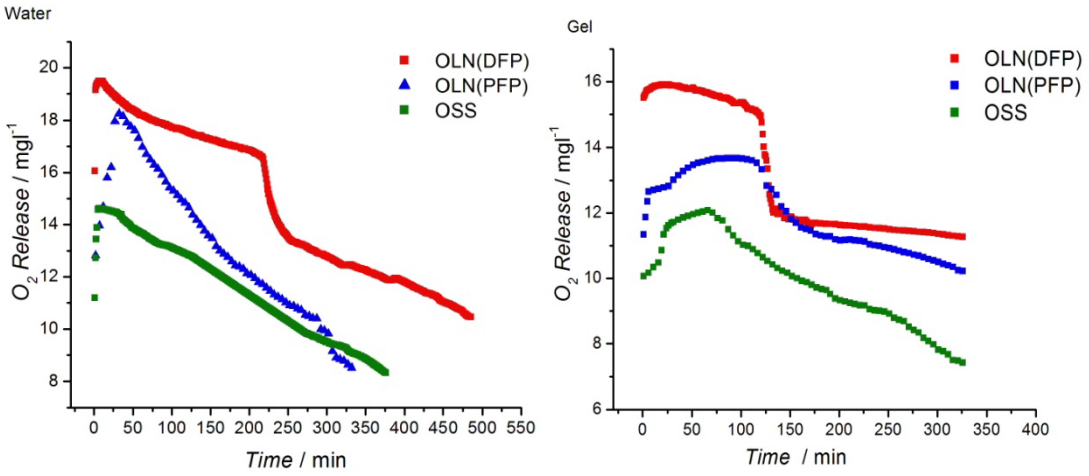

Figure 3.20. *In vitro* oxygen release from dextran OLND and OLNB liquid and gel formulation.

From graph 3.19 appears that OLNs also had a good oxygen-loading capacity. This was due to the presence of fluorocarbons, as DFP and PFP can favor oxygen entrapment. Both OLND and OLNB displayed a very good ability to deliver O_2 at high concentrations and for long times, either in water or gel formulations; nevertheless, DFP-containing OLNs appeared more effective than those with PFP, OSS did deliver high O_2 concentrations, but for shorter times than OLNs, as expected.

OXYGEN RELEASE WITH US AND TRESPASSING OF SKIN MEMBRANES

As described in paragraph 1.5.4. sonophoresis is a process that exponentially increases the absorption of topical compounds (transdermal delivery) into the epidermis, dermis and skin appendages by ultrasonic energy. To verify the ability of ultrasound (US)-activated OLNs to release O_2 through biological membranes, an homemade experimental apparatus has been used. This is composed by an US probe with a high frequency transducer (f = 2.5 MHz; P = 5 W), combined with a home-made apparatus with two sealed cylindrical chambers separated by a layer of pig ear skin employed as a model of biological membrane (see paragraph 2.7.6 for more detail). The US transducer (f = 2.5 MHz; P = 5 W) was alternatively switched on and off at regular time intervals of 5 min for an overall observational period of 135 min, and oxygen concentration in the recipient chamber was monitored by Hach Langhe LDO oxymeter every 45 min. Because of the local heating caused by US, the O_2 sensor was positioned laterally in order to prevent possible damage of the oxymeter, whereas the transducer was held in a fixed position. within the donor compartment. The acoustic power of the transducer was determined through a balance's radiation force with a reflecting target, with an uncertainty of 4%.

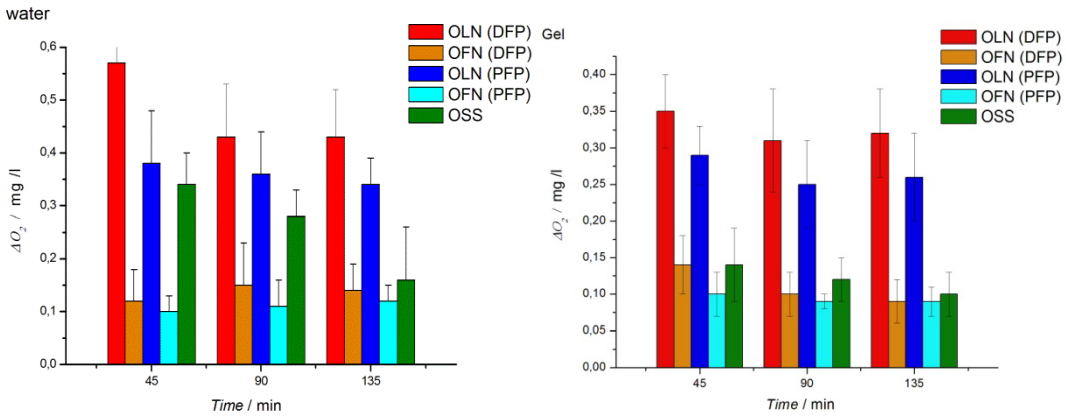

Figure 3.21. US abilities to induce sonophoresis and oxygen release from dextran OLN and control HEC gel formulations.

US improved the ability of both liquid and gel OLND formulations to cross the pig skin membrane and to release oxygen into the hypoxic chamber, being such oxygen release significantly larger than that from OFNDs, OLNBs, OFNBs, and OSS formulations. Even in this case. OLND appears more effective than OLNB. On the contrary, OFNs

did not release significant O_2 amounts, whereas OSS did deliver high O_2 concentrations. but for shorter times than OLNs, as expected. The efficacy of OLNs in releasing O_2 on skin models is particularly crucial in order to verify the hypothesis that OLNs might help to restore the physiological level of oxygenation in cancerous tissues in which there is an oxygen deficiency.

3.4.3 BIOCOMPATIBILITY ASSESSMENT

Before in vivo applications, the biocompatibility assessment of dextran OLND regarding nanobbubbles cytotoxicity and cell viability have been studied. The cells in which the measurement are performed are human keratinocytes (106 cells / 2 ml Panserin medium). These were untreated (upper panels) or treated with 200 μl FITC-conjugated OLND PBS formulation (lower panels) for 24 h in normoxia (20% O_2). After DAPI staining, cells were checked by confocal microscopy. Results are shown as representative images from three independent experiments. Left panels: blue caption (cell nuclei after DAPI staining). Central panels: green caption (FITC-conjugated OLNDs). Right panels: merged caption. Magnification: 63X.

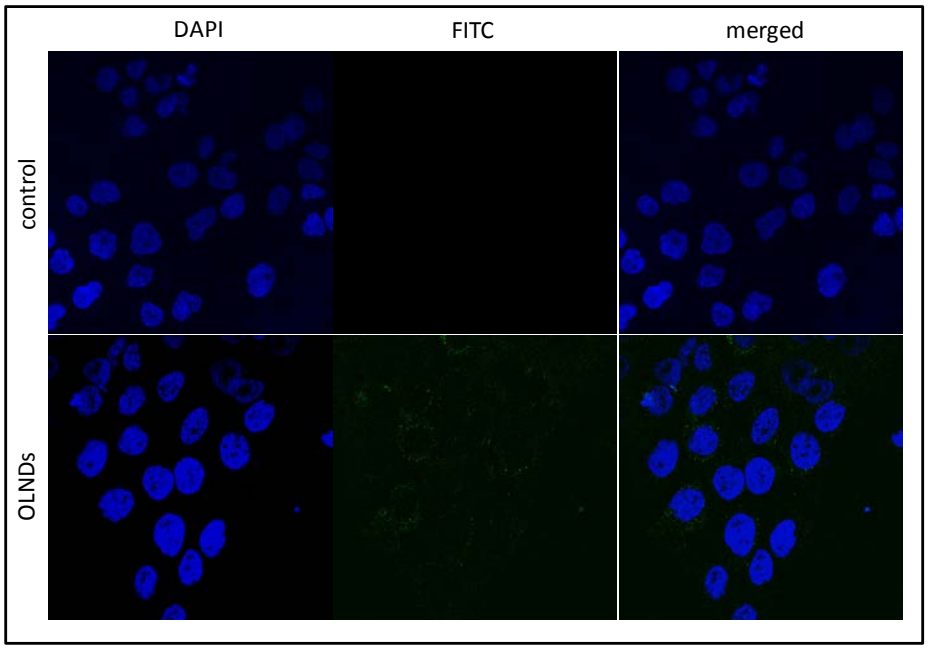

Figure 3.22. Dextran OLND internalization by HaCaT cell line.

As emerged from analysis by confocal microscopy. FITC-conjugated OLNDs were avidly internalized by HaCaT cells.

OLND CYTOTOXICITY

Human keratinocytes (10^6 cells / 2 ml Panserin medium) were left untreated or treated with different doses (100-400 μl) of OLND PBS formulation for 24 h in normoxia (20% O_2; white-squared curve) or hypoxia (1% O_2; black-squared curve). After collection of cell supernatants and lysates, OLND cytotoxicity was measured through LDH assay. Results are shown as means+SEM from three independent experiments. Data were also evaluated for significance by ANOVA. Versus normoxic untreated cells: p not significant.

HUMAN KERATINOCYTE CELL VIABILITY

Human keratinocytes (10^6 cells / 2 ml Panserin medium) were left untreated or treated with different volumes (100-400 μl) of OLND PBS formulation for 24 h in normoxia (20% O_2; white-squared curve) or hypoxia (1% O_2; black-squared curve). Thereafter, cell viability was measured through MTT assay. Results are shown as means+SEM from three independent experiments. Data were also evaluated for significance by Student's *t* test. Versus normoxic untreated cells: *p< 0.01; **p< 0.001; ***p<0.0001.

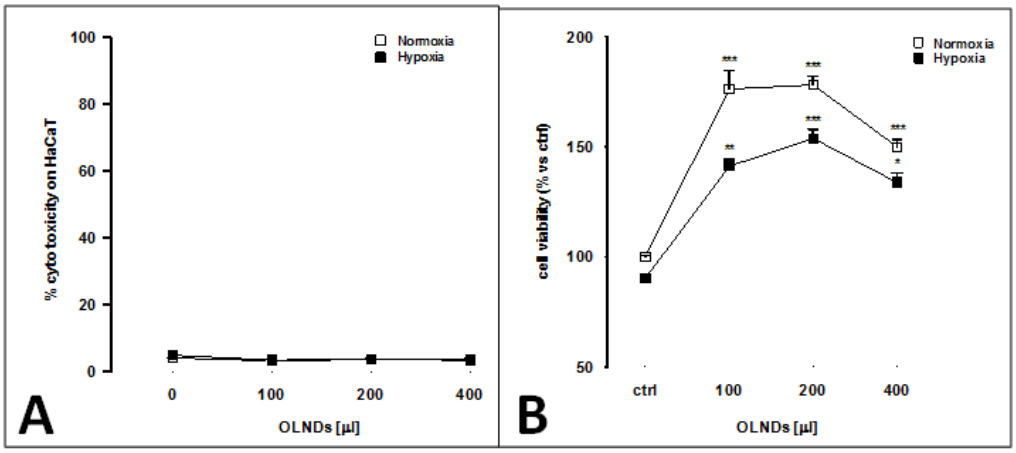

Figure 3.23. Cytotoxicity and viability of HaCaT cell line after dextran OLND treatment.

Investigation through lactate dehydrogenase (LDH) assay (Figure 3.22) showed that different doses of OLNDs, ranging from 100 to 400 μl, did not result toxic for cells, both in normoxic (20% O2) and hypoxic (1% O2) conditions, and eventually OLNDs

proved to be effective to improve dose-dependently keratinocyte viability, either in normoxia or hypoxia.

3.4.4 *IN VIVO* DETERMINATION OF OXYGEN RELEASE FROM OLNDs

After *in vitro* experiments. two different measurements to evaluate the OLNs ability to release oxygen in vivo has been performed. Oxygen release have been monitored in photoacoustic experiments and throught transcutaneous oxygenation.

PHOTOACOUSTIC IMAGING

Shaved hind limbs of anaesthetized mice were monitored by photoacoustics for oxy-and deoxy-Hb levels before (0 min. upper row), during (0-10 min. central row) and after (10 min. lower row) topical treatment with OSS (first column), OLND (second column) and OFND (third column) gel formulations. White/red pixels: oxy-Hb; blue pixels: deoxy-Hb. Data are shown in figure 3.24 as representative images from three independent experiments (three mice per experiment) with similar results.

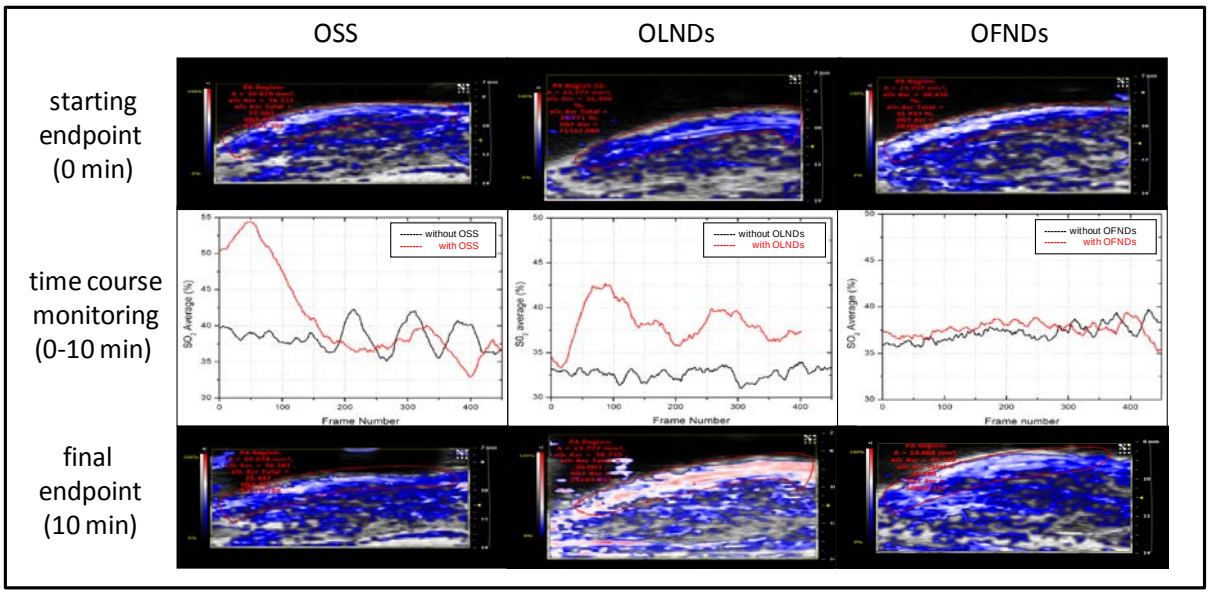

Figure 3.24. Topical treatment with dextran OLND gel formulation effectively enhances oxy-Hb levels *in vivo*.

Photoacoustic monitoring revealed that oxy-Hb levels significantly increased for the entire observational period in the animals treated with OLNDs while, as expected. OSS induced a high but only transient peak in oxy-Hb, whereas OFNDs did not affect oxy-/deoxy-Hb balances at all.

MEASUREMENT OF *TcpO₂* WITH US

Shaved abdomens of anaesthetized mice were topically treated with OLND gel formulation and ultrasonicated for 15 sec (*f* = 1 MHz), Before and after treatment. *tcpO₂* was monitored through TINA TCM30 oxymeter. Panel A. Short-term time-course (0-15 min) *tcpO₂* monitoring of three mice before and after treatment with OLND gel formulation. Data are shown as means±SD. Results were also analyzed for statistical significance by Student's *t* test. Versus untreated mice: $p<0.02$. Long-term end-point (1 h) *tcpO₂* measurement of five mice before and after treatment with OLND gel formulation. Data are shown individually per each mouse (m 1-5).

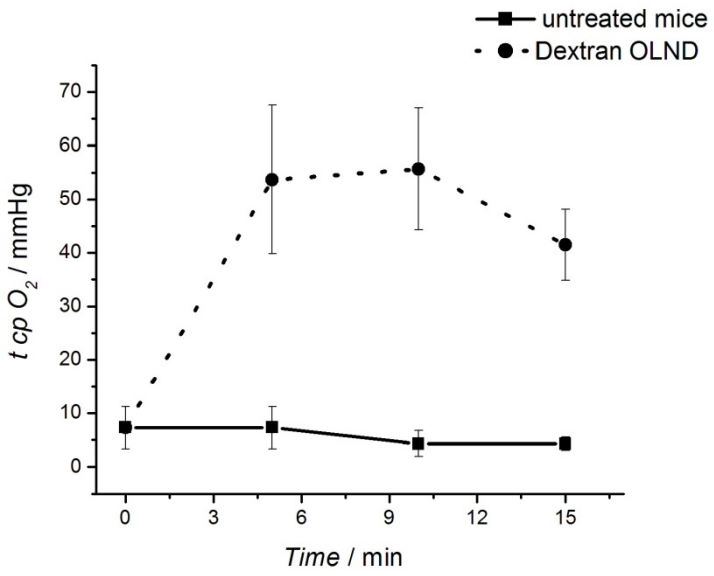

Figure 3.25. Topical treatment with US-activated dextran OLNDs effectively enhances *tcpO₂ in vivo*.

After topical administration of US-activated OLNDs, hypoxic mice displayed larger oxygenation levels in a time-sustained manner, OLNs significantly increased transcutaneous capillary oxygenation in topically treated mice.

STATISTICAL ANALYSIS

Every characterization of ten preparations for each formulation was performed in triplicate, and results are shown as means + SD (light scattering and oxygen measurement) or as a representative image (TEM and optical microscopy). Data from cell studies are shown as means + SEM (LDH and MTT) or as a representative image (confocal microscopy) from three independent experiments analyzed in duplicate. Results from *in vitro* oxygen release studies are shown as a representative image (release without US) or as means ± SD (release with US) from three independent experiments. Results from *in vivo* oxygen release studies are shown as a representative image (release without US) or as means ± SD (release with US) from 5-9 mice. SD or SEM were used for descriptive or inferential information. respectively. Data were analyzed for significance by Student's *t* test or by a one-way Analysis of Variance (ANOVA).

3.5 CHITOSAN NANOBUBBLES

In the following paragraph I will provide the results obtained with oxygen load nanobubbles prepared using chitosan as outer shell and perfluoropentane (PFP) or decafluoropentane as inner core. Even in this case, I will refer to chitosan OLND for those prepared with DFP and dextran OLNB for those prepared with PFP. Like dextran nanobubbles, also these preparations have been characterized. The ability to release oxygen with and without ultrasound has been studied and *in vivo* experiments has been performed.

3.5.1 CHARACTERIZATION OF CHITOSAN NANOBUBBLES

OLN COMPOSITION

In table 3.16, the composition and the percentage weight/volume (w/v %) for CHITOSAN OLND, OFND, OLNB, OFNB and OSS formulations are reported. Preparations A corresponds to OLND, OFND, OLNB, OFNB and OSS water liquid formulations, while preparations B corresponds to OLND, OFND, OLNB, OFNB and OSS 2% HEC gel formulations. Preparation C is the OLND in PBS liquid formulation. Preparation D correspond to FITC-labeled OLND in PBS liquid formulation.

MORPHOLOGY

The morphology of chitosan nanobubble, both OLND and OLNB formulations was assessed by transmitting electron microscopy (TEM) (Philips CM10) and by optical microscopy (XDS-3FL). OLNs were dropped onto a Formwar-coated copper grid and air-dried before observation. Results are shown in figure 3.25.

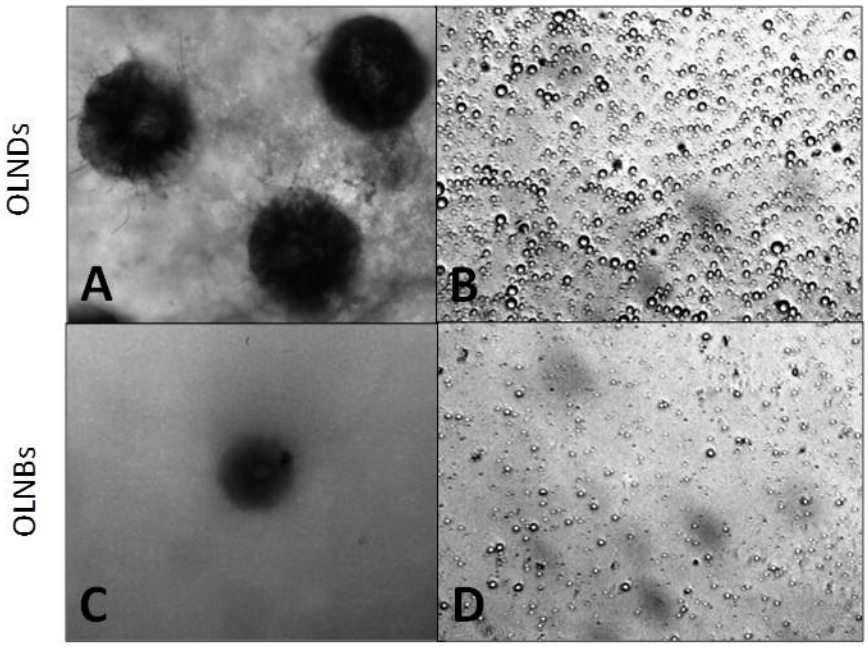

Figure 3.26. Chitosan OLND and OLNB were checked for morphology by TEM or by optical microscopy. Results are shown as representative images from ten different preparations for each formulation. Panel A. TEM image of OLNDs. Magnification: 15500X. Panel B. Optical microscopy image of OLNDs. Magnification: 630X. Panel C. TEM image of OLNBs. Magnification: 52000X. Panel D. Optical microscopy image of OLNBs. Magnification: 630X.

Ingredients	OLNDs		OFNDs		OLNBs		OFNBs		OSS	
	Prep. A (%w/v)	Prep. B (%w/v)	Prep. A (%w/v)	Prep. B (%w/v)	Prep. A (%w/v)	Prep. B (%w/v)	Prep. A (%w/v)	Prep. B (%w/v)	Prep. A (%w/v)	Prep. B (%w/v)
chitosan (medium M_W)	0.14	0.07	0.14	0.07	0.14	0.07	0.14	0.07	/	/
DFP	6.87	3.37	6.87	3.377	/	/	/	/	/	/
PFP	/	/	/	/	7.01	3.44	7.01	3.44	/	/
palmitic acid	0.02	0.02	0.02	0.01	0.02	0.01	0.02	0.01	0.02	0.01
Epikuron® 200	0.051	0.025	0.051	0.03	0.05	0.03	0.05	0.03	0.06	0.03
pvp	0.070	0.034	0.070	0.03	0.07	0.03	0.07	0.03	0.08	0.04
ethanol	3.98	1.96	3.98	1.96	3.98	1.96	3.99	1.96	4.40	2.16
filtered H_2O	88.87	92.58	88.87	92.58	88.73	92.51	88.73	92.51	95.44	95.80
HEC	/	1.960	/	1.96	/	1.96	/	1.96	/	1.96
O_2*	YES	YES	NO	NO	YES	YES	NO	NO	YES	YES
* O_2 is merely indicated for its presence/absence in the solution (YES/NO), as it was added in excess to reach saturation; the specific O2 content was further measured during characterization. as shown in Table 2										

Table 3.16. Composition of OLND, OFND, OLNB, OFNB and OSS formulations.

SIZE, PARTICLE SIZE DISTRIBUTION AND ZETA POTENTIAL

Average diameters, polydispersity indexes, and zeta potentials of nanodroplets and nanobubbles were determined by dynamic light scattering using Delsa Nano C instrument, which portrays the particle size distribution of samples in the diameter range 0.6 nm - 7µm. Each reported value is the average of 10 independent measurements of 3 different formulations. The polydispersity index assesses the size distribution within a nanodroplet or nanobubble population. For the zeta potential determination, formulation samples were placed into an electrophoretic cell, where an electric field of approximately 30 V/cm was applied. The electrophoretic mobility was converted into zeta potential using the Smoluchowski equation. Each sample was analyzed in triplicate. Results are shown in Table 3.17.

	Fluorocarbon boiling point	*O_2 content* (g/ml+SD)		*diameters* (nm+SD)	*Polidispersivity index*	*zeta potential* (mV+SD)
		before UV	after UV			
OLND	chitosan	DFP	51 °C	0.46 ± 0.01	0.45±0.01	726.55 ± 123.07
OFND	chitosan	DFP	51 °C	/	/	332.70 ± 101.10
OLNB	chitosan	PFP	32 °C	0.45 ± 0.01	0.44 ± 0.01	745.20 ± 117.89
OFNB	chitosan	PFP	32 °C	/	/	320.40 ± 100.90
OSS	/	/	/	0.41 ± 0.01	0.40 ± 0.01	/

Table 3.17. Physical-chemical characterization of OLNDs, OFNDs, OLNBs, OFNBs and OSS.

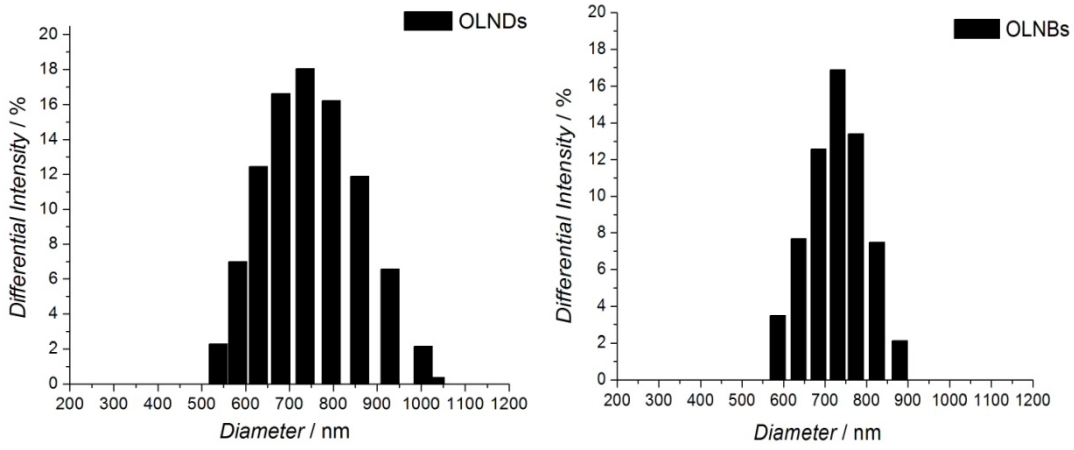

Figure 3.27. Chitosan OLND and OLNB size distribution.

OLND and OLNB water formulations were checked for size distribution by light scattering. Results are shown as representative image from ten different preparations for each preparation. Panel A. OLND size distribution. Panel B. OLNB size distribution.

Either chitosan OLND and OLNB (nanodroplets and nanobubbles) displayed spherical shapes and nanometric sizes, with average diameters ranging from ~720 nm (OLNDs) to ~740 nm (OLNBs) for oxygen-loaded carriers and from ~320 nm (OFNBs) to ~330 nm (OFNDs) for oxygen-free carriers. Moreover, nanodroplets and nanobubbles displayed cationic zeta potentials ranging from ~ +35 mV for oxygen-loaded carriers to ~ +40 mV for oxygen-free carriers. These values implicate that OLNDs are physically stable as a consequence of the electrostatic repulsion of the polymer chains. Indeed, the zeta potential measures charge repulsion or attraction between particles and is a fundamental parameter to determine nanoparticle physical stability, with zeta potentials lower than -30 mV or higher than +30 mV being generally required for physical stability of colloid systems. Consistently, further 72 h-monitoring of sizes and zeta potentials of OLNDs confirmed their physical stability over time (not shown). The cationic surfaces were a clear consequence of the presence of chitosan, which is positively charged in the shell. Interestingly, it has been proposed that surface-charged nanoparticles are exquisitely suitable for topical treatment, as surface charges enhance nanoparticle interaction with skin and improve their therapeutic effect on inflamed cutaneous tissues, either without or with concomitant US treatment. In particular, cationic nanoparticles are generally recommended for topical treatment due to the anionic nature of the skin.

3.5.2 *IN VITRO* DETERMINATION OF OXYGEN RELEASE FROM OLNS

OXYGEN RELEASE WITHOUT US

O_2 release by diffusion from OLND, OLNB and OSS liquid or gel formulations was estimated by monitoring O_2 concentration up to 7 h through Hach Langhe LDO oxymeter, displaying an accuracy of 0.01 mg/l. The oxymeter was calibrated in air, waiting for stable temperature and humidity conditions to be reached before each measurement.

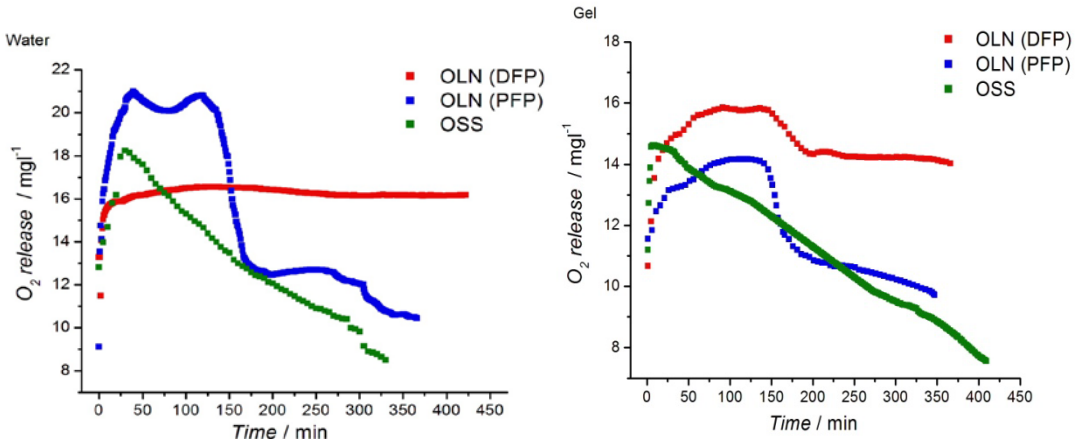

Figure 3.28. Chitosan OLND and OLNB oxygen release without US.

Results obtained for oxygen release without US using chitosan nanobubbles are quite similar to those obtained for dextran OLNs. Even in this case, OLNs also had a good oxygen-loading capacity. Both OLND and OLNB displayed a very good ability to deliver O_2 at high concentrations and for long times, either in water or gel formulations; nevertheless, DFP-containing OLNs appeared more effective than those with PFP. OSS did deliver high O_2 concentrations, but for shorter times than OLNs, as expected.

OXYGEN RELEASE WITH US AND TRESPASSING OF SKIN MEMBRANES

In figure 3.29 is shown the US abilities to induce sonophoresis and oxygen release from OLND and control HEC gel formulations. Sonophoresis is evaluated by using a home-made apparatus with two sealed cylindrical chambers (lower chamber: OLNDs, OFNDs, OLNBs, OFNBs or OSS; upper chamber: hypoxic solution) separated by a layer of pig ear skin. The oxygen-donor chamber (filled with OLND or control solutions) was connected to an US-transducer, whereas the oxygen-recipient chamber (filled with hypoxic solution) was connected to an oxymeter (see paragraph 2.7.6).

In our system, US might promote a cascade of events strongly impacting on the oxygen release kinetics. At first, US can induce bubble formation after acoustic droplet vaporization. Thereafter, bubble oscillations might lead to a stronger release mechanism due to cavitation. Finally, US might elicit sonoporation, temporarily enhancing skin leakage thus favoring transdermal drug release.

US improved the ability of both liquid and gel OLND formulations to cross the pig skin membrane and to release oxygen into the hypoxic chamber, being such oxygen release significantly larger than that from OFNDs, OLNBs, OFNBs, and OSS formulations. US

treatment (f = 2.5 MHz; P = 5 W) was performed for 5 min; thereafter, oxygen concentration in the hypoxic chamber was monitored every 5 min up to 135 min by Hach Langhe LDO oxymeter. Results are shown as means ± SD from three independent experiments. Data were also evaluated for significance by ANOVA. *Versus* OLND formulation: $p < 0.04$. Panel C. Sonophoresis and oxygen release from US-activated gel (2% HEC) formulations. Results are shown as means ± SD from three independent experiments. Data were also evaluated for significance by ANOVA. *Versus* OLND formulation: $p < 0.02$.

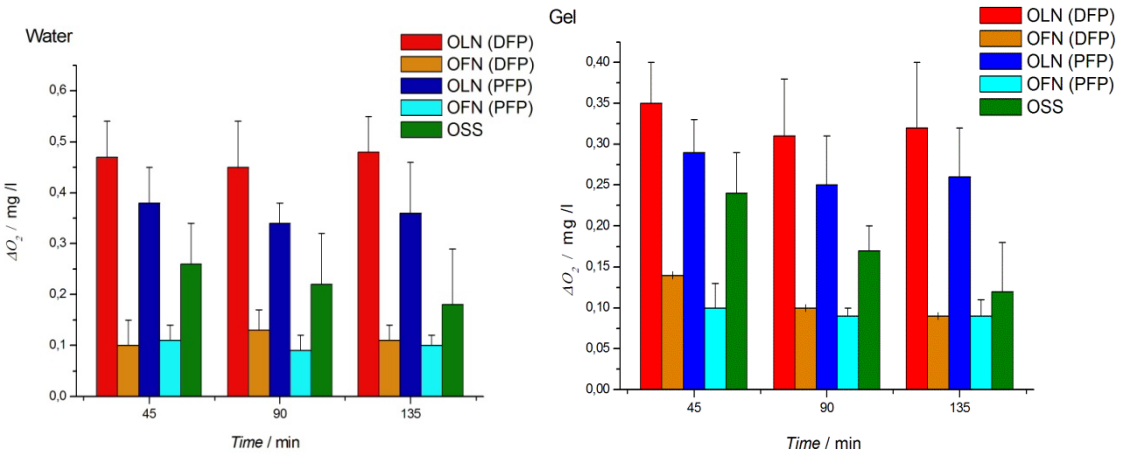

Figure 3.29. US-activated OLND oxygen release and sonophoresis through skin membranes *in vitro*.

US improved the ability of both liquid and gel OLND formulations to cross the pig skin membrane and to release oxygen into the hypoxic chamber, being such oxygen release significantly larger than that from OFNDs, OLNBs, OFNBs, and OSS formulations.

3.5.3 BIOCOMPATIBILITY ASSESSMENT

OLND toxicity was evaluated by testing *in vitro* cultures of human HaCaT keratinocytes, a cell line immortalized from a 62-year old Caucasian male donor. Human keratinocytes (10^6 cells/2 ml DMEM medium supplemented with 10% FCS) were left untreated or treated with different doses (100-400 µl) of OLNDs for 24 h in normoxia (20% O_2; white-squared curve) or hypoxia (1% O_2; black-squared curve). Thereafter, OLND cytotoxicity was measured through LDH assay (Panel A), and HaCaT cell viability by MTT assay (Panel B). Results are shown as means ± SEM from three independent experiments. Data were also evaluated for significance by Student's *t*

test. Panel A. *Versus* normoxic untreated cells: p not significant. Panel B. *Versus* normoxic untreated cells: * $p < 0.05$; ** $p < 0.01$; *** $p < 0.005$.

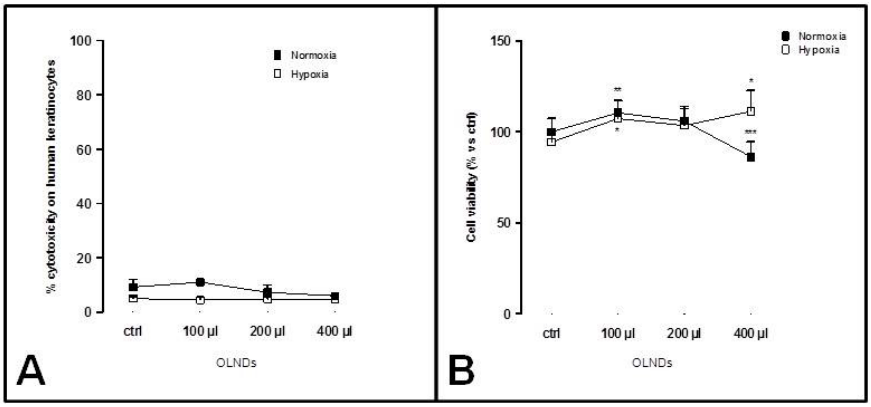

Figure 3.30. Lack of chitosan OLND toxicity on human keratinocytes.

As shown in Figure 3.30 (Panel 3.29A: LDH assay; Panel 3.29B: MTT assay), increasing volumes of OLND suspensions (100-400 µl/ 2 ml cell culture medium) were not toxic in normoxic conditions (20% O_2) and eventually improved keratinocyte viability in hypoxic conditions (1% O_2).

3.5.4 *IN VIVO* DETERMINATION OF OXYGEN RELEASE FROM OLNS

PHOTOACOUSTIC IMAGING

Shaved hind limbs of anaesthetized mice were monitored by photoacoustics for oxy-Hb and deoxy-Hb levels before (0 min, upper row), during (0-10 min, central row) and after (10 min, lower row) topical treatment with OSS (first column), OLND (second column) and OFND (fifth column) gel formulations. White/red pixels: oxy-Hb; blue pixels: deoxy-Hb. Data in figure 3.31 are shown as representative images from three independent experiments (three mice per experiment) with similar results.

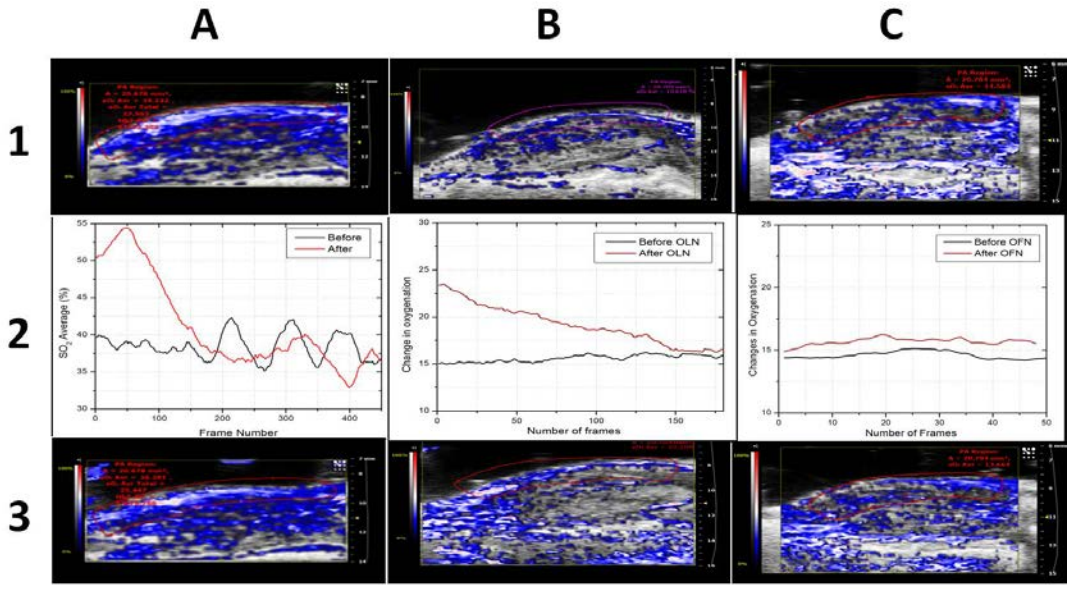

Figure 3.31. Topical treatment with OLND gel formulation partially enhances oxy-Hb levels *in vivo*.

As shown in Figure 3.31, *in vivo* experiments did not reproduce the promising results obtained *in vitro*. OLNDs did appear more effective than OSS, which induced a high but only transient peak in oxy-Hb, and OFNDs, which did not affect oxy-/deoxy-Hb balances at all. However, OLND-induced oxygenation gradually decreased throughout the overall observational period, and at the final time-point oxy-Hb levels were similar to those observed before starting treatment.

MEASUREMENT OF *TcpO$_2$* WITH US

Shaved abdomens of anaesthetized mice were topically treated with OLND gel formulation and ultrasonicated for 30 sec using a home-made US equipment (f = 1 MHz; P = 5 W). Before and after treatment, *tcpO$_2$* was monitored every 5 min for 15 min through TINA TCM30 oxymeter. Data are shown as means ± SD of three mice. Results were also analyzed for statistical significance by Student's t test. Versus untreated mice: $p < 0.03$.

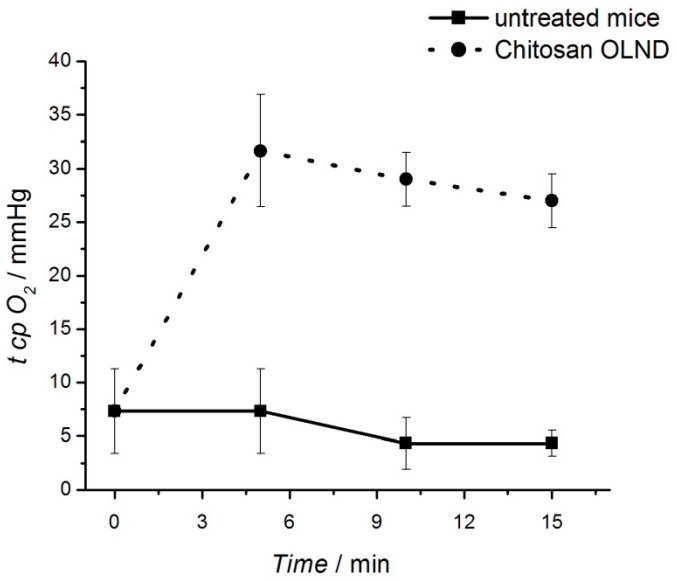

Figure 3.32. Topical treatment with US-activated OLNDs effectively enhances *tcpO₂ in vivo*.

As shown in figure 3.32, US promoted transdermal oxygen delivery in a time-sustained manner. Sonication appears therefore essential to induce oxygen release from OLNDs *in vivo*.

3.6 A COMBINED APPROACH: HIFU AND OLN

In this paragraph, a combined approach, regarding HIFU and OLN is provided. In particular, temperature increase induced by a focused ultrasound field (Transducer 3) in two different TMMs is studied. Two agar-based TMMs (described in paragraph 2.6.1) have been prepared. Before the gelling process is completed, 20 ml of dextran OLND are added to one of them. By means of a micro positioning system, the TMMs under study, including the optical fiber, are moved to reach the point of maximum revealed temperature, which is supposed to be the focus region of the ultrasound beam. Temperature data are acquired by means of a fiber optic hydrophone when the gel is subjected to a focused ultrasound field produced at three different values of power (50W, 75W, 100W). The exposure time is 5 s every measurement. Temperature values are calculated as the mean of five measures realized for each measurement condition. In graph 3.33 data obtained are shown.

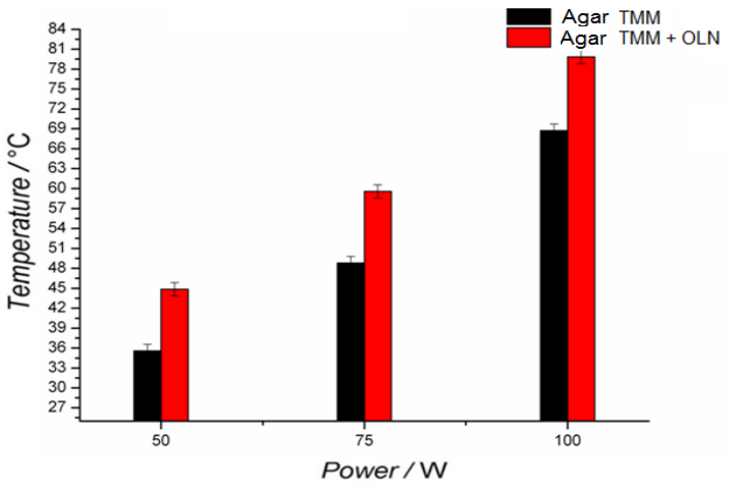

Figure 3.33. Temperature increment in an agar-based TMM (black bars) and in a TMM in which 20 ml of OLND are added to the solution (red bars).

As it is possible to see from the figure above, the temperature rise induced by an HIFU source in the TMM phantom without OLN (black bars) are lower than the temperature reached in a TMM in which 20 ml of OLN are added (red bars) in all the considered cases. The percentage of temperature increment using a TMM containing OLN is about 26% at 50 W, 22% at 75 W and 34% at 100 W. These experimental evidence are probably due to the fact that OLN may act as nuclei for cavitation inducing formation of shock waves and local temperature increase.

CHAPTER 4

CONCLUSIONS

This PhD thesis summarizes the results of three years activity devoted to the study of two different approaches for cancer treatment based on the use of ultrasound for therapeutic purpose. These two techniques regard the characterization of high intensity focused ultrasound (HIFU) and the synthesis, characterization and applications (both in vitro and in vivo) of oxygen loaded nanobubbles.

To whom concern the characterization of an HIFU field, the necessity of guidelines for a safe application of ultrasounds on patients is emerged and simulations of ultrasound field interactions with tissues are become fundamental. The activities conducted in this PhD aim to give some contribution in such a sense. The characterization of an ultrasound source has been provided measuring the total emitted power and a spatial description of the pressure field. Beside them, an accurate study of the temperature rise in the focus of an HIFU transducer has been performed using thermocouples and a fiber optic probe hydrophone. The latter instrument is an innovative hydrophone with a wide range of applications because it is free of errors due to viscous artifacts that afflict thermocouples and, most important advantage, is a completely compatible technique with magnetic resonance (MR) systems. Temperature measurements are necessary to understand the interaction between ultrasound beam and tissues and an accurate evaluation of temperature rise in the focus of an HIFU transducer has been performed in different tissue mimicking materials (TMM). TMM samples of agar and poliacrylamide gels have been realized and tested to study the heating effects induced by HIFU irradiation. Preliminary test on the accuracy of a fiber optic hydrophone conducted with a thermocouple reveal that temperature measurement are in good agree using this instrument. Thus, measurements on temperature rise induced by HIFU transducer using this sensors have been conducted, in particular, modifying the chemical composition of the gel in order to tuning its acoustic properties. It has been found that increasing the percentage of scattering and absorbing agents (kieselguhr) the temperature reached in the focus is lower, revealing that part of the energy of the ultrasonic beam has been absorbed by

wave interactions with inhomogeneities of the medium. After that, some studies on polyacrilamide gel have been performed in situ, using the USgFUS available at Istituto Oncologico Europeo (IEO) in Milan. Typical rising curves of temperature at different power outputs have been recovered. These are preliminary results obtained using an USgFUS system, further measurements in situ using a MRgFUS are planned. Due to the fact that the presence of permanent magnets within the structure of MR exclude the use of ferromagnetic devices (thermocouples), these coming measurement will be conducted using a fiber optic probe hydrophone. Successively, a new material has been developed and characterized as possible TMM to investigate the temperature rise induced by HIFU transducers: a reversible thermocromic silica gel. Preliminary measurements on temperature rise have been conducted with this material and it has been possible to analyze the heating effects caused by focused ultrasonic sources in function of power, frequency and irradiation time. All the begun activities would bring to a contribution in the development of a new concept of "dose" for ultrasonic treatment and in defining new instruments, methods and techniques for quality control assessment of medical ultrasonic devices and for a better guarantee for the safety of the patients treated with new generation devices.

The other research activity followed during my PhD has concerned the realization and characterization of oxygen load nanobubbles. While the use of nanobubbles as contrast agents has been around for a couple of decades, the development of nanobubbles for therapeutic purpose is still in its infancy. However, there is considerable interest in facilitating the transfer of drug, gene and other therapeutic compounds into diseased tissues and organs using ultrasound. In this regard, nanobubbles filled by oxygen represent an useful tool for the re-oxygenation of cancerous tissues. These tissues are characterized by oxygen deficiency, that is the main hallmark of cancerous solid tumors and a major factor limiting the effectiveness of radiotherapy. Thankfully, hypoxic regions are often located superficially; oxygen, properly encapsulated in suitable formulations of nanobubble solutions provided through ultrasonic transdermal sonophoresis, might help to counteract hypoxia effects. Oxygen-loaded nanobubbles (OLNs) that have been developed are constituted by a shell of biocompatible material (chitosan or dextran) and an oxygen-storing core, made of decafluoropentane (DFP) or perfluoropentane (PFP). OLNs have been manufactured both in liquid and gel formulations with the latter being more suitable for skin spreading. The behaviors of the different nanobbules preparation have been fully studied and compared looking for a further application to treat hypoxia-associated pathologies of superficial tissues. The two OLNs formulations has been characterized from a physical-chemical point of view, showing an average diameters lower than 1 μM, spherical shapes, and a good capacity of maintain their structure and small dimension over time. OLN sizes and stability are crucial properties in view of

their potential for *in vivo* administration. In addition to the proprieties listed above, it has been found that nanobubbles are surface-charged. This is an exquisitely propriety suitable for topical treatment, as surface charges enhance nanoparticle interaction with skin. However, transdermal oxygen delivery is normally limited by low skin permeability due to the stratum corneum, the outermost layer of the skin. To overcome this problem, ultrasound have been used to elicit sonophoresis, temporarily enhancing skin leakage thus favoring oxygen delivery. The first step to demonstrate the OLNs ability to across a skin membrane have been evaluated in vitro. The ability of OLNs to trespass the dermal layer has been monitored using a home-made apparatus developed during my work. Both liquid and gel OLNs behaviors has been studied. Once proven *in vitro* that OLNs were more effective than simple oxygen saturated solution (OSS) in releasing oxygen, without being toxic on human keratinocytes, and that gel formulation appeared suitable for treatment of skin membranes, OLND gel formulation was tested for oxygen delivery in vivo. In vivo, OLNs significantly increased transcutaneous capillary oxygenation in topically treated mice and, finally, oxygen release from OLNs have been studied in photoacoustic experiments. The skin oxygenation of anaesthetized mice topically treated with OLN, OFN (oxygen-free nanobubbles) or OSS gel formulations, was monitored by visualizing the subcutaneous levels of oxyhemoglobin (oxy-Hb) and deoxyhemoglobin (deoxy-Hb) through photoacoustic imaging. All these experiments have confirmed that topical administration of exogenous O_2, properly encapsulated in nanobubble formulations, might be a new suitable and efficient approach to treat hypoxic tissues, cancerous or affected by other disease. Future preclinical and clinical studies will be certainly investigated, as OLN application appears of great interest for transdermal oxygen delivery.

The activities conducted during my PhD, concerning HIFU field characterization and the development of oxygen nanocarriers, can be considered preliminary (but necessary) results for further experiments that merge these two techniques in a new and non invasive therapeutic modality. Indeed, the application of focused ultrasound might promote transdermal oxygen delivery and destroy cancerous tissues while, in the same time, nanobubbles in gel formulation might counteract hypoxia effects in several pathologies of different etiology (cancer, autoimmunity, infection etc) by improving oxygen delivery to hypoxic tissues.

BIBLIOGRAFY

[1] F.P. Curra, L. Crum, Therapeutic ultrasound: surgery and drug delivery. Acoustic Science and Technology 2003;24, 6

[2] Frenkel, V. Ultrasound mediated delivery of drugs and genes to solid tumors. Advanced Drug Delivery Reviews, 2008; 60(10), 1193-1208.

[3] von Eschenbach, A. C. A vision for the national cancer program in the united states. Nature Reviews.Cancer, 2004; 4(10), 820-828.

[4] Alongi F., Russo G., Spinelli A., Borasi G., Scorsetti M., Gilardi M. C., et al. Can magnetic resonance image-guided focused ultrasound surgery replace local oncology treatments? A review. Tumori, 2011; 97(3), 259.

[5] ter Haar, G.. High intensity focused ultrasound for the treatment of tumors. Echocardiography (Mount Kisco, N.Y.), 2001 18(4), 317-322.

[6] Kennedy, J. E. High-intensity focused ultrasound in the treatment of solid tumours. Nature Reviews Cancer, 5(4), 2005; 321-327.

[7] James J. Kwan, Mehmet Kaya, Mark A. Borden and Paul A. Dayton. Theranostic Oxygen Delivery Using Ultrasound and Microbubbles. Theranostics, 2012; 2(12):1174-1184

[8] E Stride* and N Saffari. Microbubble ultrasound contrast agents: a review. Proc. Instn Mech. Engrs (2003) Vol. 217 Part H: J. Engineering in Medicine.

[9] S. Mitragotri. Healing sound: the use of ultrasound in drug delivery and other therapeutic applications. Nature Reviews 2005;Vol. 4 March.

[10] Maylia E, Nokes LD. The use of ultrasonics in orthopaedics—a review. Technol Health Care.; 1999; 7:1-28.

[11] Ziskin MC, Rapacholi MH, Grandolfo M, Rindi A. Applications of ultrasound in medicine comparison with other modalities. Ultrasound: medical applications, biological effects, and hazard potential. New York: Plenum Press; 1987; p 49-59.

[12] Dyson M. Therapeutic applications of ultrasound. New York: Churchill Livingstone; 1985, p 121-33.

[13] Nyborg WL, Ziskin MC. Biological effects of ultrasound. New York: Churchill Livingstone; 1985, p 157-67.

[14] Kaufman JJ, Einhorn TA. Ultrasound assessment of bone. J Bone Miner Res.; 1993; 8:517-25.

[15] Moed BR, Kim EC, van Holsbeeck M, Schaffler MB, Subramanian S, Bouffard JA, Craig JG. Ultrasound for the early diagnosis of tibial fracture healing after static interlocked nailing without reaming: histologic correlation using a canine model. J Orthop Trauma.; 1998,12:200-5.

[16] St John Brown R. How safe is diagnostic ultrasonography? J Can Med Assoc.; 1984, 131:307-11.

[17] Bamber J, ter Haar GR, Hill C. Physical Principles of medical Ultrasound. 2nd ed. London: Wiley; (2004).

[18] Humphrey, V. F.. Ultrasound and matter--physical interactions. Progress in Biophysics and Molecular Biology, 93(1-3), 195-211(2007)

[19] Sapareto, S. A., & Dewey, W. C. Thermal dose determination in cancer therapy. International Journal of Radiation Oncology, Biology, Physics, 1985, 10(6), 787.

[20] Wu, J., & Nyborg, W. L.. Ultrasound, cavitation bubbles and their interaction with cells. Advanced Drug Delivery Reviews, 2008, 60(10), 1103-1116.

[21] Hill, C. R., & ter Haar, G. R.. Review article: High intensity focused ultrasound-potential for cancer treatment. The British Journal of Radiology, 1995, 68(816), 1296.

[22] Frenkel,V. Editor: “Therapeutic Ultrasound: Mechanisms to Applications”. Nova Science Publishers, Inc. Hauppauege, NY. (2011).

[23] Young F. Cavitation. New York:McGraw-Hill. (1989).

[24] Leighton, T. G. The acoustic bubble. The Journal of the Acoustical Society of America, 1994, 96(4), 2616.

[25] Flynn, H.G. Physics of acoustic cavitation in liquids. In Physical Acoustics, ed. WP Mason, vol. 1B, chapter 9. New York: Academic, 1964.

[26] E. Quaia, Physical basis and principles of action of microbubble-based contrast agents. Contrast Media in Ultrasonography, 2005.

[27] K. Ferrara, R. Pollard, M. Borden, Ultrasound microbubble contrast agents: fundamentals and application to gene and drug delivery, Annu. Rev. Biomed. Eng. 20007, 9 415–447

[28] V. Sboros, Response of contrast agents to ultrasound, Adv. Drug Deliv. Rev. 60 2008 1117–1136.

[29] E. VanBavel, Effects of shear stress on endothelial cells: possible relevance for ultrasound applications, Prog. Biophys. Mol. Biol.2007, 93 374–383

[30] P.F. Davies. Flow-mediated endothelial mechanotransduction. Physiol. 1995, Rev. 75, 519.

[31] M. Postema, A. vanWamel, C. Lancée, N. de Jong, Ultrasound-induced encapsulated microbubble phenomena. Ultrasound Med. Biol. 30, 2004, 827–840.

[32] M. Postema, A. vanWamel, F. ten Cate, N. de Jong, High-speed photography during ultrasound illustrates potential therapeutic applications of microbubbles, Med. Phys. 32, 2005 3707–3711.

[33] T.g. Leighton, What is ultrasound? Prog. Biophys. Mol. Biol. 2007, 93.

[34] Flynn, H. G.. Generation of transient cavities in liquids by microsecond pulses of ultrasound. The Journal of the Acoustical Society of America, 1982, 72(6), 1926 – 1932.

[35] Delius, M., Denk, R., Berding, C., Liebich, H. G., Jordan, M., & Brendel, W. Biological effects of shock waves: Cavitation by shock waves in piglet liver. Ultrasound in Medicine & Biology, 1990, 16(5), 467-472.

[36] Bailey, M. R., Blackstock, D. T., Cleveland, R. O., & Crum, L. A.. Comparison of electrohydraulic lithotripters with rigid and pressure- release ellipsoidal reflectors. II. Journal of the Acoustical Society of America, 1999,106(2), 1149-1160

[37] Apfel, R. E., & Holland, C. K. Gauging the likelihood of cavitation from short-pulse, lowduty cycle diagnostic ultrasound. Ultrasound in Medicine & Biology, 1991, 17(2), 179-185.

[38] Frenkel, V., & Li, K. C. P. Potential role of pulsed-high intensity focused ultrasound in gene therapy. Future Oncology (London, England), 2006, 2(1), 111-119.

[39] Warden, S. J., Fuchs, R. K., Kessler, C. K., Avin, K. G., Cardinal, R. E., & Stewart, R. L. Ultrasound produced by a conventional therapeutic ultrasound unit accelerates fracture repair. Physical Therapy, 2006, 86(8), 1118.

[40] Mitragotri, S. Healing sound: The use of ultrasound in drug delivery and other therapeutic applications. Nature Reviews.Drug Discovery, 2005 4(3), 255-260.

[41] Wood, R. W., & Loomis, A. L.. The physical and biological effects of high-frequency soundwaves of great intensity. (phil. mag., sept., 1927). Journal of the Franklin Institute, 1928 205(1), 151- 153.

[42] Dubinsky, T. J., Cuevas, C., Dighe, M. K., Kolokythas, O., & Hwang, J. H.. High-intensity focused ultrasound: Current potential and oncologic applications. AJR.American Journal of Roentgenology, 2008;190(1), 191-199.

[43] Lynn JG, Zwemer RL, Chick AJ, Miller AE. A new method for the generation and use of focused ultrasound in experimental biology. J Gen Physiol 1942;26:179–192.

[44] Ballantine HT, Bell E, Manlapaz J. Progress and problems in the neurological applications of focused ultrasound. J Neurosurg 1960;17:858–876.

[45] WJ, Fry FJ. Fundamental neurological research andmhuman neurosurgery using intense ultrasound. IRE Trans Biomed Electronics 1960;ME-7:166–181.

[46] Lynn JG, Putnam TJ. Histological and cerebral lesions prodcued by focused ultrasound. Am J Pathol 1944;20:637–649.

[47] Wall P.D, Fry WJ, Stephens R, Tucker D, Lettvin JY. Changes produced in the central nervous system by ultrasound. Science 1951;114:686–687.

[48] Bakay L, Hueter TF, Ballantine HT, Sosa D. Ultrasonically induced changes in the blood brain barrier. A M A Arch Neuro Psychiatr 1956;00:457–467.

[49] Fry WJ, Barnard JW, Fry FJ, Krumins RF, Brennan JF. Ultrasonic lesions in the mammalian central nervous system. Science 1955;122:517–518.

[50] Fry FJ, Kossoff G, Eggleton RC, Dunn F. Threshold ultrasound dosages for structural changes in the mammalian brain. J Acoust Soc Am 1970;48:1413–1417.

[51] Aubry JF, Tanter M, Pernot M, Thomas JL, Fink M. Experimental demonstration of noninvasive transskull adaptive focusing based on prior computed tomography scans. J Acoust Soc Am 2003;113:84–93.

[52] Clement GT, White J, Hynynen K. Investigation of a largearea phased array for focused ultrasound surgery through the skull. Phys Med Biol 2000;45:1071–1083.

[53] Lavine O, Langenstrass K, Bowyer C, Fox F, Griffing V, Thaler W. Effects of ultrasonic waves on the refractive media of the eye. Arch Ophthalmol 1952;47:204–209.

[54] Rosenberg RS, Purnell E. Effects of ultrasonic radiation on the ciliary body. Am J Ophthalmol 1967;63:403–409.

[55] Coleman DJ, Lizzi FL, El-Mofty AAM, Driller J, Franzen LA. Ultrasonically accelerated absorption of vitreous membranes. Am J Ophthalmol 1980;89:490–499.

[56] Coleman DJ, Lizzi FL, Torpey JH, Burgess SEP, Driller J, Rosado AL, et al. Treatment of experimental lens capsular tears with intense focused ultrasound. Br J Ophthalmol 1985;69:645–649.

[57] Silverman RH, Vogelsang B, Rondeau MJ, Coleman DJ. Therapeutic ultrasound for the treatment of glaucoma. Am JmOphthalmol 1991;111:327–337.

[58] Burgess SEP, Iwamoto T, Coleman DJ, Lizzi FL, Driller J, Rosado AL. Histological changes in porcine eyes treated with high intensity focused ultrasound. Ann Ophthalmol 1987;19:133–138.

[59] Lizzi FL, Coleman DJ, Driller J, Ostromogilsky M, Chang S, Grenall P. Ultrasonic hyperthermia for ophthalmic therapy. IEEE Trans Son Ultrason 1984;SU-31:473–481.

[60] Dewhirst MW, Viglianti BL, Lora-Michiels M, Hanson M, Hoopes PJ. Basic principles of thermal dosimetry and thermal thresholds for tissue damage from hyperthermia. Int J Hyperther 2003; 19:267–294.

[61] Fosse E. Thermal ablation of benign and malignant tumours. Minim Invasive Ther Allied Technol 2006;15:2–3.

[62] Shibata T, Niinobu T, Ogata N. Comparison of the effects of in-vivo thermal ablation of pig liver by microwave and radiofrequency coagulation. J Hepatobiliary Pancreat Surg 2000;7:592–598.

[63] ter Haar GR, Robertson D. Tissue destruction with focused ultrasound in vivo. Eur Urol 1993;23(Suppl. 1):8–11.

[64] Ishikawa T, Okai T, Sasaki K, Umemura S, Fujiwara R, Kushima M, Ichihara M, Ichizuha K. Functional and histological changes in rat femoral arteries by HIFU exposure.Ultrasound Med Biol 2003;29:1471–1477.

[65] O'Neil, H. T. (1949). Theory of focusing radiators. The Journal of the Acoustical Society of America, 21(5), 516.

[66] Wu J, Nyborg WL Ultrasound, cavitation bubbles and their interaction with cells. Adv Drug Deliv Rev. 2008 Jun 30;60(10):1103-16.

[67] ter Haar, G. High intensity focused ultrasound for the treatment of tumors. Acoustic surgery. Physics Today, 2001; 54(12), 29.

[68] Ter Haar, G. Ultrasound focal beam surgery. Ultrasound in Medicine & Biology, 1995;21(9), 1089-1100.

[69] Ter Haar, G., Coussios C., High intensity focused ultrasound: Physical principles and devices. Int. J. Hyperthermia, March 2007; 23(2): 89–104

[70] Ter Haar GR, Robertson D. Tissue destruction with focused ultrasound in vivo. Eur Urol 1993;23(Suppl. 1):8–11.

[71] ter Haar, G. Therapeutic applications of ultrasound. Progress in Biophysics and Molecular Biology, 2007; 93(1-3), 111-129

[72] Ter, Haar, G., Clarke, R. L., Vaughan, M. G., & Hill, C. R. Trackless surgery using focused ultrasound: Technique and case report. Minimally Invasive Therapy & Allied Technologies, 1991, 1(1), 13-19.

[73] Hynynen, K. The threshold for thermally significant cavitation in dog's thigh muscle in vivo. Ultrasound in Medicine & Biology, 199117(2), 157-169.

[74] Brujan, E. A., Ikeda, T., & Matsumoto. Jet formation and shock wave emission during collapse of ultrasound-induced cavitation bubbles and their role in the therapeutic applications of high-intensity focused ultrasound. Physics in Medicine and Biology, 2005; 50(20), 4797-4809.

[75] Tran, B. C., Jongbum Seo, Hall, T. L., Fowlkes, J. B., & Cain, C. A. Microbubble-enhanced cavitation for noninvasive ultrasound surgery, 2003; 50(10) 1296-1304.

[76] Sokka, S. D., King, R., & Hynynen, K. MRI-guided gas bubble enhanced ultrasound heating in in vivo rabbit thigh. Physics in Medicine and Biology, 2003; 48(2), 223-241.

[77] McDannold, N., Vykhodtseva, N., & Hynynen, K. Targeted disruption of the blood-brain barrier with focused ultrasound: Association with cavitation activity. Physics in Medicine and Biology, 2006; 51(4), 793-807.

[78] Rivens I, Shaw A, Civale J, Morris M. Treatment Monitoring & Thermometryfor Therapeutic Focused Ultrasound. Int J Hyperther 2007,

[79] Vaezy S, Zderic V. Haemorrhage control using high intensity focused ultrasound. Int J Hyperther, 2007.

[80] Fry FJ. Precision high intensity focused ultrasonic machines for surgery. Am J Phys Med 1958; 37:152–156.

[81] Chapelon JY, Cathignol D, Cain C, Ebbini E, Kluiwstra JU, Sapozhnikov OA, Fleury G, Berriet R, Chupin L, Guey JL. New piezoelectric transducers for therapeutic ultrasound. Ultrasound Med Biol 2000;26:153–159.

[82] Wan H, Vanbaren P, Ebbini ES, Cain CA. Ultrasound surgery – comparison of strategies using phased-array systems. IEEE Trans Ultrason Ferroelectr Freq Cont 1996; 43:1085–1098.

[83] Visioli, A. G., Rivens, I. H., ter Haar, G. R., Horwich, A., Huddart, R. A., Moskovic, E., et al.. Preliminary results of a phase I dose escalation clinical trial using focused ultrasound in the treatment of localised tumours. European Journal of Ultrasound : Official Journal of the European Federation of Societies for Ultrasound in Medicine and Biology, 1999; 9(1), 11-18.

[84] Vallancien, G., Harouni, M., Guillonneau, B., Veillon, B., & Bougaran, J. Ablation of superficial bladder tumors with focused extracorporeal pyrotherapy. Urology, 1996, 47(2), 204-207.

[85] Bohris C, Schreiber WG, Jenne J, Simiantonakis I, Rastert R, Zabel HJ, Huber P, Bader R, Brix G. (). Quantitative MR temperature monitoring of high-intensity focused ultrasound therapy. Magn Reson Imaging. 1999 May; 1999, 17(4):603-10

[86] Kallel F. The feasibility of elastograohic visualization oh HIFU induced thermal lesion in soft tissues. Ultrasound in Med. & Biol., 1999; Vol. 25, No. 4, pp. 641–647.

[87] Sheng Li1, and Pei-Hong Wu1. Magnetic resonance image-guided versus ultrasound-guided high-intensity focused ultrasound in the treatment of breast cancer. Chin J Cancer. 2013; 32(8): 441–452.

[88] Curiel, L., Souchon, R., Rouvie` re, O., Gelet, A., Chapelon, J.Y.. Elastography for the follow-up of high-intensity focused ultrasound prostate cancer treatment: initial comparison with MRI. Ultrasound Med. Biol. 2005; 31, 1461–1468.

[89] Bailey, M.R., Couret, L.N., Sapozhnikov, O.A., Khokhlova, V.A., ter Haar, G.R., Vaezy, S., Shi, X., Martin, R., Crum, L.A.,. Use of overpressure to assess the role of bubbles in focused ultrasound lesion shape in vitro. Ultrasound Med. Biol. 2001; 27, 695–708.

[90] Vallancien, G., Harouni, M., Guillonneau, B., Veillon, B., Bougaran, J.,. Ablation of superficial bladder tumors with focused extracorporeal pyrotherapy. Urology 1996; 47, 204–207.

[91] Wu, F., Wang, Z., Chen, W., et al., Extracorporeal high intensity focused ultrasound ablation in the treatment of patients with large hepatocellular carcinoma. Ann. Surg. Oncol. 2004, 11, 1061–1069.

[92] Gianfelice, D., Khiat, A., Amara, M., et al.. MR image guided focused ultrasound ablation of breast cancer: histological assessment of effectiveness—initial experience. Radiology 2003; 227, 849–855.

[93] Kennedy, J.E., ter Haar, G.R., Cranston, D.,. High intensity ultrasound: surgery of the future? Br. J. Radiol. 76, 2003; 590–599.

[94] Kennedy, J.E:. High intensity focused ultrasound in the treatment of solid tumours. Nat. Rev. Cancer 2005; 18, 321–327.

[95] Kennedy, J.E., Wu, F., ter Haar, G.R., et al., High intensity focused ultrasound for the treatment of liver tumours. Ultrasonics 2004, 42, 931–935.

[96] Watkin, N.A., ter Haar, G.R., Morris, S.B., Woodhouse, C.R.J.,. The urological applications of focused ultrasound surgery. Brit. J. Urol. 1995; 75 (Suppl 1).

[97] Tu, G., Qiao, T., He, S., et al.,. An experimental study on high-intensity focused ultrasound in the treatment of VX2 rabbit kidney tumours. Chin. J. Urol. 20, 1999; 456–458.

[98] Chapelon, J.Y., Margonari, J., Theille` re, Y., Gorry, F., Vernier, F., Blanc, E., Gelet, A.,. Effects of high energy focused ultrasound on kidney tissue in the rat and the dog. Eur. Urol. 1992; 22, 147–152.

[99] Marberger, M., Schatzl, G., Cranston, D., Kennedy, J.E.,. Extra-corporeal ablation of renal tumours with high intensity focused ultrasound. BJU 2005; Int. 95 (Suppl. 2), 52–55.

[100] Wu, F., Wang, Z., Chen, W., Bai, J., Zhu, H., & Qiao, T. Preliminary experience using high intensity focused ultrasound for the treatment of patients with advanced stage renal malignancy. The Journal of Urology, 2003; 170 (6 Pt 1), 2237-2240.

[101] Illing, R.O., Kennedy, J.E., Wu, F., et al. The safety and feasibility of extracorporeal high intensity focused ultrasound (HIFU) for the treatment of liver and kidney tumours in the Western population. Br. J. Cancer 2005; 93, 890–895.

[102] Wu, F., Wang, Z., Chen, W., et al., 2004b. Extracorporeal high intensity focused ultrasound surgery for the treatment of human solid carcinomas: early Chinese clinical experience. Ultrasound Med. Biol. 30, 245–260.

[103] Vaezy, S., Fujimoto, V.Y., Walker, C., Martin, R.W., Chi, E.Y., Crum, L.A., Treatment of uterine fibroid tumour in a nude mouse model using high-intensity focused ultrasound. Am. J. Obstet. Gynecol. 2000; 183, 6–11.

[104] Tempany, C.M., Stewart, E.A., McDannold, N., 2003. High intensity focused ultrasound surgery of uterine leiomyomas: a feasibility study. Radiology 226, 897–905.

[105] Li, C., Bian, D., Chen, W., et al.,. Focused ultrasound therapy of vulvar dystrophies: a feasibility study. Obstet. Gynecol. 2004; 104, 915–921.

[106] Clement, G.T., White, J., Hynynen, K., Investigation of a large-area phased array for focused ultrasound surgery through the skull. Phys. Med. Biol. 2000; 45, 1071–1083.

[107] Hynynen, K., Jolesz, F.A.,. Demonstration of potential non-invasive ultrasound brain therapy through the intact skull. Ultrasound Med. Biol. 1998, 24, 275–283.

[108] Yu, T., Wang, G., Hu, K., Ma, P., Bai, J., Wang, Z., b. A microbubble agent improves the therapeutic efficiency of high intensity focused ultrasound: a rabbit kidney study. Urol. Res. 2004; 32, 14–19.

[109] Oosterhof, G. O. N., Cornel, E. B., Smits, G. A. H. J., Debruyne, F. M. J., & Schalken. Influence of high-intensity focused ultrasound on the development of metastases. European Urology, 1997; 32(1), 91-95.

[110] Wu, F., Wang, Z., Lu, P., et al., Activated anti-tumour immunity in cancer patients after high intensity focused ultrasound ablation. Ultrasound Med. Biol. 2004; 30, 1217–1222.

[111] Sanghvi NT, Fry FJ, Bihrle R, Foster RS, Phillips MH, Syrus J, Zaitsev AV, Hennige CW. Noninvasive surgery of prostate tissue by high-intensity focused ultrasound. IEEE Trans Ultrason Ferr 1996;43:1099–1110.

[112] Sanghvi NT, Fry FJ, Bihrle R, Foster RS, Phillips MH, Syrus J, Zaitsev AV, Hennige CW. Noninvasive surgery of prostate tissue by high-intensity focused ultrasound. IEEE Trans Ultrason Ferr 1996;43:1099–1110.

[113] Leslie TA, Kennedy JE. High-intensity focused ultrasound principles, current uses, and potential for the future. Ultrasound Q 2006;22: 263–272.

[114] Madersbacher, S., Kratzik, C., Susani, M., Marberger, M., Foster, R. S., Bihrle, R., et al.Tissue ablation in benign prostatic hyperplasia with high intensity focused ultrasound. Journal of Urology, 1994; 152(6 I), 1956-1961.

[115] Chaussy, C., & Thuroff, S., High-intensity focused ultrasound in prostate cancer: Results after 3 years. Molecular Urology, 2000; 4(3), 179-182.

[116] Lafon C, Chapelon JY, Prat F, Gorry F, Margonari J, Theillere Y, Cathignol D. Design and preliminary results of an ultrasound applicator for interstitial thermal coagulation. Ultrasound Med Biol 1998;24:113–122. High intensity focussed ultrasound 103

[117] Prat F, Lafon C, Margonari J, Gorry F, Theillere Y, Chapelon JY, Cathignol D. A high-intensity US probe designed for intraductal tumor destruction: Experimental results. Gastrointest Endosc 1999;50:388–392.

[118] Prat F, Lafon C, Melodelima D, Theillere J-Y, Fritsch J, Pelletier G, Buffet C, Cathignol D. Endoscopic treatment of cholangiocarcinoma and carcinoma of the duodenal papilla by intraductal high-intensity US: Results of a pilot study. Gastrointest Endosc 2002;56:909–915.

[119] Prat F, Lafon C, Theillere J-Y, Fritsch J, Choury A-D, Lorand I, Cathignol D. Destruction of bile duct carcinoma by intraductal high intensity ultrasound during ERCP. Gastrointest Endosc 2001;53:797–800.

[120] Melodelima D, Salomir R, Mougenot C, Moonen C, Cathignon D. In vivo experiments with intraluminal ultrasound applicator compatible with ‘‘real-time’’ MR temperature mapping, designed for oesophagus tumour ablation. 2005;Proc ISTU4 AIP 185–187.

[121] Melodelima D, Salomir R, Chapelon JY, re Y, Moonen C,Cathignol D. Intraluminal high intensity ultrasound treatment in the esophagus under fast MR temperature mapping: In vivo studies. Magn Reson Med 2005;54:975–982.

[122] Makin I, Faikin W, Mast D, Runk M, Slayton M, Barthe P Conformal bulk ablation and therapy monitoring using intracorporeal image-Treat Ultrasound Arrays. Proc ISTU4AIP 2005;27–29.

[123] Murat F, Lafon C, Gelet A, Martin X, Cathignol D Bloodless partial nephrectomy through application of nonfocused high-intensity ultrasound. Proc ISTU4 AIP 2005;181–184.

[124] http://www.fusfoundation.org/

[125] http://www.cfef.org/

[126] British Journal of Cancer (2005) 93, 890–895. doi:10.1038/sj.bjc.6602803 http://www.nature.com/bjc/journal/v93/n8/full/6602803a.html

[127] American Heart Association, Inc. Circulation. First Human Experience With Pulmonary Vein Isolation Using a Through-the-Balloon Circumferential Ultrasound Ablation System for Recurrent Atrial Fibrillation ;2000;102/16/1879

[128] World Federation for Ultrasound in Medicine & Biology. Volume 31, Issue 11, Pages 1527-1537; 2005 http://www.umbjournal.org/article/

[129] ter Haar, G., Rivens, I., Chen, L., & Riddler, S. (). High intensity focused ultrasound for the treatment of rat tumours. Physics in Medicine and Biology, 1991; 36(11), 1495.

[130] Vaughan, M. G., ter Haar, G. R., Hill, C. R., Clarke, R. L., & Hopewell, J. W. Minimally invasive cancer surgery using focused ultrasound: A pre-clinical, normal tissue study. The British Journal of Radiology, 1994 67(795), 267.

[131] Kennedy, J. E., Wu, F., ter Haar, G. R., Gleeson, F. V., Phillips, R. R., Middleton, M. R., et al. High-intensity focused ultrasound for the treatment of liver tumours. Ultrasonics, 2004; 42(1-9), 931- 935.

[132] Gelet, A., Chapelon, J. Y., Bouvier, R., Pangaud, C., & Lasne, Y. Local control of prostate cancer by transrectal high intensity focused ultrasound therapy: Preliminary results. The Journal of Urology, 1999; 161(1), 156-162.

[133] Clement, G. T. Perspectives in clinical uses of high-intensity focused ultrasound. Ultrasonics, 2004 42(10), 1087.

[134] Zhi B. Wang, Feng Wu, Zhi L. Wang, & Chuan Liu. Concept of biological focal field and its importance in tissue resection with high intensity focused

ultrasound. The Journal of the Acoustical Society of America, 1998;103(5), 2869.

[135] Melodelima, D., Chapelon, J. Y., Theillère, Y., & Cathignol, D. (). Combination of thermal and cavitation effects to generate deep lesions with an endocavitary applicator using a plane transducer: Ex vivo studies. Ultrasound in Medicine & Biology, 2004; 30(1), 103-111.

[136] Poliachik, S. L., Chandler, W. L., Mourad, P. D., Bailey, M. R., Bloch, S., Cleveland, R. O., et al. Effect of high-intensity focused ultrasound on whole blood with and without microbubble contrast agent. Ultrasound in Medicine & Biology, 1999; 25(6), 991-998.

[137] Kessel, D., Jeffers, R., Fowlkes, J. B., & Cain, C. Porphyrin-induced enhancement of ultrasound cytotoxicity. International Journal of Radiation Biology, 1994; 66(2), 221-228.

[138] Katherine W. Ferrara Driving delivery vehicles with ultrasound. Advanced Drug Delivery Reviews 60 2008; 1097–1102

[139] Liu Y, Miyoshi H, Nakamura M Encapsulated ultrasound microbubbles: therapeutic application in drug/gene delivery. J Control Release. 2006;114(1):89-99. Epub 2006 May 27.

[140] Evan C. Unger *, Terry Onichi Matsunaga, Thomas McCreery, Patricia Schumann, Robert Sweitzer, Rachel Quigley. Therapeutic applications of microbubbles. European Journal of Radiology 42, 2002; 160–168.

[141] Wilson SR, Burns PN. Microbubble-enhanced US in body imaging: what role? Radiology. 2010;257(1):24–39.

[142] Deshpande N, Needles A, Willmann JK. Molecular ultrasound imaging: current status and future directions. Clin Radiol. 2010;65(7): 567–581.

[143] Danila M, Popescu A, Sirli R, Sporea I, Martie A, Sendroiu M. Contrast enhanced ultrasound (CEUS) in the evaluation of liver metastases. Med Ultrason. 2010;12(3):233–237.

[144] Lindner, J.R., Song, J., Sklenar, J., Kaul, S.,. Microvascular rheology of Defin-ity microbubbles after intra-arterial and intravenous administration. J. Am. Soc.Echocardiogr. 15, 2002; 396–403.

[145] Suzuki, R., Oda, Y., Utoguchi, N., Maruyama, K.,. Progress in the development ofultrasound-mediated gene delivery systems utilizing nano- and microbubbles.J. Control. Rel. 149, 2011; 36–41.

[146] Deckers, R., Moonen, C.T., Ultrasound triggered, image guided, local drug deliv-ery. J. Control. Rel. 2010; 148, 25–33.

[147] Crum, L. A., Roy, R. A., Dinno, M. A., Church, C. C., Apfel, R. E., Holland, C. K., et al.. Acoustic cavitation produced by microsecond pulses of ultrasound: A discussion of some selected results. Journal of the Acoustical Society of America, 91(2), 1992; 1113-1119.

[148] Schutt, E.G., Klein, D.H., Mattrey, R.M., Riess, J.G.. Injectable microbubbles ascontrast agents for diagnostic ultrasound imaging: the key role of perfluoro-chemicals. Angew. Chem. Int. Ed. 2003; 42, 3218–3235.

[149] Roberta Cavalli, Agnese Bisazza, David Lembo. Micro- and nanobubbles: A versatile non-viral platform for gene delivery. International Journal of Pharmaceutics, 2013.

[150] Takahashi, M.,. Base and technological application of micro-bubble and nanobubble. Mater. Integration 2009; 22, 2–19.

[151] Takahashi, M., Chiba, K., Li, P., Free-radical generation from collapsing microbubbles in the absence of a dynamic stimulus. J. Phys. Chem. B 2007; 111, 1343–1347.

[152] Delalande, A., Postema, M., Mignet, N., Midoux, p., Pinchon, C.,. Ultrasound andmicrobubbles-assisted gene delivery: recent advances and ongoing challenges.Ther. Del. 3, 2012; 1199–1215.

[153] Kwan, J.J., Borden, M.A.. Lipid monolayer collapse and microbubble stability. Adv. Colloids Interface Sci. 2012; 183–184, 82–99.

[154] Kim, J.Y., Song, M.G., Kim, J.D.,. Zeta potential of nanobubbles generated by ultrasonication in aqueous alkyl polyglycoside solutions. J. Colloid Interface Sci. 2000223, 285–291.

[155] Borden, Ma, Cruse, D.E., Caskey, C.E., Zhao, S.K., Dayton, P.A., Ferrara, K.W., 2005.Influence of lipid shell: physic-chemical properties on ultrasound-inducedmicrobubble destruction. IEEE Trans. Ultrason. Ferroelectr. Freq. Control,1992–2002.

[156] Borden, M., Little, E., Gillies, R., Ferrara, K.. DNA and polylysine adsorption andmultilayer construction onto cationic lipid-coated microbubbles. Langmuir 2007; 23,9401–9408.

[157] Cavalli, R., Bisazza, A., Rolfo, A., Balbis, S., Madonnaripa, D., Caniggia, I., Guiot, C.,. Ultrasound-mediated oxygen delivery from chitosan nanobubbles. Int. J.Pharm. 378, 2009; 215–217.

[158] Delalande, A., Postema, M., Mignet, N., Midoux, p., Pinchon, C., 2012. Ultrasound andmicrobubbles-assisted gene delivery: recent advances and ongoing challenges.Ther. Del. 3, 1199–1215.

[159] Leong-Poi, H., Song, J., Rim, S.J., Christiansen, J., Kaul, S., Lindner, J.R.,. Influ-ence of microbubble shell properties on ultrasound signal: implications

forlow-power perfusion imaging. J. Am. Soc. Echocardiogr. 15, 2002; 1269–1276.

[160] P.A. Dijkmansa, L.J.M. Juffermansa,b, R.J.P. Mustersb, A. van Wamelc, F.J. ten Catec, W. van Gilstd, C.A. Vissera, N. de Jongc, O. Kamp. Microbubbles and ultrasound: from diagnosis to therapy. Eur J Echocardiography, 2004 5, 245-256

[161] Fechheimer, M., Boylan, J.F., Parker, S., Sisken, J.E., Patel, G.L., Zimmer, S.G.,.Transfection of mammalian cells with plasmid DNA by scrape loading and son-ication loading. Proc. Natl. Acad. Sci. U. S. A. 1987; 84, 8463–8467.

[162] Miller, D.L., Quddus, J. Lysis and sonoporation of epidermoid and phagocyticmonolayer cells by diagnostic ultrasound activation of contrast agent gas bodies. Ultrasound Med. Biol. 2001; 27, 1107–1113.

[163] Wei, W., Zheng-zhong, B., Yong-jie, W., Qing-wu, Z., Ya-lin, M.,. Bioeffects offlow-frequency ultrasonic gene delivery and safety on cell membrane perme- ability control. J. Ultrasound Med. 2004; 23 (12), 1569–1582.

[164] W.J. Greenleaf, M.E. Bolander, G. Sarkar, M.B. Goldring, J.F. Greenleaf, Artificial cavitation nuclei significantly enhance acoustically induced cell transfection, Ultrasound Med. Biol. 24 (1998) 587–595.

[165] D.M. Hallow, A.D. Mahajan, T.E. McCutchen, M.R. Prausnitz, Measurement and correlation of acoustic cavitation with cellular bioeffects, Ultrasound Med. Biol. 32 (2006) 1111–1122.

[166] Sirsi, S., Borden, M.. Microbubble compositions, properties and biomedical applications. Bubble Sci. Eng. Technol. 2009; 1, 3–17.

[167] Klibanov, A.L., Shevchenko, T.J., Raju, B.L., Seip, L., Chin, C.T.. Ultrasound-triggered release of materials entrapped in microbubble-liposome constructs:a tool for targeted drug delivery. J. Control. Rel. 2010; 148, 13–17.

[168] P.A. Dayton, J.E. Chomas, A.F. Lum, J.S. Allen, J.R. Lindner, S.I. Simon, K.W. Ferrara, Optical and acoustical dynamics of microbubble contrast agents inside neutrophils, Biophys. J. 80, 2001; 1547– 1556.

[169] Abdelsalam M, Cheifetz IM Goal-directed therapy for severely hypoxic patients with acute respiratory distress syndrome: permissive hypoxemia. Respir Care 2010; 55(11):1483–1490

[170] Taylor CT, Moncada S Nitric oxide, cytochrome C oxidase, and the cellular response to hypoxia. Arterioscler Thromb Vasc Biol 2010; 30(4):643–647

[171] Ward DS, Karan SB, Pandit JJ. Hypoxia: developments in basic science, physiology and clinical studies. Anaesthesia 2011; 66(Suppl 2):19–26

[172] Iyer AK, Khaled G, Fang J, Maeda H. Exploiting the enhanced permeability and retention effect for tumor targeting. Drug Discov Today. 2006;11(17–18):812 818.

[173] Skinner SA, Tutton PJ, O'Brien PE. Microvascular architecture of experimental colon tumors in the rat. Cancer Res. 1990;50(8): 2411–2417.

[174] Matsumura Y, Maeda H. A new concept for macromolecular therapeutics in cancer chemotherapy: mechanism of tumoritropic accumulation of proteins and the antitumor agent smancs. Cancer Res. 1986;46(12 Pt 1): 6387–6392.

[175] Cabrales, P.; Intaglietta, M. Blood substitutes: evolution from noncarrying to oxygen- and gas-carrying fluids. ASAIO J. 2013, 59: 337-354.

[176] Modery-Pawlowski, C. L, Tian, L. L.; Pan, V.; Sen Gupta, A. Synthetic approaches to RBC mimicry and oxygen carrier systems. Biomacromolecules. 2013, 14: 939-948.

[177] Lundgren, C. E.; Bergoe, G. W.; Tyssebotn, I. The theory and application of intravascular microbubbles as an ultra-effective means of transporting oxygen and other gases. Undersea Hyperb. Med. 2004, 31: 105–106.

[178] Bisazza, A.; Giustetto, P.; Rolfo, A.; Caniggia, I.; Balbis, S.; Guiot, C.; Cavalli, R. Microbubble-mediated oxygen delivery to hypoxic tissues as a new therapeutic device. Conf. Proc. IEEE Eng. Med. Biol. Soc. 2008: 2067- 2070.

[179] Cavalli, R.; Bisazza, A.; Rolfo, A.; Balbis, S.; Madonnaripa, D.; Caniggia, I.; Guiot, C. Ultrasound-mediated oxygen delivery from chitosan nanobubbles. Int. J. Pharm. 2009, 378: 215-217.

[180] Cavalli, R.; Bisazza, A.; Giustetto, P.; Civra, A.; Lembo, D.; Trotta, G.; Guiot, C.; Trotta, M. Preparation and characterization of dextran nanobubbles for oxygen delivery. Int. J. Pharm. 2009, 381: 160-165.

[181] Cavalli, R.; Bisazza, A.; Trotta, M.; Argenziano, M.; Civra, A.; Donalisio, M.; Lembo, D. New chitosan nanobubbles for ultrasound-mediated gene delivery: preparation and in vitro characterization. Int. J. Nanomedicine. 2012, 7: 3309-3318.

[182] A. Lawrie, A.F. Brisken, S.E. Francis, D.I. Tayler, J. Chamberlain, D.C. Crossman, D.C. Cumberland, C.M. Newman, Ultrasound enhances reporter gene expression after transfection of vascular cells in vitro, Circulation 99, 1999; 2617–2620.

[183] Tachibana K, Tachibana S. The use of ultrasound for drug delivery. Echocardiography 2001;18(4):323e8.

[184] Basta G, Venneri L, Lazzerini G, Pasanisi E, Pianelli M, Vesentini N, et al. In vitro modulation of intracellular oxidative stress of endothelial cells by diagnostic cardiac ultrasound. Cardiovasc Res 2003;58(1):156e61

[185] Wu J. Temperature rise generated by ultrasound in the presence of contrast agent. Ultrasound Med Biol 1998; 24(2):267e74.

[186] Microbubbles and ultrasound: from diagnosis to therapy P.A. Dijkmansa, L.J.M. Juffermansa,b, R.J.P. Mustersb, A. van Wamelc, F.J. ten Catec, W. van Gilstd, C.A. Vissera, N. de Jongc, O. Kampa Eur J Echocardiography; 2004, 5, 245e256

[187] Tachibana K, Tachibana S. Transdermal delivery of insulin by ultrasonic vibration. J Pharm Pharmacol 1991; 43: 270–271.

[188] Mitragotri S et al. Ultrasound mediated transdermal protein delivery. Science 1995; 269: 850–853.

[189] Tang H et al. Theoretical description of transdermal transport of hydrophilic permeants: application to low-frequency sonophoresis. J Pharm Sci 2001; 90: 543–566.

[190] Joshi A, Raje J. Sonicated transdermal drug transport. J Control Release 2002; 83: 13–22.

[191] Tezel A et al. A theoretical description of transdermal transport of hydrophilic solutes induced by low frequency sonophoresis. J Pharm Sci 2003; 92: 381–393.

[192] Smith NB. Perspectives on transdermal ultrasound mediated drug delivery. Int J Nanomed 2007; 2: 585–594.

[193] Lavon I, Kost J. Ultrasound and transdermal drug delivery. Drug Discovery Today 2004; 9: 670–676.

[194] M.R. Prausnitz, S. Mitragotri, R. Langer, Current status and future potential of transdermal drug delivery, Nat. Rev. Drug Discovery 3; 2004, 115–124.

[195] A. Naik, Y.N. Kalia, R.H. Guy, Transdermal drug delivery: overcoming the skin's barrier function, Pharm. Sci. Technol. Today 3, 2000; 318–326.

[196] S.H. Lee, S.K. Jeong, S.K. Ahn, An update of the defensive barrier function of skin, Yonsei Med. J. 47, 2006, 293–306.

[197] P.M. Elias, Lipids and the epidermal permeability barrier, Arch. Dermatol. Res. 270, 1981 95–117.

[198] Y.N. Kalia, L.B. Nonato, C.H. Lund, R.H. Guy, Development of skin barrier function in premature infants, J. Invest. Dermatol. 111, 1998, 320–326.

[199] A.M. Wokovich, S. Prodduturi, W.H. Doub, A.S. Hussain, L.F. Buhse, Transdermal drug delivery system (TDDS) adhesion as a critical safety, efficacy and quality attribute, Euro. J. Pharm. Biopharm. 64; 2006, 1–8.

[200] M. Cormier, B. Johnson, M. Ameri, K. Nyam, L. Libiran, D.D. Zhang, P. Daddona, Transdermal delivery of desmopressin using a coated microneedle array patch system, J. Controlled Release 97; 2004, 503–511.

[201] X. Hui, T.C. Chan, S. Barbadillo, C. Lee, H.I. Maibach, R.C. Wester, Enhanced econazole penetration into human nail by 2-n-nonyl-1, 3-dioxolane, J. Pharm.Sci. 92 (2003) 142–148.

[202] S. Mitragotri, D. Blankschtein, R. Langer, Ultrasound-mediated transdermal protein delivery, Science (1995) 850–853.

[203] Tachibana K. Transdermal delivery of insulin to alloxan-diabetic rabbits by ultrasound exposure. Pharm Res 1992;9:952–954.

[204] Sinha VR, Kaur MP. Permeation enhancers for transdermal drug delivery. Drug Dev Industrial Pharm 2000;26:1131–1140.

[205] Tang Hua,Wang CCJ, Blankschtein D, Langer R. An investigation of the role of cavitation in low-frequency ultrasound-mediated transdermal drug transport. Pharm Res 2002;19:1160–1169.

[206] S. Mitragotri, D. Blankschtein, R. Langer, Transdermal drug delivery using low-frequency sonophoresis, Pharm. Res. 13 (1996) 411–420.

[207] J. Collis, R. Manasseh, P. Liovic, P. Tho, A. Ooi, K. Petkovic-Duran, Y. Zhu, Cavitation microstreaming and stress fields created by microbubbles, Ultrasonics 50 (2010) 273–279.

[208] J. Wu, W.L. Nyborg, Ultrasound, cavitation bubbles and their interaction with cells, Adv. Drug Delivery Rev. 60 (2008) 1103–1116.

[209] A. Williams, A possible alteration in the permeability of ascites cell membranes after exposure to acoustic microstreaming, J. Cell Sci. 12 (1973) 875–885.

[210] R. Pecha, B. Gompf, Microimplosions: cavitation collapse and shock wave emission on a nanosecond time scale, Phys. Rev. Lett. 84 (2000) 1328–1330.

[211] M. Lokhandwalla, B. Sturtevant, Fracture mechanics model of stone comminution in ESWL and implications for tissue damage, Phys. Med. Biol. 45 (2000) 1923.

[212] J. Katz, Jets from collapsing bubbles, Proceedings of the Royal Society of London, Ser. A: Math. Phys. Eng. Sci. 455 (1999) 323–328.

[213] S. Lee, D.J. McAuliffe, T.J. Flotte, N. Kollias, A.G. Doukas, Photomechanical transcutaneous delivery of macromolecules1, J. Invest. Dermatol. 111 (1998) 925–929.

[214] http://www.echotx.com/SonoPrep+For+Topical+Anesthesia.

[215] Robertson VJ, Baker KG. A review of therapeutic ultrasound: effectiveness studies. Phys Ther 2001; 81:1339–1350.

[216] Coleman DJ, Burgess SEP, Iwamoto T, Lizzi FL, Driller J, Rosado AL. Histological changes in porcine eyes treated with high intensity focused ultrasound. Ann Ophthalmol 1987;19: 133–138

[217] Lake, A. M., Hall, T. L., Kieran, K., Fowlkes, J. B., Cain, C. A., & Roberts, W. W. Histotripsy: Minimally invasive technology for prostatic tissue ablation in an in vivo canine model. Urology, 2008; 72(3), 682-686.

[218] Fry, F. J., Kossoff, G., Eggleton, R. C., & Dunn, F. (1970). Threshold ultrasonic dosages for structural changes in the mammalian brain. The Journal of the Acoustical Society of America, 48(6), 1413.

[219] Dyson, M., Woodward, B., & Pond, J. B. Flow of red blood cells stopped by ultrasound. Nature, 1971; 232(5312), 572-573.

[220] Pilla, A. A., Mont, M. A., Nasser, P. R., Khan, S. A., Figueiredo, M., Kaufman, J. J., et al. Non-invasive low-intensity pulsed ultrasound accelerates bone healing in the rabbit. Journal of Orthopaedic Trauma, 1990, 4(3), 246-253.

[221] Brookes, M., & Dyson, M. Stimulation of bone repair by ultrasound. International Journal of Rehabilitation Research, 1985; 8(Supplement), 73.

[222] Warden, S. J., Fuchs, R. K., Kessler, C. K., Avin, K. G., Cardinal, R. E., & Stewart, R. L. Ultrasound produced by a conventional therapeutic ultrasound unit accelerates fracture repair. Physical Therapy, 2006; 86(8), 1118.

[223] IEC61161:2007 Ultrasonics—Power Measurement—Radiation Force Balances and Performance Requirements (Geneva: International Electrotechnical Commission)

[224] IEC61161:2007 Ultrasonics—Power Measurement—Radiation Force Balances and Performance Requirements (Geneva: International Electrotechnical Commission)

[225] 2008 Guide to the Expression of Uncertainty in Measurement ISO/IEC GUIDE 98-3

[226] Durando G, Guglielmone C and Musacchio C 2011 HIFU ultrasound power measurements at INRiM J. Phys.: Conf. Ser. 279 012013

[227] IEC 62127-1: Ultrasonics - Hydrophones – Part 1: “Measurement and characterization of medical ultrasonic fields up to 40 MHz using hydrophones”.

[228] R. Pecha. FOPH 2000: Technical Description and Instruction Manual RP Acoustics, Leutenbach, Germany (1996).

[229] Ultrasonic measurement tank – A user Manual. Precision Acoustic LTD. www.acoustic.co.uk

[230] Clarke RL, Ter Haar GR. Temperature rise recorded during lesion formation by high-intensity focused ultrasound. Ultrasound Med Biol 1997;23:299.

[231] Dickinson RJ. Thermal conduction errors of manganinconstantan thermocouple arrays. Phys Med Biol 1985;30:445–453.

[232] Fry WJ, Fry RB. Determination of absolute sound levels and acoustic absorption coefficients by thermocouple probes. J Acoust Soc Am 1954;26:311–317.

[233] Rivens I, Shaw A, Treatment monitoring and thermometry for therapeutic focused ultrasound Int. J. Hyperthermia, March 2007; 23(2): 121–139

[234] Morris, Ian Rivens, Adam Shaw and Gail ter Haar, Investigation of the viscous heating artefact arising from the use of thermocouples in a focused ultrasound field Phys. Med. Biol. 53 (2008) 4759–4776 doi:10.1088/0031-9155/53/17/020

[235] Lafon C., Haczkowskt P., Developement and characterization of an innovative synthetic tissue- mimicking material for hifh intensity focused ultrasound (HIFU). Misty Noble Center for Industrial and Medical Ultrasound, University of Washington, Seattle, USA, 98105 Oleg A. Sapozhnikov. 2001 IEEE ultrasonic symposium

[236] E.L. Madsen, J.A. Zagzebski, M.C. Macdonald and J.R. Frank, “Ultrasound focal lesion detectibility phantoms,” Med. Phys., 1991; vol. 18(6), pp.1171-1180.

[237] Takegami K., Kaneko Y. , Watanabe T., Maruyama T., Polyacrylamide gel containing egg white as new model for irradiation experiments using focused ultrasound, Ultrasound in Medicine & Biology 30,10, 2004, 1419–1422.

[238] Browne JE, Ramnairne KV, Hoskins PR and Watson AJ. Assessment of the acoustic properties of common tissue-mimicking test phantoms, Ultrasound in Medicine and Biology, 29,7; 2003, 1053–1060

[239] L.M. Cannon, A. Fagan, Jacinta Browne. Novel tissue mimicking materials for high frequency breast ultrasound phantoms. Ultrasound Med Biol. 2003 vol 37 n 1.

[240] Brewin MP, Pike LC, Rowland DE, Birch MJ. The acoustic properties, centered on 20 MHZ, of an IEC agar-based tissue-mimicking material and its temperature, frequency and age dependence. Ultrasound Med Biol. 2008;34(8):1292-306. Epub 2008 Mar 14

[241] Furukawa H. Effect of varying preparing-concentration on the equilibrium swelling of polyacrylamide gels. J Molec Struct 2000;554: 11–19.

[242] Prokop A, Polyacrilamide gel as an acoustic coupling medium for focused ultrasound therapy. Ultrasound in Med. & Biol., Vol. 29, No. 9, pp. 1351–1358, 2003

[243] N. Carmonaa,V. Bouzasa, F. Jiménezb,M. Plazaa, L. Péreza, M.A. Garcíaa, M.A. Villegasf, J. Llopisa, Cobalt (II) environment characterization in sol–gel thermochromic sensors, Sensors and Actuators B 145 (2010) 139–145

[244] Civale, J., Clarke, R., Rivens, I. & ter Haar, G., The use of a segmented transducer for rib sparing in HIFU treatments, Ultrasound in Medicine & Biology, 32, 11, (2006),1753–1761

[245] Srivastava J., Srivastava J. N., Sarfaraz A., Mathur G. N., Quantification of response time in poly(vinyl alcohol)–metal complex thermochromic polymeric systems, Journal of Applied Polymer Science, 100,6, (2006), 4832–4834

[246] Krafft, M. P.; Riess, J. G. Highly fluorinated amphiphiles and colloidal systems, and their applications in the biomedical field. A contribution. Biochimie. 1998, 80: 489–514.

[247] Bos, G. W.; Hennink, W. E.; Brouwer, L.A.; den Otter, W.; Veldhius, F. J.; Van Nostrum, C. F.; Van Luyn, M. J. A. Tissue reactions of in situ formed dextran hydrogels crosslinked by stereocomplex formation after subcutaneous implantation in rats. Biomaterials. 2005, 26, 3901–3909.

[248] De Groot, C.J.; Van Luyn, M. J. A.; Van DijK-Wolthuis, Cadée, J. A.; Plantinga, J. A.; Den Otter, W.; Hennink, W. E. In vitro biocompatibility of biodegradable dextran-based hydrogels tested with human fibroblast. Biomaterials. 2001, 22, 1197–1203.

[249] Möller, S.; Weisser, J.; Bischoff, S.; Schnabelrauch, M. Dextran and hyaluronan methacrilate based hydrogels as matrices for soft tissue reconstruction. Biomol. Eng. 2007, 24: 496–504.

[250] Sze, A.; Erickson, D.; Ren, L.; Li, D. Zeta-potential measurement using the Smoluchowski equation and the slope of the current-time relationship in electroosmotic flow. J. Colloid Interface Sci. 2003, 261: 402-410.

[251] Jose, J.; Willemink, R. G.; Resink, S.; Piras, D.; van Hespen, J. C.; Slump, C. H.; Steenbergen, W.; van Leeuwen, T. G.; Manohar, S. Passive element enriched photoacoustic computed tomography (PER PACT) for simultaneous imaging of

acoustic propagation properties and light absorption. Opt. Express. 2011, 19: 2093-2104.

[252] Laufer, J.; Delpy, D.; Elwell, C.; Beard, P. Quantitative spatially resolved measurement of tissue chromophore concentrations using photoacoustic spectroscopy: application to the measurement of blood oxygenation and haemoglobin concentration. Phys. Med. Biol. 2007, 52: 141-168.

ACKNOWLEDGMENTS

I would like to sincerely thank to my supervisors Dr. Giovanni Durando and Adriano Troia. Their ideas and informative discussions have played an important role in the successful completion of this work. In particular, I owe great thanks to Adriano: he encouraged me when I needed be encouraged and he never accepted anything less than what I was capable of. I thank him for his guidance and for providing me an environment that allowed me to grow both as a scientist and as a person.

I would also like to thank all the staff of the department of acoustic at INRIM for their help and support.

I would also like to thank Mauro Prato for his invaluable help at whatever hour of the day or night.

Lastly, I would like to thank my family for all their love and encouragement. I would never be able to do all of this without them. I would like to thanks my sister for all her advice and support and, most of all, thanks to Andrea, for his love, support and patience during these years. To Andrea and my family, from the bottom of my heart, thank you, thank you, thank you.